A THESIS

FOR THE DEGREE OF DOCTOR OF PHILOSOPHY

Fabrication and Integration of Solution Processed Electronic Devices using Printed Technologies

Shawkat Ali

Department of Ocean System Engineering

GRADUATE SCHOOL

JEJU NATIONAL UNIVERSITY

June 2016

To

My Parents and Famil

Nothing in Nature is random…
A thing appears random only through the incompleteness of our knowledge

Spinoza (1632-1677)

Acknowledgements

I would like to present my humble gratitude to Almighty ALLAH WHO bestowed me courage and skill to complete the doctoral studies with quite satisfaction and contentment. At this vital occasion when I am going to get the highest educational degree, I acknowledge my parents for their encouragement and every kind of support during my studies from the first day of my school until now. Especially the prayers of my mother and her believe in me have always been a source of courage during my entire life.

I am heartily thankful to my supervisor Prof. Jinho Bae whose guidance and every kind of support from the start to the end of my Ph.D. studies were there for me in the completion of this research work. Who polished my skills not only to grow as a quality researcher but also as an instructor, independent and innovative thinker. I would like to pay my heartiest thanks with best regards to Prof. Jinho Bae, who put his full efforts to give me confidence, access over all the resources in the laboratory and hire external resources as well to accomplish the task. During my Ph.D. studies, Prof. Bae provided me shelter against all kinds of crisis from morally depraved conditions to financial problems. I would also like to thank Prof. Chong Hyun Lee head of the department who gave me valuable suggestions ideas and pleasant environment to pursue the fruitful end of my research work. I am also grateful to Prof. Kyung-Hyun Choi for his support during my first semester for lab and equipment.

I am especially grateful to Dr. Muhammad Naeem Awais who introduced me to my supervisor Prof. Jinho Bae for postgraduate studies at OISE Lab, Jeju National University. I am extremely grateful to Dr. Rashad Ramzan my mentor during master's studies at National University of Computer and Emerging Sciences Pakistan who motivated me to pursue my higher studies. I am thankful to all my teachers who taught me from my elementary school to the highest educational degree.

I would love to present my tribute to my loving Sisters, Brothers, and sisters in Law for their support and care when I was busy in my studies and could not give them much time. All of my family has always been a source of appreciation and admiration throughout my life either in my professional career or student life. I am also thankful to my wife for scarifying her one year and staying at jeju with me during my last year of Ph.D. I would like to disclose that Almighty GOD bestowed me

such a noble and dominating figures in my life, without whom I could not have predicted myself to accomplish this task.

I would like to thank my colleagues at OISE Lab and friends in the Jeju University as well, Arshad Hassan, Waseem Abbas, Gul Hassan, Fasihullah, Dr. Adnan Ali, Dr. Kamran Ali, Dr. Safdar Ali, Dr. Rasheed, Irshad, Wahid, Dr. Jael Lee, Dr. Juho Kim, Kibae Lee, Joung Hoa, Yuhan Choi, Hansoo Kim. I would also like to thank my colleagues at NUCES-FAST Islamabad campus for their encouragement to pursue my Ph.D. studies, Dr. Aftab Maroof, Dr. Waseem Ikram, Dr. Mukhtarullah, Dr. Ataul Aziz, Aamir Munir, Kashif Islam, Saqib Raja, Rizwan Javed, Ahmar Qamar, Niaz Ahmed, Shehzad Ahmed.

In the end, I would like to acknowledge and promise myself to be bind by the golden tips of life as positive thinking, hard work and consistency in execution of the idea.

Shawkat Ali

Abbreviations and Notations

CC	Compliance Current
DCB	Di-cholorobenzene
DMF	N,N-dimethyl-formamide
FESEM	Field Emission Scanning Electron Microscope
FIB	Focused Ionic Beam
FORS	Full Organic Resistive Switch
G-QDs	Graphene Quantum Dots
HRS	High Resistance State
ITO	Indium Tin Oxide
I-V	Current-Voltage
LRS	Low Resistance State
MEH:PPV	Poly[2-methoxy-5-(2 ’-ethylhexyloxy)–(*p*-phenylenevinylene)]
Memristor	Memory Resistor
MIM	Metal Insulator Metal
NDR	Negative Differential Resistance
NP	Nanoparticle
OLED	Organic Light Emitting Diode
PEDOT:PSS	Poly(3,4-ethylenedioxythiophene):poly(styrenesulfonate)
PET	Polyethylene terephthalate
PVP	Poly(4-vinylphenol)
ReRAM	Resistive Random Access Memory
SCLC	Space Charge Limited Current
STDP	Spike Timing Dependent Plasticity
TCLC	Trap Charge Limited Current
XPS	X-ray Photoelectron Spectroscopy
XRD	X-ray Diffraction
ZrO_2	Zirconium Dioxide
A^*	Effective Richardson Constant
C	Capacitance
d	Thickness
e	Electron
E	Electric Field
H_b	Density of Traps at the Edge of Valance Band
k	Boltzmann Constant
L	Inductance
l	Distribution of Traps in the Band Gap
M	Memristance
N_v	Effective Density of State
R	Resistance
R_{OFF}	High Resistance State
R_{ON}	Low Resistance State
T	Absolute Temperature
V_{TH}	Threshold Voltage
β	Schottky Coefficient
E	Dielectric Constant
ε_0	Permittivity of the Free Space
λ	Wavelength
J	Current Density
i	Electric Current
q	Electric Charge
v	Voltage

List of Figures

List of Tables

List of Contents

Abstract

Recently there has been a growing interest in the realization of low cost, flexible and wearable electronic systems including flexible displays, RFID tags and biomedical sensors. Printed Electronics has emerged as one of the most promising alternative manufacturing technologies because of its ambient manufacturing processing. From electronic market point of view, if we consider the sensors and smart systems to be fully manufactured with a printed process it will capture around $1B by 2020. In growing printed electronic market, solution processed materials including organic and inorganic are playing vital role in the rapidly improving performance of the printed electronic devices. In addition to these materials, the advance open-air manufacturing techniques such as electrohydrodynamic EHD, inkjet and spin coating are also contributing in improvement of the performance of printed electronic devices, circuits and systems.

This thesis focuses on the fabrication of printed, flexible and stretchable electronic devices based on solution processed materials and utilization of printed techniques. Materials are synthesized to make it printable through printed techniques for the realization of electronic devices and circuits. The printed techniques used in device manufacturing are electrohydrodynamic EHD, Inkjet material printing, magnetic sputtering, and spin coating. In this work, I have used different substrates according to the manufacturing process requirement and device in flexible, stretchable and transparent applications. The main substrates utilized in fabrication of devices are glass, PDMS, PET and paper. The fabricated devices were characterized against their electrical, mechanical, optical and chemical behavior to verify the solution processed device fabrication approach.

In addition to the printed devices, some printed circuits and systems were also fabricated and characterized such as conventional crossbar passive array with pull-up resistors and asymmetric memristor to minimize the sneak current problem in nonvolatile resistive memory (ReRAM), and printed state memorable organic light emitting device (SMOLED) for the flexible programmable display applications.

Several types of printed devices are fabricated and discussed in this thesis includes: memristors, memory units, capacitors, diodes, temperature sensors, humidity sensor and biomedical sensors. I have fabricated different memristors based on graphene quantum dots (GQDs), zinc stannate ($ZnSnO_3$), poly(4-vinylphenol) (PVP) and zirconium oxide (ZrO) to improve retention time, on/off

ratio and endurance cycles. These memristors were utilized for the cross bar resistive memory applications. A printed differential temperature sensor (DTS) based on silver nanoparticles (AgNPs) is fabricated which measures temperature of a flexible or curved body as well as its strain. To measure humidity sensor in a wide range with high sensitivity, an inkjet printed humidity sensor based on graphene and methyl-red composite is fabricated that converts the relative humidity (%RH) level into its terminal resistor with 96% sensitivity in 5-96% RH. Comb type electrodes were decorated with silver nanowires (AgNWs) to realize a biomedical printed sensor that detects and classify three popular bacteria types JM-109, DH5-$\boldsymbol{\alpha}$ and salmonella through impedance analysis. Flexible and stretchable photo sensors based on perylene/graphene composite on a PDMS and PET substrates were fabricated to detect the visible light with 25% axial strain. Printed diodes for rectification applications in printed electronic circuits based on organic materials N,N′-Bis(3-methylphenyl)-N,N′-diphenylbenzidine (TPD) and fullerene (C_{60}). The prototype of printed electronic devices and circuits fabricated by utilizing solution-processed materials are good achievements and a way to future printed flexible and stretchable electronics.

Chapter 1 Introduction

1.1 Printed Electronics

Printed electronics is a new branch of electronics where functional materials are directly deposited through printing techniques on substrates to make operational electronic devices and systems. Printed electronics is rapidly grooming because of it ample advantages over conventional rigid electronics such as Silicon or Gallium Arsenide, which are fabricated in clean-room environments at wafer-size level. This type of electronics starts to find severe limitations to satisfy the demands imposed by new applications, especially those requiring large area, mechanical flexibility or compatibility with biological systems. On the other hand, printed electronics full-fill the missing gaps of conventional electronics with more dynamic style including easy fabrication, environmental friendly, low cost, low temperature and ambient conditions processing. Within the printed electronics, organic electronics, polymer electronics or plastic electronics consist of using organic materials as the substrate or active material in electronic circuits and systems. Some of the organic electronic devices have reached a level to find a place in the consumer electronics market for large-area applications such as, organic thin film transistors (OTFTs) or especially organic LEDs (OLEDs), already used on modern displays and TVs. As a natural expansion of the field, the development of low-cost ubiquitous flexible sensors, biomedical stretchable and implantable devices or intelligent surfaces are currently gaining a lot of interest. These devices require all the use of polymers as supportive substrate. Using polymers substrates as substrates for electronic systems is then opening new opportunities in the field of micro engineering. Polymers have the potential of making electronics very low-cost, environmental friendly, disposable, biocompatible or biodegradable. Moreover, they can bring benefit to electronic systems especially in those applications where optical opacity, weight or mechanical rigidity is limiting factors. Some polymers are also able to stretch or deform into arbitrary shapes without losing their properties. The fact that they are inexpensive and compatible with large-scale production though roll-to-roll or sheet-to-sheet process make them the perfect complement to be used with printing technologies, rather than with standard clean-room techniques such as photolithography, lift-off or etching; to the point that

the term printing electronics often implies the use of a plastic or paper substrate. Some of the applications of printed electronics are shown in Figure 1.1.

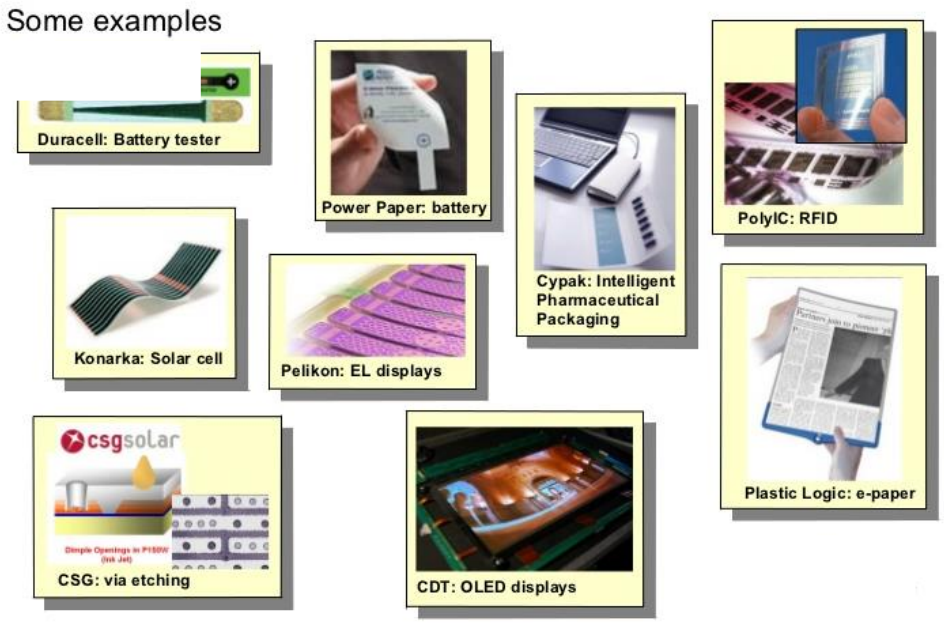

Figure 1.1. Printed electronics applications.

Printed electronics is further divided into flexible and stretchable electronics based on their materials and techniques used for the devices and systems.

1.1.1. Flexible Electronics

Flexible circuits have been one of the fastest growing market segments for interconnection products in the last several years, which is due to the wide range of applications enabled by flexibility. Like conventional rigid circuit boards, flexible circuits can be single-sided, double-sided or multilayered. Applications of flexible circuits can be roughly divided into two categories: (1) dynamic and (2) flex-to-fit. In dynamic applications, flexibility enables movement and changing form factors, whereas in flex-to-fit applications flexibility is needed only in the assembly phase to fit circuit board in such form factor, which is not possible with rigid planar boards. A typical example of a flex-to-fit [1] and dynamic flexible electronics application is shown in Figure 1.2.

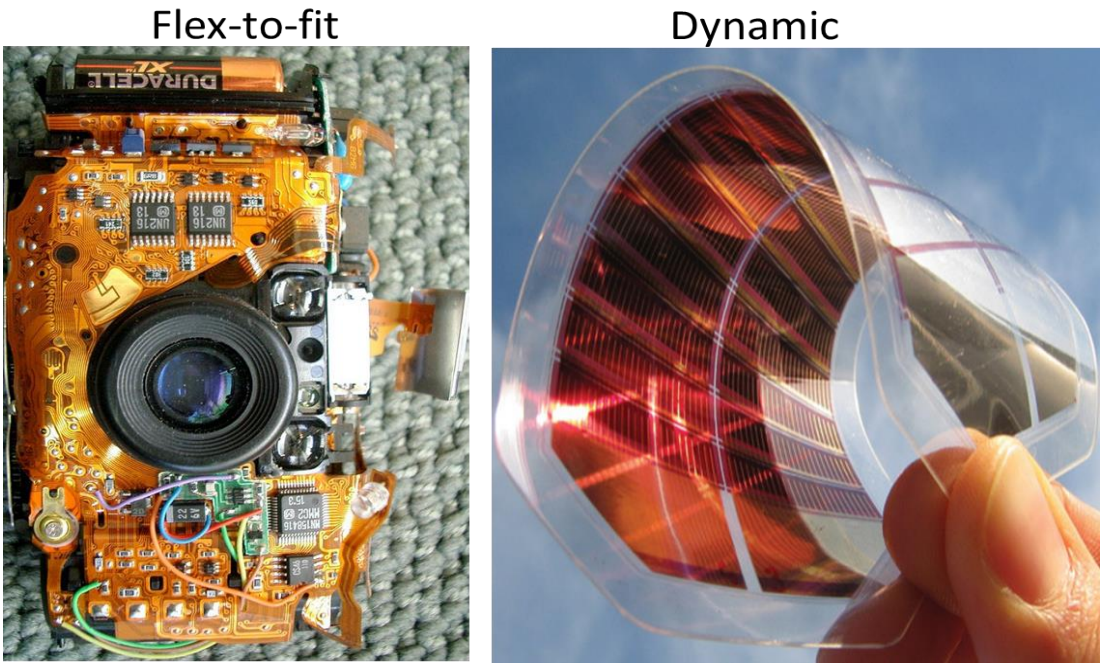

Figure 1.2. Olympus Stylus camera with covers removed showing flexible circuit board wrapped around camera frame [1], and a fully flexible solar cell.

1.1.2 Stretchable Electronics

Printed electronics allow the manufacturing of stretchable electronics as the processing temperature is low where polymeric substrate can work. Making the stretchable electronic devices there are two choices available, first method is to use intrinsically stretchable materials, like conductive polymers or organic semiconductors, which have relatively poor electrical performance compared to conventional inorganic electronic materials. The second method is to use conventional electronic materials and make the system stretchable. This way good electrical performance is achieved, but the stretching is more challenging, since conventional semiconductors like silicon are hard and brittle. If rigid areas with silicon-based semiconductors are kept small and the interconnections between them are made stretchable, resulting system appears stretchable macroscopically. Figure 1.3 illustrates the different approaches to manufacturing stretchable electronics. Stretchable interconnects are usually made by exploiting out-of-plane deformation or planar patterning which help to reduce stresses caused by stretching. The actual length of conductors is increased while dimensions along one or two axis are pre served. Consequently, this converts stretching to bending for strains between the actual length of conductor and the relaxed state of conductor. Other methods for producing

stretchable interconnects rely on thin films and forming of microscopic cracks, which serve as strain relief and form a conductive network.

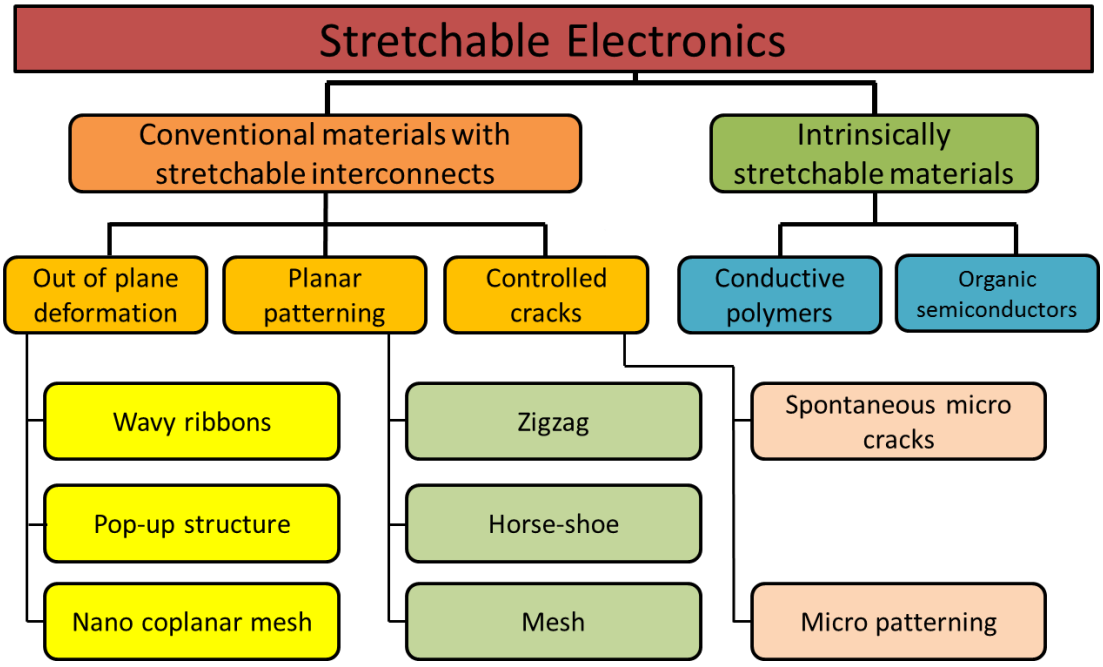

Figure 1.3. Options for manufacturing stretchable electronics.

1.2 Printed Electronics Technologies

Recent years have seen a great demand in the field of printed electronics because their light weight, environment-friendly, low-cost manufacturing, ease of fabrication, and the availability of inexpensive substrates such as papers, textiles, and plastics which make flexible electronics an attractive candidate for the next generation of consumer electronics.

For the fabrication of printed electronic devices, a variety of fabrication techniques is available in which some are matured and commercialized whereas some techniques are still under research. Main task of the printed electronics techniques is to deposit the functional materials on a substrate with precision and high accuracy where the thickness and uniformity of the film is main concern. In the history of thin films deposition, various techniques have been adopted including. Figure 1.4 shows some of the schematic diagrams of different printing techniques including chemical bath, spin-coating, dip coating, doctor blade, metering rod, slot casting, spray coating, screen printing, inkjet printing and aerosol jet. Other than these techniques, electrostatic spray deposition (ESD) and electro hydrodynamic (EHD) use for the deposition of thin films, where material is deposited

through electrostatic field. All fabrication techniques have their advantages and disadvantages. Some of them need vacuum chambers, heat, and a special environment to process the fabrication of a device. Some materials require special environment such as specific temperature, pressure, humidity, light and vacuum, therefore the fabrication techniques are adopted accordingly.

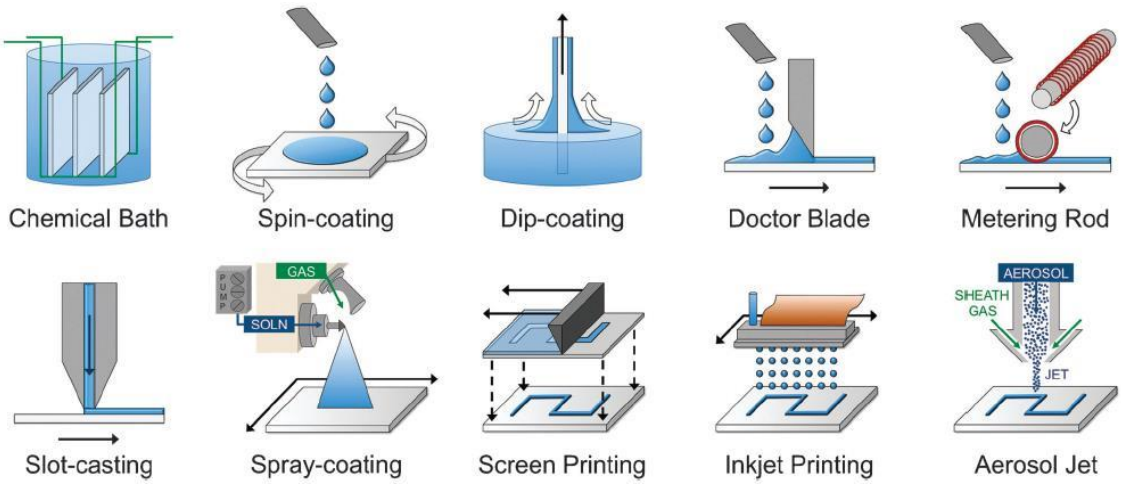

Figure 1.4. Various printing techniques based on solution-processed manufacturing [2].

In this thesis work, for the fabrication of devices and circuits ink jet, EHD, spin coating and sputtering are used. These techniques are discussed in detail in the forthcoming sections.

1.3 Ink-jet Printing

Inkjet printing is a liquid deposition technique where the droplets of the ink are ejected with the same volume and printed on the substrate. It is a low cost, material-conserving, non-contact, additive patterning and maskless approach with the scalability to large area manufacturing. Inkjet printers are classified into two main types, continuous inkjet and drop-on-demand (DOD) inkjet. In continuous inkjet printers, the ink ejected by the pressure is broken into uniform droplets and directed to the required place on the substrate with the help of deflecting electrode. These inkjet printers operate at high-frequency drop generation, are best suited for graphic arts and industrial applications. In DOD inkjet printers, the drops are generated with various volume controlled by the applied voltage on the piezoelectric materials of the channel wall. At the beginning the voltage is applied on one channel and as the piezoelectric effect, the channel is enlarged and filled with the ink; then the voltage will applied to the neighbor channel, which will is enlarged and at the same time the first channel will shrink and release a drop of ink. Thus by

applying voltage on channels, the ink can be ejected in the form of drops and printed on substrate as the pattern designed. There are two main ways to generate the pressure pulse necessary to form and eject the ink drops out of their small reservoir through a micrometer sized nozzle (see Figure 1.2). The first way consists of the generation of a bubble by using a heater (thermal inkjet). The second way is to use a MEMS piezoelectric actuator that squishes the ink out (piezoelectric inkjet) [3].

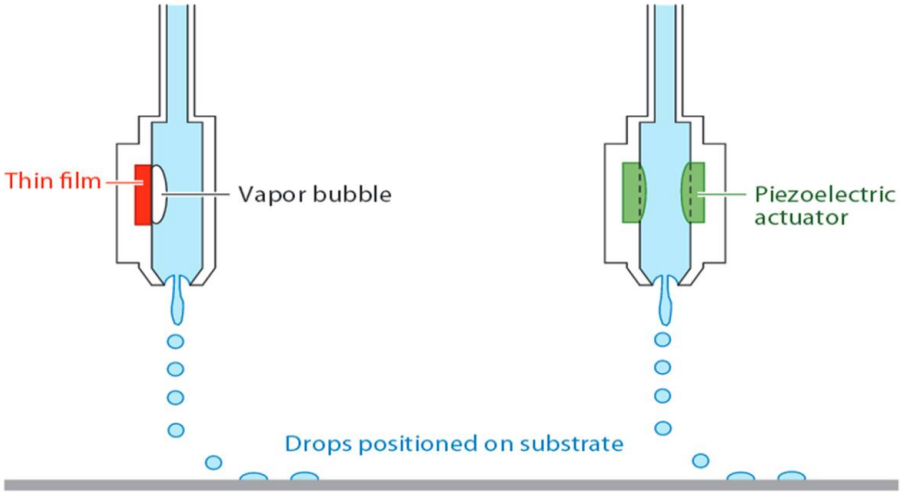

Figure 1.5. Schematic diagram showing the operation of drop-on-demand inkjet printing, where drops are formed and ejected in two ways: Thermal inkjet (on the left) and piezoelectric inkjet (on the right) [3].

1.3.1 DMP-3000 ink-jet material printer

Digital photograph of the DMP-3000 is shown in the Figure 1.6a, it is consisted of DMP-300 inkjet material printer and a personal computer with monitoring unit. The schematic diagram of the same printer is shown in Figure 1.6b, where main components are shown includes high-resolution camera, monitor, PC control system, jet driver, 16 nozzles head, ink reservoir, pressure controller, strove LED, temperature controller and moveable stage. These components mainly contribute in printing process. The features of DMP-3000 printer are print area 300x300mm, substrate thickness 0.05 to 30 mm, system position accuracy ±5 µm, repeatability is ±1 µm, and platen temperature from room 25 to 60 °C. To print a device through inkjet printer various steps are followed from design of layout to the product. The detailed procedure is explained in the coming section.

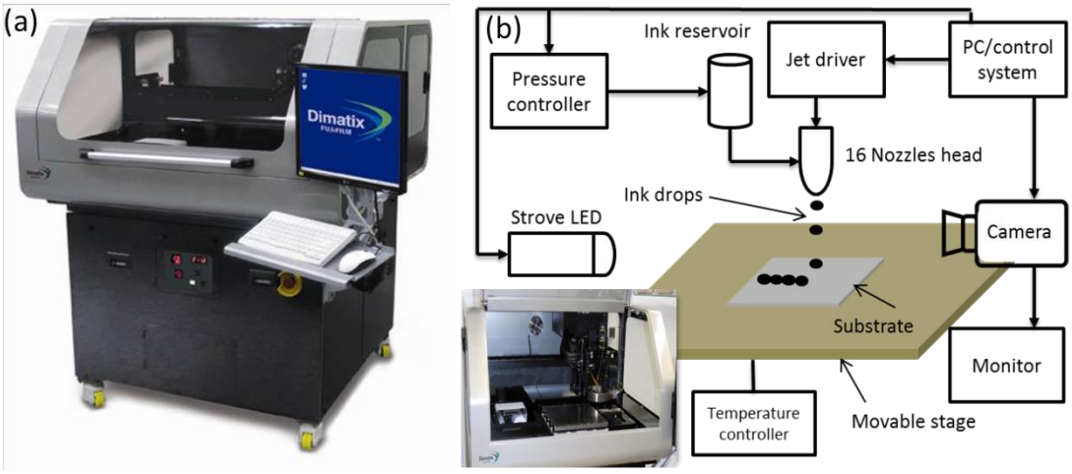

Figure 1.6. (a) Digital photograph of DMP-3000 inkjet material printer. (b) Schematic diagram of the DMP-3000 along main components.

1.3.2 Printing with DMP-3000

First, a schematic is designed in any circuit design software that can export bitmap (.bmp) or drawing exchange format (.dxf). The output file is then converted into printer compatible file (.ptn) format in the Dimatix Drop Manager (software to controlled Dimatix Printer). This (.ptn) file is then loaded into DMP-3000 to initialize the printing, the flow diagram is shown in the Figure 1.7a. Ink of 3 ml is filled in the cartridge that is maximum filling limit of the cartridge, ink is filled through a syringe through filling port and then the nozzle part of the cartridge is fixed with reservoir part as shown in Figure 1.7b. The cartridge has 16 nozzles with 254 µm spacing in a single row. The cartridge is then loaded onto the printhead of the printer. There are three different type of the printhead compatible with DMP-3000 SX3, SE3 and SE-DPN having nozzle diameters of 19, 42 and 35 µm respectively. Provides drop volume of 1 pico liter and 10 pico liter for DMC-11601 and DMC-11610 respectively [4]. After loading the cartridge into the printer, layout of the desired pattern is loaded to the printer and parameters are set for the printing including substrate thickness, drop size, temperature of the substrate and number of nozzles.

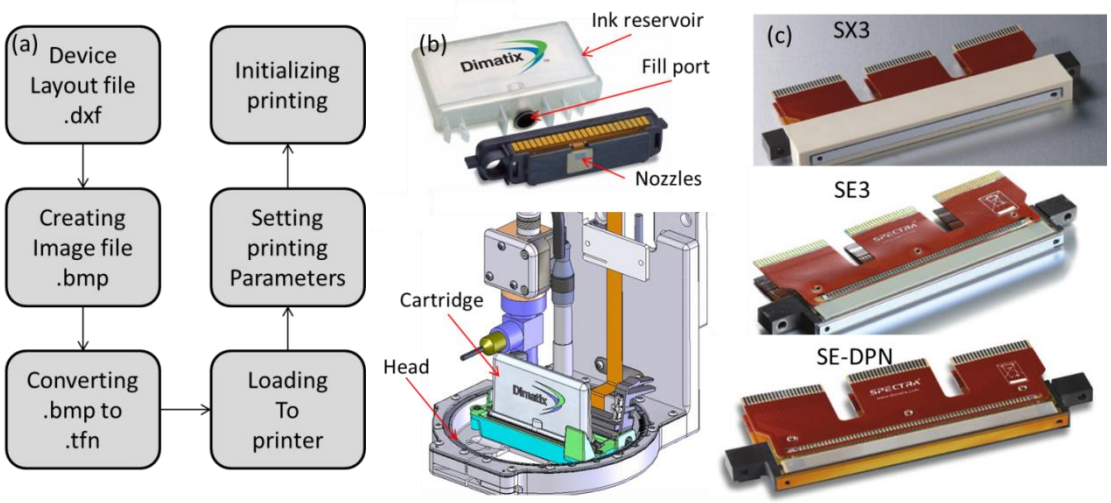

Figure 1.7. (a) Flow diagram of the printing process from layout to printing. (b) Cartridge of 16 nozzle and printhead of the DMP-3000. (c) Different printhead of the DMP-3000 material printer.

1.3.3 Jetting control

Jetting of the piezoelectric nozzles is controlled through a waveform applied to the transducers in the printhead. The waveform is shown in Figure 1.7, the wave signal is formed by four segments. Each of the four segment has three properties, duration, and level and slew rate. The applied voltage is proportional directly to the volume of the pumping chamber and slew rate control the speed of operation. As illustrated in Figure 1.7, the stand by phase bring the piezoelectric transducers to a relaxed position while the chamber is at maximum volume. In the first phase, a decrement in voltage occurs that retract the piezoelectric transducers drawing material into the pumping chamber followed by the settling time. In phase 2, the material is pushed into the chamber where it flows in two directions, to nozzle and to reservoir due to acoustic waves. The wave causes a droplet out from the nozzle. In the third phase, the piezoelectric transducers retract slightly breaking the droplet from the chamber. An appropriate slope between phase 3 and phase 4 can provide a damping effect to prevent air from being inter into the chamber. Finally, the voltage wave form returns back to the standby position and starts again from phase 1 if the waveform is periodic. The droplet velocity and size is controlled through the voltage level of waveform. If the voltage is low, it will not generate the droplet and if the voltage is high, it will generate satellite drops along with droplet.

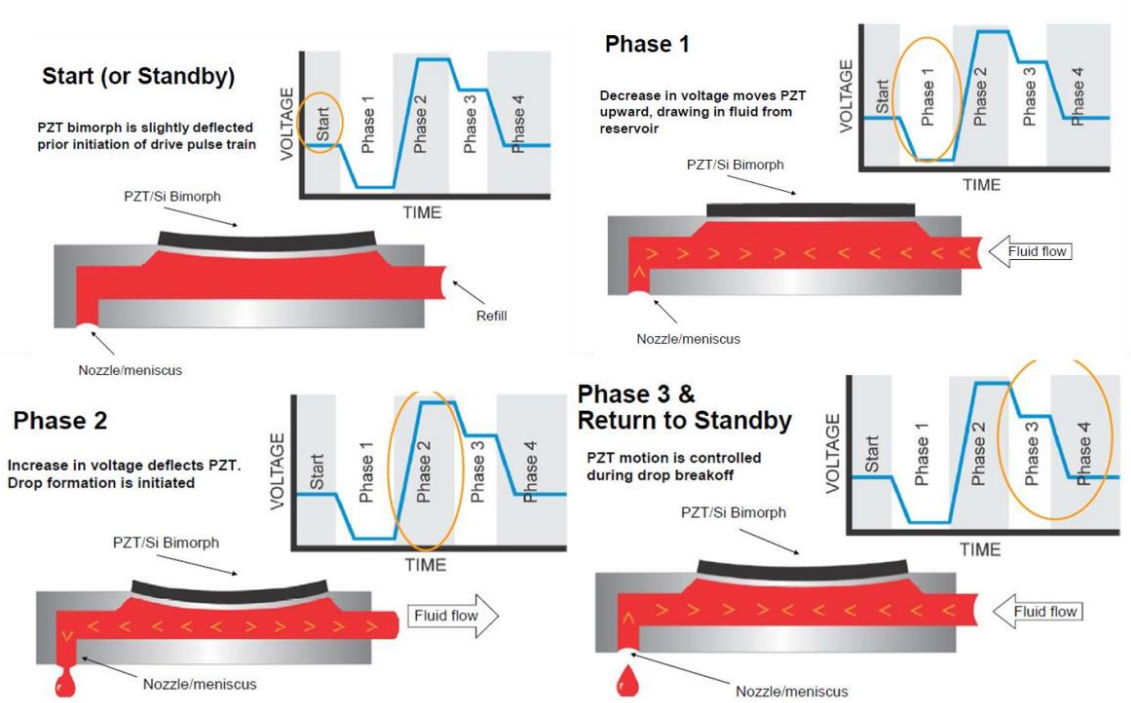

Figure 1.8. Voltage wave shpe for jetting the drop.

1.3.4 Coffee ring effect

A coffee ring effect occurs when the ink jetted drops completely wet the surface leading to an excess of solute at the edges as shown in Figure 1.9. This effect is due to the higher evaporation at the outer edges of the deposited drop, which causes an outward convective flow to replenish the lost solvent thus resulting in the accumulation of solute at the edges. The coffee ring effect can be reduced by several methods including (1) controlling the substrate's temperature, (2) incorporating co-solvent with a high boiling point and lower surface tension.

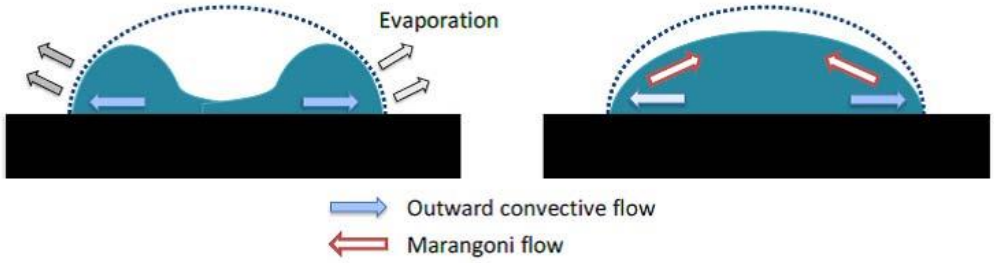

Figure 1.9. Coffee ring formation and suppressed by Margoni flow [5].

1.4 EHD fabrication technique

EHD is a cost effective, ambient temperature deposition, feasible for mass production, free of harmful radiation and short fabrication time deposition technique. The E H D setup and schematic diagram is shown in Figure 1.10, contains XY-stage for the substrate movement, light source and camera to observe EHDA jet modes, ink storage and supply section, high power voltage source to supply electric potential, nozzle to deposit the thin patterns of electrodes and active layer on the substrate, and computer to monitor and control all the deposition process during the experiment.

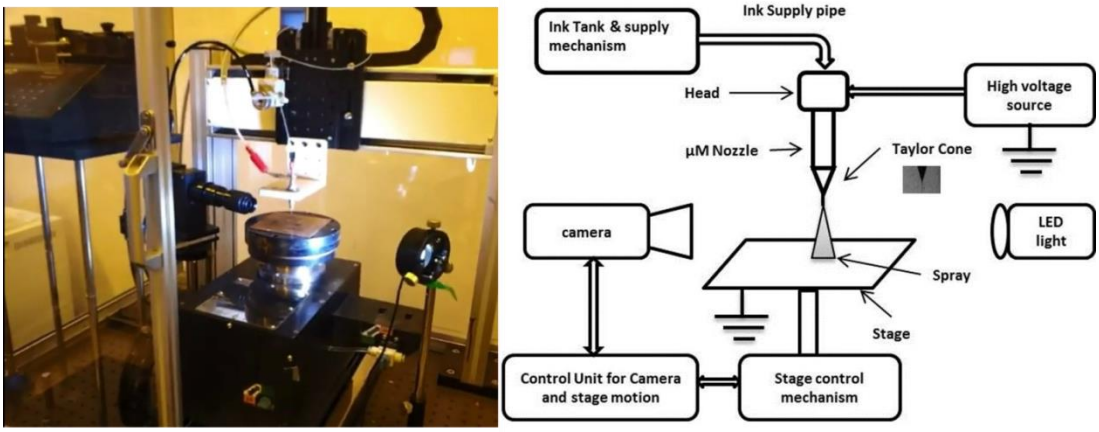

Figure 1.10. Digital photograph of the EHD system and schematic diagram of the EHD setup showing main components.

1.4.1 Printing with EHD

EHDA printing technology is an emerging direct printing and deposition technology in which the ink is pumped through a nozzle at some appropriate flow rate with the positive potential at the nozzle and grounding the substrate. The induction of the surface charges on the pendent meniscus emerging at the nozzle outlet, results in an electric stress over the liquid surface. If the electric field and flow rate are in some operating range then this will overcome the surface tension stress over the liquid surface and results in deformation of the droplet at the orifice of the nozzle into a conical shape. Due to the tangential electric field acting on the surface of the liquid cone, a thin jet emanates at the cone apex that further breaks up into a number of small droplets under the effect of coulomb forces. While changing the flow rate and applied voltage, different spraying modes exit in EHD technique like dripping, micro dripping, spindle, cone-jet and multi-jet mode as shown in Figure 1.11. In this particular case, 5.5 kV and flow rate from 10 to 100µl/h are the suitable parameters for the stable cone jet mode. Stable cone-jet mode is most important spraying mode because of the

generation of the mono dispersed droplets with few micrometer diameters. A complete detail and phenomenon of the EHDA process can be explored in [6],[7]. Thin film deposition through EHDA has been researched for many applications. The EHDA technique has been used for the deposition of the CIS absorber layer. Gold films have been deposited with the EHDA on silicon wafer substrate [8].

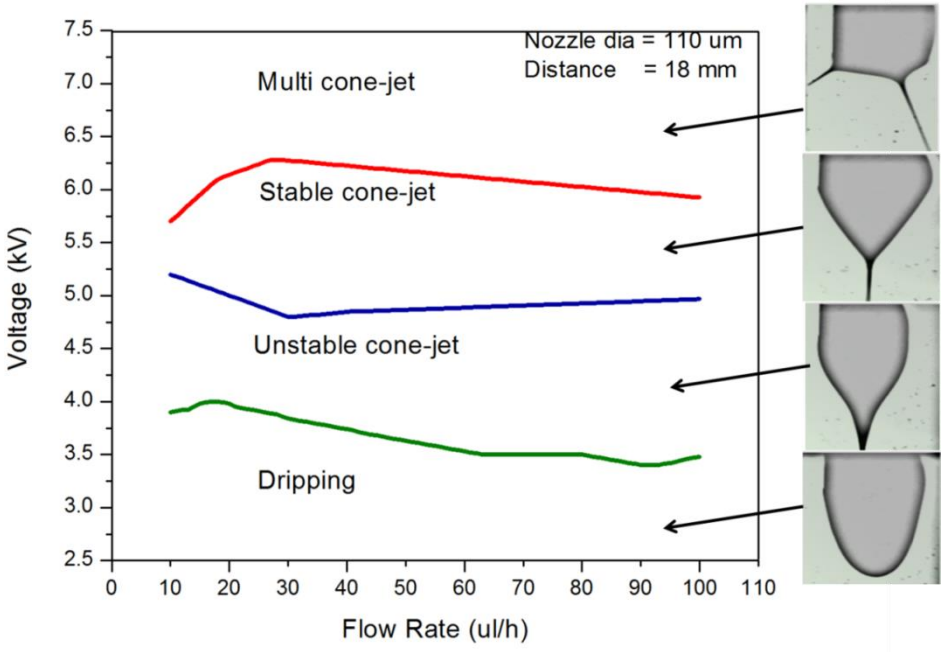

Figure 1.11. EHD modes during deposition of material, dripping mode, unstable cone jet mode, stable cone jet mode and multi jet mode.

1.5 Spin casting

Spin coating has been used for several decades for the fabrication of thin films. A typical process involves depositing a small puddle of a fluid resin onto the center of a substrate and then spinning the substrate at high speed (typically measured in revolution per minute rpm). Centripetal acceleration will cause the resin to spread to, and eventually off, the edge of the substrate leaving a thin film of resin on the surface. Final film thickness and other properties will depend on the nature of the resin such as, viscosity, drying rate, percent solids, surface tension, etc. and the parameters chosen for the spin process. Factors such as final rotational speed, acceleration, and fume exhaust contribute to how the properties of coated films are defined. Schematic diagram of a spin coater along with main components is shown in Figure 1.12a and a very simple process of spin coating flow chart is shown in Figure 1.12b.

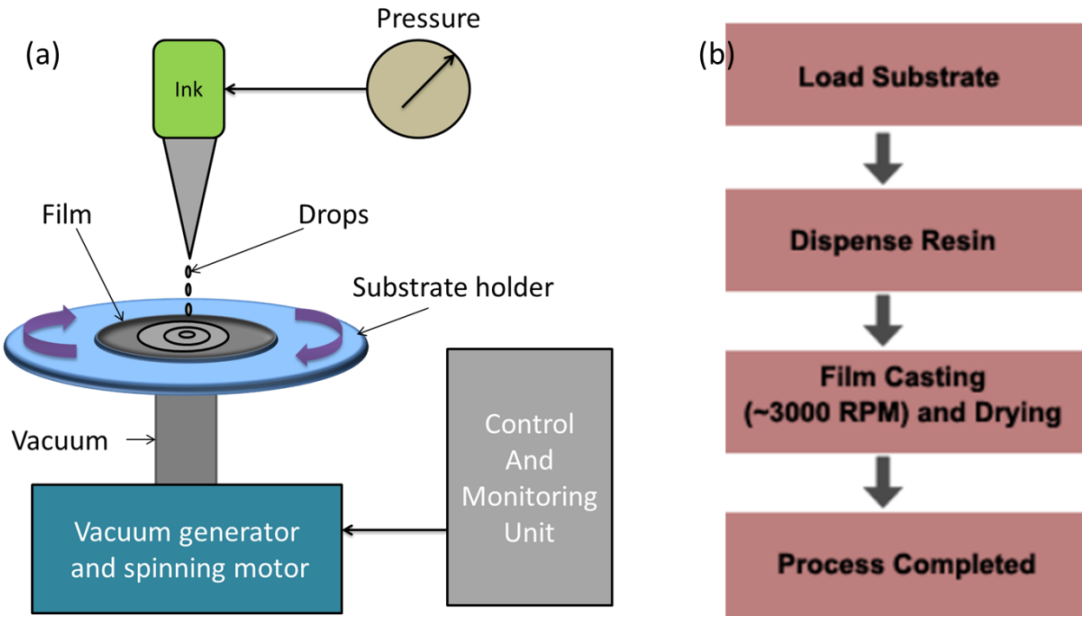

Figure 1.12. (a) Spin coater schematic diagram. (b) Simple spin coating process.

1.6 Objective of the Thesis

Printed electronics is new emerging field that allow lost cost, large area, flexible and environmentally friendly applications. Some devices are matured and already have been used in electronic applications such as OLED display, RFID tags and biomedical sensors etc. Since printed electronics is new field there is big room yet in the advancement of the printed electronics. Among the recent challenges of the printed electronics are: the fabrications techniques, encapsulation and reliable materials. The main objective of thesis is to address these challenges by exploring new functional materials to fabricate the electronic devices such as memristors, crossbar memory array, biomedical sensors, resistors, capacitors and diodes, etc. Organic and inorganic materials are synthesized to make them spray able that enable large area fabrication.

Current passive crossbar memories (ReRAM) are suffering from inherent problem of sneak currents. This problem is minimized by introducing new techniques and devices such pull-up resistors and asymmetric memristors. Apart from this, a new device is introduced that memories the on/off state and emit light that can be used in display applications in matrix form. Low cost, ambient conditions manufacturing techniques are studied and utilized for the fabrication of these devices such as EHD, ink-jet printing and spin coating. The optical, chemical, mechanical and

electrical characteristics and statistical analysis has been carried out to make sure the reliability and direct printability of the electronic device.

1.6.1 Outline of thesis

The thesis is organized into eight chapters as under:

Chapter 2 deals with the memristor working, fabrication and characterization of graphene quantum dots and zinc stannate on PET substrate. These devices are fabricated with EHD technique. Resistive switching properties and resistive switching mechanism are investigated in the fabricated devices. This chapter also describes the fabrication of flexible resistive switch.

Chapter 3 deals with the memristor circuits such as single bit voltage divider memory and memristor-capacitor based filters. The voltage divider memory consisted of one organic resistor (MEH:PPV) and one memristor (ZrO). These devices are fabricated with EHD technique and characterized for electrical and surface morphology.

Chapter 4 deals with fabrication of the memristor based nonvolatile memory includes tristate memory/crossbar memory with pull-up resistors. Tristate memory can be switched in three distinct memory states that allow on/off ratio of 6000. The memory with pull-up resistor allow parallel readout and minimizes the inherent sneak current problem.

Chapter 5 describes sneak current minimization, the value of the pull-up resistor is statistically optimized and simulated in matlab to analyze the performance of the passive crossbar array. This chapter also presents ultra-asymmetric memristor that allows current in one direction and controls the sneak current in a crossbar array.

Chapter 6 presents state memorable OLED (SM-OLED) device which consist of Ruthenium and PMMA composite with a thin layer of graphene layer on top. These two layers are sandwich between bottom electrode ITO and top electrode aluminum. This device memorize its last operated state and emits lights if it was in on state. It is programmable into two states on and off state.

Chapter 7 describes humidity and temperature sensors which are fabricated through inkjet material printer at ambient conditions. The humidity sensor sense %RH from 5-95% with sensitivity of ~96. For sensing the humidity, the sensor utilizes graphene and methyl-red composite film. The

temperature sensor is based differential meander patterns to compensate the bending effects in the flexible applications. The sensor is based on three terminals, the consecutive terminals provides strain sensing while first and third terminals provides bendable temperature sensing.

Chapter 8 deals with organic diode for rectification applications and fabricated on a glass substrate through EHD technique. The diode utilizes TPD and C_{60} organic materials for p-type and n-type semiconductors sandwich between ITO and Aluminum.

Chapter 9 presents conclusion of the thesis and future work.

1.7 References

[1] Jurvetson, S. Olympus Stylus [Photograph]. 2004. [Accessed on 19.12.2013]. Available at: http://www.flickr.com/photos/44124348109@N01/2265519
[2] R. M. Pasqualrelli, et al.,Chem. Soc. Rev., 40, 5406–5441,2011.
[3] B. Derby, Annual Review of Materials Research, 40,1, 395–414, 2010.
[4] DMP-3000 Materials printer manual.
[5] Lim J. A., et al., Adv. Funct. Mater., 18: 229–234,2008.
[6] R.P.A. Hartman, EHD Atomization in the Cone-jet Mode, Ph.D. Thesis, TU Delft, 1998.
[7] Jaworek, Powder Technol. 176 (2007) 18.
[8] S.R. Samarasinghe, et al., Appl. Phys. A-Mater. Sci. Process. 91 (2008) 141.

Chapter 2 Memristors

2.1 Memristor

In the classical electronics, there are only three fundamental 2-terminal passive circuit elements the resistor, the inductor and the capacitor. Based on simple symmetry arguments Leon Chua claimed that a fourth fundamental 2-terminal passive circuit element is necessary to complement the other three [1]. More specifically, Chua realized that out of the six possible pairwise combinations between the four fundamental circuit variables, namely, the current, voltage, charge, and flux-linkage, only five had been identified. He therefore postulated mathematically the memristor as the element relating the charge and the flux-linkage in order to establish the missing link (see Figure 2.1). In 2008, HP lab demonstrated the first physical memristor based on resistive switching in doped TiO_2 [2]. In 2010 Chua confirmed that every resistive switching device is a memristor [3]. Memristor can be switched between two resistive states, low resistance state (LRS) and high resistance state (HRS) through external voltage bias. This particular feature makes it a transistor less switch that can be fabricated in very small size. Since that, it researched widely in the electronics field for the future non-volatile memory applications.

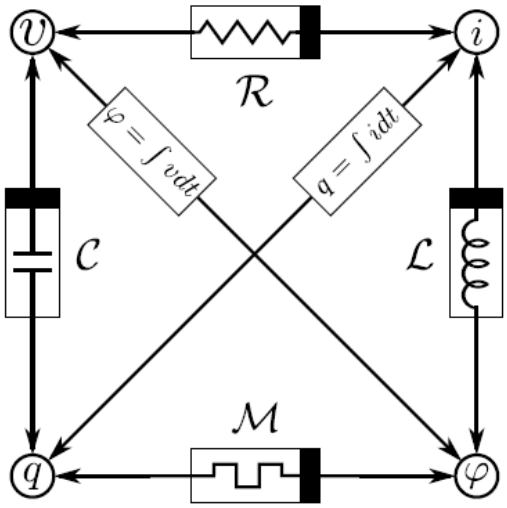

Figure 2.1 The diagram shows the six possible binary relations between the four fundamental circuit elements.

Resistive crossbar passive memories (ReRAMs) based on resistive switching is considered the next generation non-volatile memory (NVM) because of its ample advantages over the flash memory.

As CMOS technology is reaching its limits in sense of materials, device size, fabrication plants and economics, ReRAM is the only hope to counteract the upfront challenges to the electronic industry. Resistive switches (transistor less) considered as a justified replacement for the memory devices and electrical switching elements have been researched productively for many. Solid electrolyte sandwiched between two metallic electrodes is considered to elucidate the reversible resistive switching characteristics. The sandwiched structures exhibit at least two distinct states when are being forced with opposite polarity. The change in the resistance is then exploited for the electrical switching and memory applications. The resistive switching devices are fabricated by simply sandwiching some metal oxide, polymer-based material, perovskite material, or even a vacuum nano-gap etc between two conducting electrodes. The resistive switch provides great data storage density due to its simple device structure. The sandwiched type structures are more reliable because these devices are resistance based so they keep their state unchanged even when the power absence.

2.2 Types of Memristors

As described in the previous section that as compare to an ordinary electrical resistor, memristor can be programmed or switched in different resistive states based upon the history of the voltage signal applied to the device. This phenomenon can be understood in a current-voltage (I-V) curve. Resistive switching are categories into two main types based upon the voltage polarity needed to the device operation.

2.2.1 Unipolar Memristors

If switching of the resistive switch is independent of the polarity of the voltage/current source and is dependent on the amplitude of the voltage/current then the switching is categorized as unipolar resistive switching as shown in Figure 2.2. As noticed in the I-V curve, set and reset of the device is happening irrespective of the polarity of forcing node. A device in an HRS state can be switched to LRS state by a threshold voltage (V_{TH}) and the current is limited by compliance current (CC) to avoid hard break down in the switching layer of the device. Resetting back to ON-state happens at a same polarity below its V_{TH}. A much higher current can be observed in retting state of the device. Application of CC is not needed in retting of the device. Therefore, both the transition of setting and resetting are possible on both sides of the polarity.

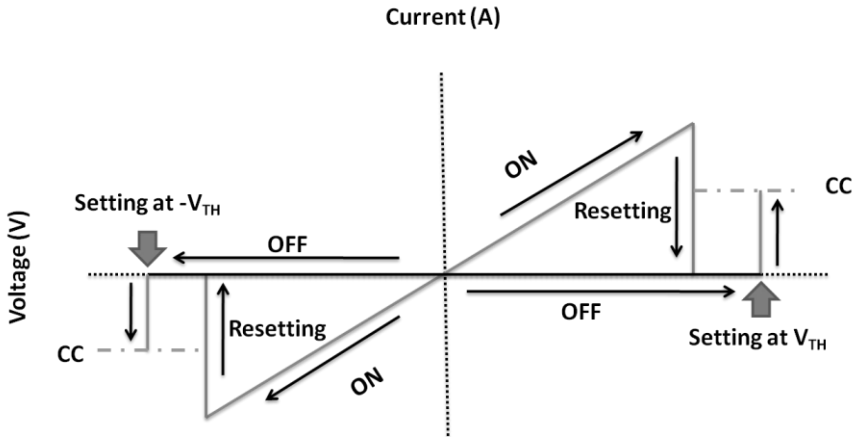

Figure 2.2. Amplitude dependent unipolar resistive switching.

2.2.2 Bipolar Memristors

The behavior of the device in which setting and retting of the device appeared at different sides of the polarity is termed as bipolar resistive switching. In this type of resistive switching, ON-state of the device occurs at some V_{TH} and OFF-state of the device occurs at some specific V_{TH} on the opposite side of the voltage polarity as shown in Figure 2.3. Bipolar resistive switching is also called polarity dependent resistive switching. Current observes in bipolar resistive is much lower as compared to that of unipolar resistive switching.

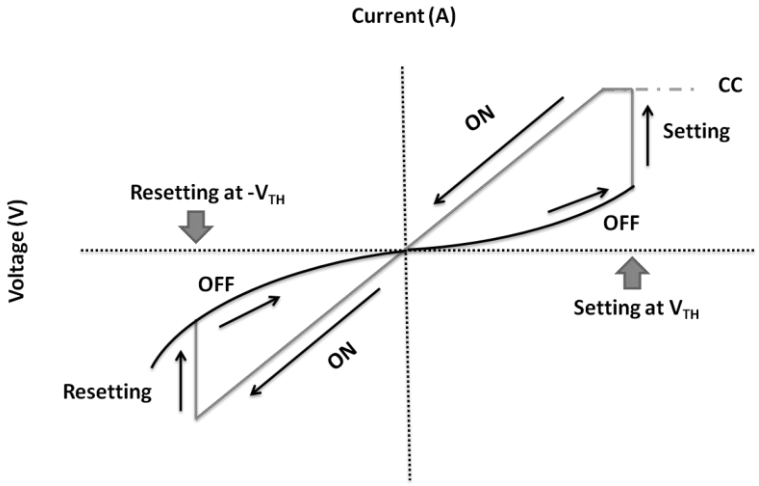

Figure 2.3. Polarity dependent bipolar resistive switching.

2.3 Memristors Mechanisms

Several studies have been conducted for memristive mechanisms involved in metal oxides and polymers based sandwiched structures (Waser and Aono 2007, Sawa 2008, Akinaga and Shima 2010, Lee and Chen 2012, Cho et al. 2011, and Ling et al. 2008). Broadly, the purposed mechanisms are categories into two classes: the bulk effect and the interface effect.

2.3.1 Bulk Effect

The memristive effect that is caused by formation and rupturing of the conductive filaments due to joule heating in the sandwiched material between the two electrodes is termed as bulk effect or thermal effect. Bulk effect is observed common in unipolar resistive switching devices. Forming voltage is usually needed in these types of resistive switching. The filaments are formed by the voltage induced partial dielectric breakdown. These filaments may be composed of electrode material transported into the sandwiched layer, local degradation of the organic film or decomposed insulator material such as sub-oxides. During the resetting state of the device, the filaments are undergone into the rupturing phase hence the device change its LRS into HRS.

2.3.2 Interface Effect

Interface effect is common in bipolar devices. Different models are involved to explain the interface effect in bipolar resistive switching devices. Some common models are explained with the charge injection and trapping of charges in the traps in the insulator/oxide switching material. Traps play important rule when the interface between metallic/conducting electrode and insulator/oxide is schottky. When external potential is provided then the injected charges are trapped in the interface between conducting electrode and insulator. When sufficient number of charges are gathered in the trap site eventually the scenario overcomes the barrier between metal-insulator interface and large current starts to flow through the interface. Contrary when the biasing is reversed then again the schottky barrier establishes and changes the device state to its original HRS.

2.3.3 Redox Process Induced Cation Migration

This model is based on the redox reaction of the metallic electrode. When one of the electrodes is chemically reactive while the other conducting electrode is inert then cations migrate in the ionic conductor. Chemically reactive electrode (Ag or Cu etc) undergoes oxidation reaction when force with some potential. The drift of cations (such as Ag^{+} or Cu^{+} etc) in the ion-conducting layer and

their discharge at the counter electrode form a highly conductive path results in setting the device into the ON state. When the polarity is reversed, the conductive path undergoes into the electrochemical dissolution and resetting the device into the OFF state.

2.3.4 Redox Process induced Anion Migration

Anion migration model is based on the chemical redox reaction of insulator/oxide. This is the mechanism in which resistive switching takes place by the migration of anion/oxygen ion towards anode or better described by the migration of oxygen vacancies towards cathode. This model is also termed as oxygen vacancy migration resistive switching model. The migration of anion (oxygen ion) or oxygen vacancy leads to the change in stoichiometry and a valance change of the cation sub lattice. Eventually the state of the device changes to the LRS by the change in the electronic conductivity of the oxide/insulator.

2.3.5 Formation and Disruption of Metal Oxide

In some of the reports, the resistive switching effect was attributed to the formation and disruption of the metal oxide between the metallic electrode and oxide interface. When a potential is applied to the device, metal oxide formed due to the electrochemical reaction between the electrode material and sandwiched layer.

2.4 Graphene quantum dots based memristor

Memristor is consisted of metal insulator metal (MIM) structure; the insulating layer is made of various materials having switching property. Among the present available materials graphene is the most dominant material for the electronic industry because of its extreme electrical, mechanical, and thermal characteristics [4],[5]. Graphene is considering as the future material of electronic industry, and many researchers presented that all the devices and integrated circuits would be fabricated from graphene instead of silicon [6]-[12] . Especially, graphene quantum dots (G-QDs) are semiconductor nano crystals that they have typically diameter size between 1~20 nanometer (nm) [14]. Due to versatile properties of G-QDs, it is extensively researched for electronic devices [15]. Graphene quantum dots exhibits resistive switching and provide linear resistance at the cost of low resistance during HRS and LRS. Low resistance problem of the graphene QDs can be improve by attaching it with other materials having property of switching [16]. In combination with

high resistance material, graphene quantum dots can offer high resistance (during HRS and LRS of resistive switch) and high OFF/ON ratio.

A highly stable resistive switching device based on graphene quantum dots and polyvinylpyrrolidone composite (G-QDs/PVP) fabricated on flexible substrate is demonstrated. The G-QDs and PVP are blended to get the semiconductor property of G-QDs while holding a resistance state (linear) and filament conduction property of PVP during transition from one state to another state (switching) in the device. Without PVP, the G-QDs offer low resistance that is not feasible for high dense circuits as electrical power constraint, PVP drastically reduced the current of both states of memristor in this research work. PVP is organic insulator and solvable in number of solvents, here we blend PVP with graphene quantum dots to achieve fully organic active layer. Furthermore, the PVP is fully unified able with G-QDs that help in uniform deposition during EHD. The active layer is sandwiched between top and bottom silver electrodes and forming metal insulator metal (MIM) structure [17]. The fabricated device has morphologically characterized by microscopic images, Scanning electron microscope (SEM) and Focused Ionic Beam (FIB) analysis. The elemental composition characterization is carried out by X-ray photoelectron spectroscopy (XPS). The device has been electrically characterized with the semiconductor analyzer to evaluate the current–voltage (I-V) characteristics in order to illustrate the memristive behavior. A 3×3 crossbar array is demonstrated, and each memristor of the array is accessed randomly through rows and columns without crosstalk. Physical endurance of the device has been tested, after being physically flexed, for flexible electronics applications. The proposed device can be used in flexible resistive stable non-volatile random access memories and can be used in binary switching purposes as well.

2.4.1 Fabrication

Ink for active layer is prepared as: Graphene quantum dots (sigma Aldrich) 10mg is dispersed in 1 ml ethanol, stirred on magnetic stirrer for 2 hours and 30 min bath sonicated. PVP powder is dispersed 10 % by weight in ethanol and stirred for 1 h on magnetic stirrer. Both inks were prepared separately and then mixed with different ratios to obtain the optimum switching of the device. The best ratio experimentally observed of G-QDs and PVP was 1:1/2. Other mixing ratios resulted in asymmetric threshold voltages, small OFF/ON ratio, and small endurance cycles. After mixing the ink with said ratio, it was again stirred with magnetic stirrer for 30 min and 10 min bath sonication prior to use. Ink for silver electrodes is prepared as: Ag nano particle paste sigma Aldrich 55%wt

is diluted in 10 ml ethylene glycol solvent mixed for 1 hour on magnetic stirrer and then 20 min bath sonication. Ag ink has a surface tension of 24mN/m, viscosity of 11.3mPa.s, and specific gravity of 1.66gm/ml.

Substrate of the devices was placed on the moving stage; electric potential was applied to the nozzle through the high voltage source and ground to substrate holder. The proposed devices are fabricated by using a stable cone-jet mode of EHD. Resistive switching devices were fabricated on PET substrate as the layout diagram shown in Figure 2.4a. To begin with, bottom silver electrodes (200µm width) were deposited with the EHD parameters given in Table 2.1 and cured for 90 min at 120 °C. Composite in of G-QDs/PVP was placed in chamber and pumped to nozzle for the active layer deposition (97nm thickness), the parameters for EHD atomization during deposition of the active layer are given in Table 2.1. For the fabrication of thin patterns for the electrodes of the device, the distance between nozzle and substrate (stand-off) is reduced to 1~3 mm, whereas the distance to deposit the active layer is increased up to 15mm. Along the stand-off distance the cone jet converts into spray and more area is covered on the substrate resulting in deposition of thin film. In the case of small stand-off distance it covers area almost equal to the diameter of the nozzle and deposits thick film (patterns).

Table 2.1. EHD parameters for the deposition of silver electrodes and G-QDs/PVP composite active layer.

Layers	Applied Voltage (KV)	Applied flow Rate (µl/h)	Stand off Distance (mm)	Substrate Velocity (mm/s)	Nozzle inner Diameter(µm)
GQDs/PVP	4.2	120	14	3	110
Ag	6	20	2	1	10

After fabrication, sample was cured at 120 °C for 120 min, and then top electrodes were deposited with the same EHD parameters as the bottom electrodes. Contact pads were deposited on the ends of both bottom and top electrodes ends for external circuitry interfacing. After the fabrication and curing process, sample was encapsulated with Al_2O_3 to protect from environmental effects such as oxidation. The fabricated device is shown in Figure 2.4b, top and bottom electrodes are visible because the active layer is transparent. Pads are relatively thick to provide robust interface with external circuits and equipment. Top right inset shows zoomed image of the cross bar point of silver electrodes, and left top inset shows zoomed image of silver electrode. The active layer of the fabricated array was analyzed for the surface morphology by FE-SEM Jeol JSM-7600F as shown

in Figure 2.4c, which shows the film is properly and uniformly deposited. Film thickness plays a vital role in memristive behavior. Different samples were prepared to check the optimum film thickness for the memristive behavior. The film thickness can be varied by varying the spray time (number of passes) and ink flow rate. The film thickness was measured with the thin film thickness measurement system K-MAC ST4000-DLX, and the thickness of the fabricated devices is around 97 nm. The inset of Figure 2.4c shows the FIB image of the cross sectional view of the device sandwiched active layer between two electrodes.

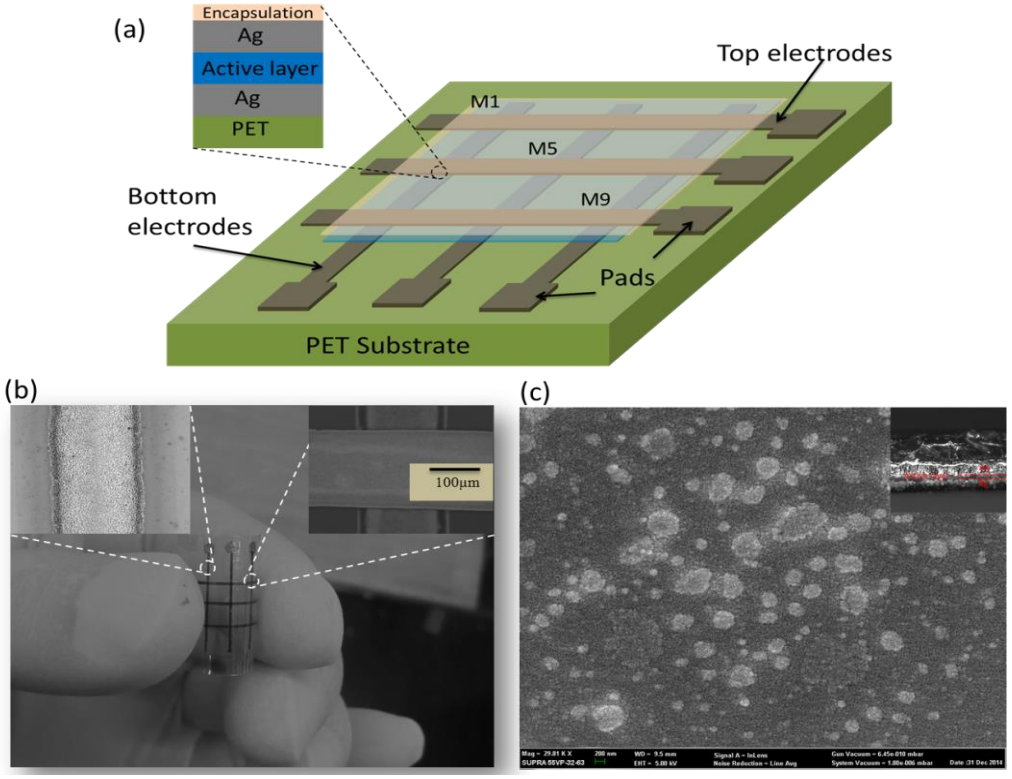

Figure 2.4. Fabrication of device.
(a) Schematic diagram of 3X3 memory array based on graphene quantum dots (G-QDs) and PVP composite. Bottom electrodes (Ag) are deposited on PET then active layer (G-QDs and PVP composite) and lastly top electrodes of (Ag). The device is encapsulated with Al2O3 . The cross sectional view is shown in the inset. (b) Fabricated 3x3 memory array device based on G-QDs and PVP composite, and silver electrodes along contact pads are visible whereas active layer is transparent. The zoomed image of crossbar point is shown in the right top inset and zoomed image of silver electrode is shown in the left top inset. (c) Scanning Electron Microscope (SEM) image of the G-QDs/PVP layer and inset shows the cross sectional view of the device at crossbar points.

2.4.2 Characterization

Agilent B1500A Semiconductor Device Analyzer is used for the electrical characterizations of the resistive switching array. The device was placed in the probe station and probes were connected to the rows and columns (bottom and top electrodes) consecutively. Before starting resistive switching operation, a positive voltage sweep (0~2V) was applied to establish the conducting paths and to get

a soft breakdown, which is necessary for the stable reversible resistive switching operations [18],[19]. After initial electroforming process, the samples were biased with a double voltage sweep from -2 to 2 V with a current compliance of 100 µA. The device showed a Lissajous curve with two distinct states, RON and ROFF as shown in Figure 2.5a. Memristor goes from LRS to HRS (set) at 1.5V and retains this LRS state until -1.65V, where the device goes back from LRS to HRS (reset). The resistance of the HRS state was observed to be 120 kΩ and of LRS 11 kΩ at reading voltage of 1V. All resistive switching devices were analyzed by selecting the row and column of the specific device from M1 to M9 as shown in Figure 2.4a. To analyze the devices, dual polarity voltage sweeps from -2 to 2V were applied with current compliance of 100µA. The entire devices exhibited resistive switching behavior with a small change in state resistance as shown in Figure 2.5a. The devices turn ON/set and turn OFF/reset voltages are different from each other with a small change from 1.5 to 1.7V for set and from -1.5 V to -1.8 V for reset were observed. Figure 2.5b shows the absolute current analysis graph of the proposed resistive switching device, after going through the complete cycle of biasing voltage (-2~2V and 2~-2V) the device was in HRS state as it was started from this state initially. Here it can be noticed that on both sides of the polarity the graph passes through zero current that defines the memristive behavior. All memristors of the 3×3 array were analyzed for the current voltage analysis for the comparison purpose with each other. The absolute current voltage graphs of the 9 devices of the memory array is clear that, all devices exhibits resistive switching as their currents passing through 0V when the polarity of voltage alternates. States of the devices are starting from "1" (HRS) followed by "2" which is transition from HRS to LRS then voltage sweep go back and passes through "3" which is LRS state and at -1.6V it goes again to HRS through "4" as mentioned in the figure. To analyze the variability of the devices with in the array of 3×3, their state resistances (HRS and LRS) were measured at 1V for 50 times each and average resistance is calculated. Average resistance of HRS and LRS of all the devices of the array were measured as shown in Figure 2.5c. A small changes in the HRS and LRS of the devices were observed, and these results ensures that the devices are highly stable and can be used for parallel switching as all devices have same characteristics.

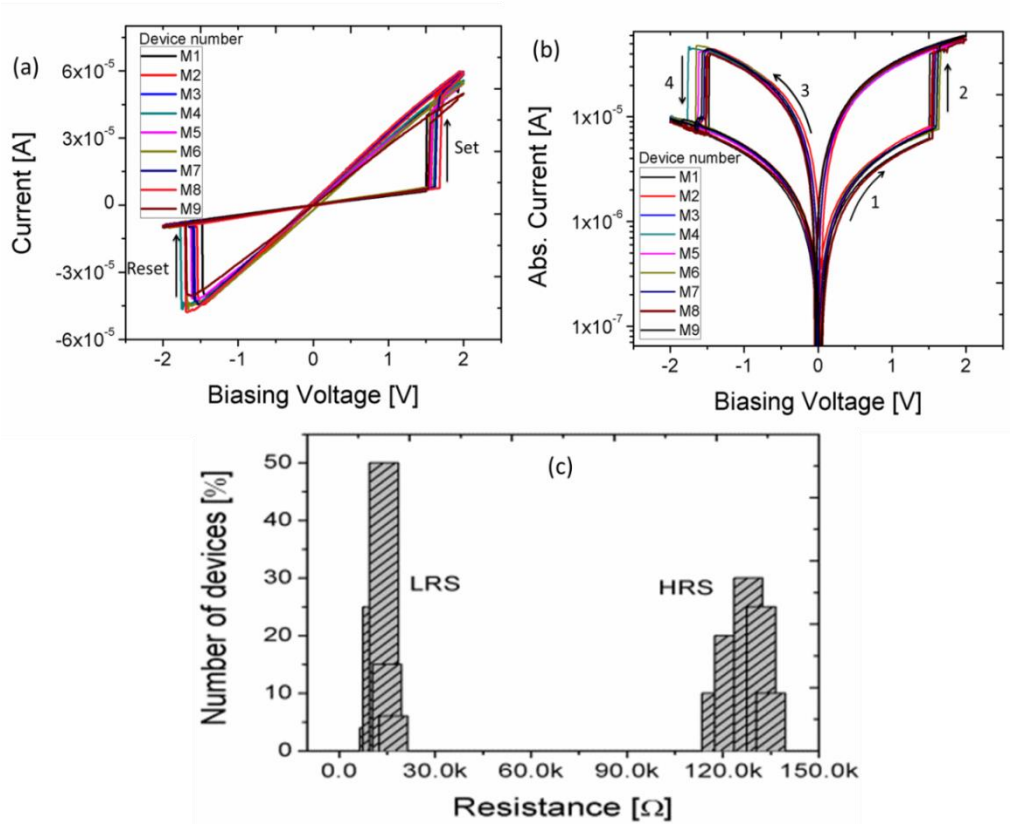

Figure 2.5. Current voltage (I-V) analysis of the 9 memristors fabricated in array form of a 3×3 matrix. (a) Typical current-voltage (I-V) curve of the memristive M5, turn ON (Set) voltage is 1.6V and OFF (Reset) voltage is -1.7V. Ohmic conduction analysis of the device states (LRS and HRS) on the Log-Log scale, comparison with a linear fit, top left inset shows LRS state, and right bottom shows HRS state. (b) Absolute current-voltage analysis of all nine memristors. (c) The histogram of the resistance values in HRS and LRS states of all devices to analyze variability for the memory.

Switching mechanism in the fabricated resistive switch has been explained with the help of slope fitting in the I-V graph as reported in the literature [20]. I-V graph has been drawn in Log-Log scale for the LRS as shown in Figure 2.6. The fitted slope (solid line) has been shown to be around "1" that ensures the ohmic conduction during the LRS/ON state of the device. I-V graph in the Log-Log scale for the HRS/OFF state of the device is shown in Figure 2.6. The calculated slope after fitting the linear line is around "1" that also demonstrates the ohmic mechanism in the fabricated device. Hence both the states of the fabricated device are governed by ohmic conduction. As noticed in the current voltage performance of the fabricated resistive switching device, almost symmetric I-V behavior has been elucidated instead of the asymmetric top and bottom electrodes. These symmetric characteristics are ascribed to the bulk conduction instead of the interface conduction. This stable and perfect bipolar behavior is due to the electrochemically

formation of the carbon conducting channels in the LRS of the device and the dissolution of the carbon conducting paths in the HRS of the resistive switch.

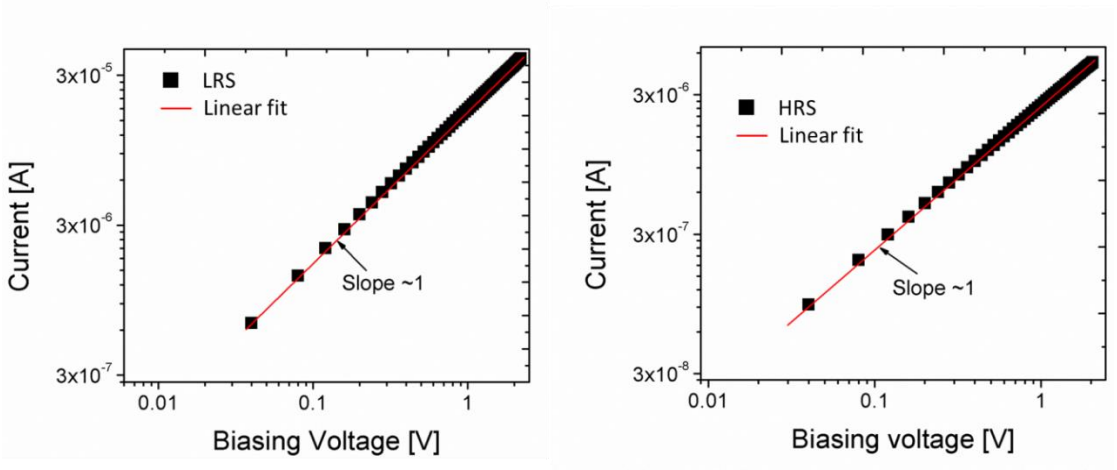

Figure 2.6. Ohmic behavior analysis of the device for HRS and LRS states.

Endurance test of the fabricated device is depicted in Figure 2.7a. The robustness of the proposed resistive switch is checked against 500 biasing voltage cycles. Device number 5 of the memory array was randomly selected, the switch demonstrated reasonable endurance against multiple voltage sweep stresses. As noticed in the endurance test, LRS of the fabricated device is more stable as compared to the HRS shown on the log scale. The change in LRS during the endurance test has been noticed from around 8 kΩ to 13 kΩ and the change in HRS is found to be from98 kΩ to 112 kΩ. Voltage of 1 V has been used as reading voltage for the resistance calculation in the graph. The non-volatility of the as fabricated device was measured over 30 days, and no prominent resistance change was found during both the states (HRS and LRS) of the device under test as shown Figure 2.7b. It has found that the change in resistance of LRS state was more as compare to HRS along the time, but until 30 days there is no overlap. The memory array was analyzed for its mechanical characteristics by bending it on different diameters. For this test, a random device was selected (M3) and memory array was wrapped around metallic rod having diameter from 26 to 5 mm. The way down until 8mm diameter the device showed normal behavior for both HRS and LRS states with a negligible change in resistance as shown Figure 2.7c. bending beyond 8mm the device showed high resistance as the silver electrodes broken due to mechanical stress. To ensure the reliability against bendability, the array was bent over 8mm diameter for more than 1000 endurance cycles as

shown in Figure 2.7d. For 1000 bending cycles, the device showed negligible change in both state resistances.

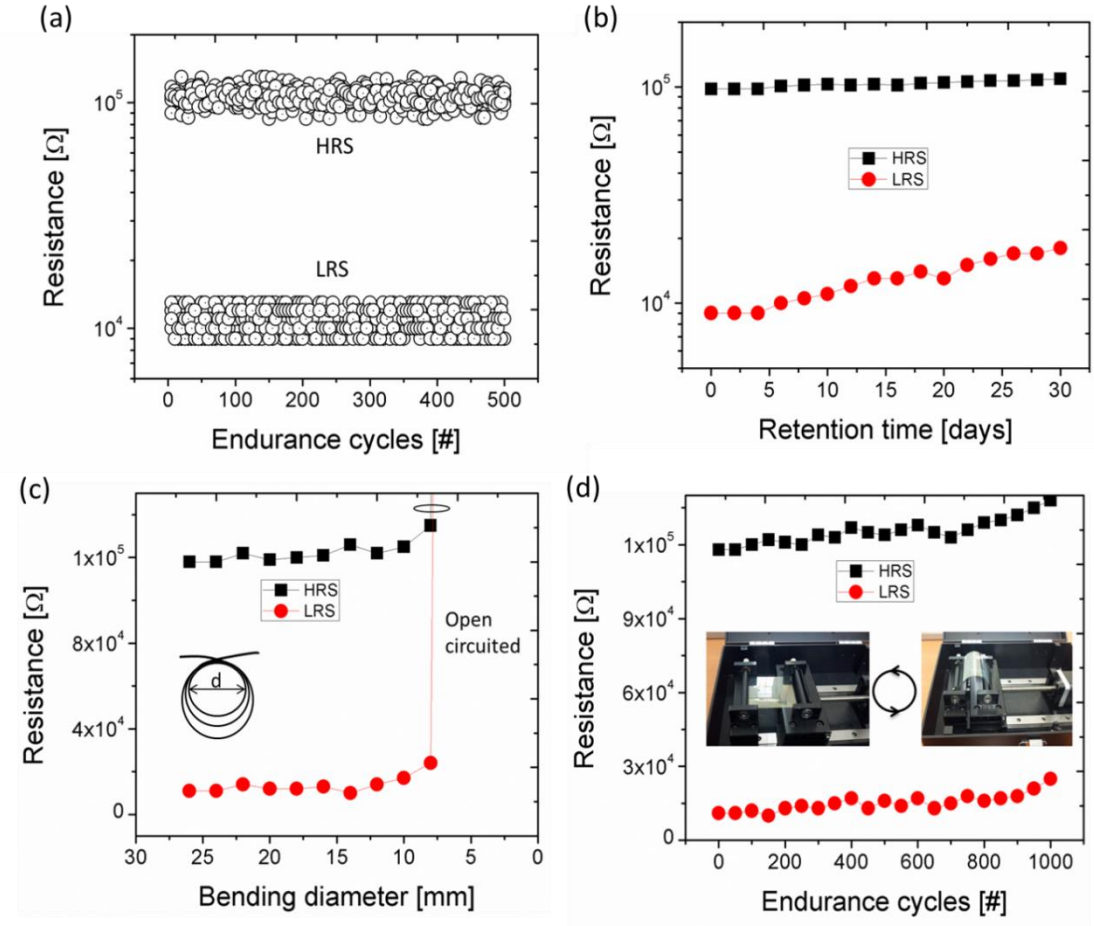

Figure 2.7. Electrical and mechanical characterizations of the proposed memristor. (a) Endurance analysis of the device number 5 for 500 cycles. (b) Retention time analysis of the 5th device of 3x3 memory array for 30 days. (c) Bending the device over different diameters by using metallic rods having diameter from 26 down to 5 mm. (d) Endurance cycles of the device by bending at 8 mm diameter through automatic bending machine for 1000 cycles.

The elemental compositional analysis was carried out through X-ray photoelectron spectroscopy (XPS) theta Probe AR-XPS System. Figure 2.8a depicts the XPS survey spectrum of G-QDs, where O 1s peak is ascribed at 532.77 eV, N 1s peak is ascribed at 399.65 eV, and C 1s peak is ascribed at 284.6 eV. Figure 2.8b shows the high-resolution XPS spectra of the O 1s peak of the G-QDs, that starts at 536.7 eV and ends at 529.6 eV. Figure 2.8c depicts the XPS survey spectrum of the PVP film fabricated on a PET substrate, O 1s peak is ascribed at 532.29 eV and C 1s peak is ascribed at 284.6 eV. Figure 2.8d depicts the XPS survey spectrum of the composite film fabricated on a PET substrate, peaks of the O1s and C 1s are almost at the same eV values therefore, they are overlapped whereas the N 1s peak from G-QDs can be seen in the

spectrum. The characterizations of the resistive switching devices lead toward the proliferating applicability of the fabricated devices for the flexible, robust, and durable printed electronic memory applications.

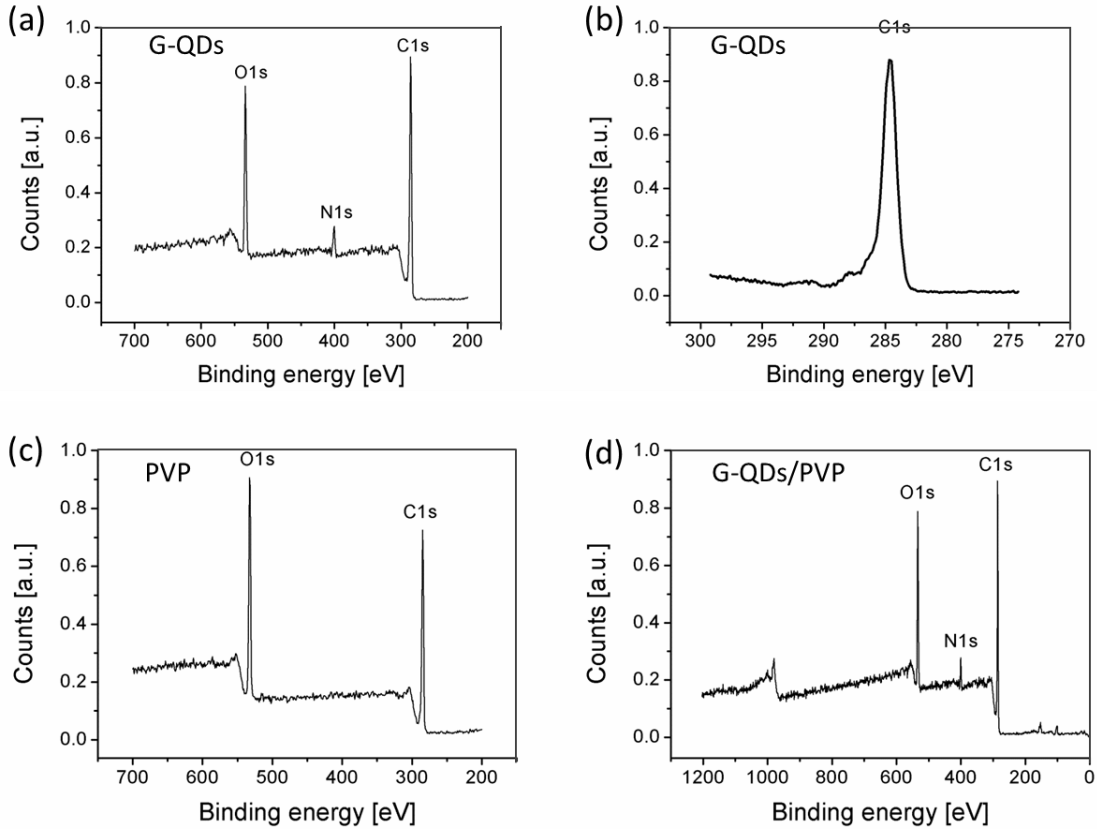

Figure 2.8. XPS analysis spectrum of the samples fabricated on a PET substrate. (a) Graphene quantum dots G-QDs. (b) High resolution O 1s spectra of the G-QDs (c) XPS spectra of PVP on PET substrate. (d) XPS survey spectrum of G-QDs/PVP film on PET substrate.

2.4.3 Summary

In summary, highly stable and long retention time resistive switches has demonstrated. The construction of the device is Ag/(G-QDs/PVP)/Ag fabricated on a flexible substrate PET through EHD technique (active layer thickness 97nm). The proposed switching devices were fabricated in 3×3 crossbar array with uniform parameters. Electrical characterization of the ORSD was carried out by accessing individual elements through rows and columns. The proposed devices exhibited the OFF/ON ratio ~14, the endurance cycles of more than 500 and the retention time over 30 days. The threshold voltage and electrical state resistance (HRS and LRS) of all the devices were found to be very stable. The devices have also demonstrated bendability down to 8 mm diameter for more

than 1000 endurance cycles. In the result of these characteristics of the proposed resistive switching devices, they have full potential to be used in flexible, high performance, and long retention memory applications.

2.5 Zinc stannate ($ZnSnO_3$) based memristor

The $ZnSnO_3$ material is sandwiched between bottom ITO and top silver electrode to make metal insulator metal (MIM) structure of a single memristor. Multiple memristors are fabricated on a single substrate with common bottom electrode and active layer with same fabrication parameters (active layer thickness) to investigate variability. The fabrication facility EHD is operated at ambient conditions and 35 % humidity level throughout the experiment. The device is characterized electrically, mechanically, and for surface morphology by using probe station, automatic bending machine, XRD and FE-SEM. The proposed device exhibited a stable resistive switching behavior for more than 200 cycles, good retention time, and flexibility down to 8 mm. As the memristor architecture is very simple, metal insulator metal (MIM), it can be fabricated with variety of fabrication techniques including sol-gel, spin casting, electrostatic spray deposition (ESD), electro hydrodynamic (EHD), roll to plate, and screen print [21]-[25]. All fabrication techniques have their advantages and disadvantages. Some of them need vacuum chambers, heat, and a special environment to process the fabrication of a device. Among them, the EHD is eco-friendly process that is suitable at ambient conditions for prototyping and mass production [26]. More details about EHD fabrication can be found in our previous work [27].

The proposed device is fabricated by using EHD technique as following: (1) An ITO coated PET substrate sample of 2×2 cm^2 was cut and treated with ethanol, DI water and UV respectively, (2) active layer was deposited on ITO coated PET and cured, (3) lastly silver electrodes were deposited and cured again. Fabrication of the proposed device is discussed in section 2, characterizations are described in section 3, and conclusion is given in section 4.

2.5.1 Materials and fabrication of the proposed device

Ink for the active layer of the memristor was prepared as Zinc stannate ($ZnSnO_3$) powder 0.78 gm was dispersed in 20 ml ethanol and 0.15 ml of ethanolamine was added. Solution was placed on magnetic stirrer for 24 h at 70 °C, and then bath sonicated for 10 minutes and filtered with 5 µm filter. Prepared ink was mixed with N-N Dimethylformalehye (DMF) with ratio 1:0.25 to increase

the electrical conductivity of the solvent to enable the electrostatic deposition (ESD) phenomenon. For silver electrodes, ink was prepared as: Silver (Ag) nano-particle paste 55%wt was diluted in 10 ml ethylene glycol solvent, ink was mixed for 1 hour on magnetic stirrer and then 30 min bath sonication.

Prior to begin with EHD printing, the substrate was treated with ethanol and deionized water for 10 min each followed by ultraviolet UV ozone for 5 min. Ink solution was pumped to a metallic nozzle to deposit on the ITO coated PET. While tuning the EHD for stable cone jet for Ag and zinc stannate inks by varying applied voltage and ink flow rate, different modes of spray were observed including dripping mode, unstable cone jet mode, stable cone jet mode and multi cone jet mode were observed as discussed in chapter 1. We got the EHD optimum parameters for zinc stannate experimentally by applying ink flow rate as starting from 50 µl/h and increasing to 800 µl/h with incremental step of 50 µl/h and applied voltage from 0 kV to 8 kV. The same procedure was applied for the Ag electrodes deposition. We found that 200 µl/h and 4.2 kV was the optimum parameters for stable cone-jet of zinc stannate with 210µm internal diameter of nozzle and for Ag electrodes 6 kV, 60 ul/h and 110 µm inner diameter of nozzle. Parameters of the EHD system during deposition of the active layer and silver electrodes are given in Table 2.2.

Table 2.2. Operating parameters of the EHD deposition process.

Layers	**Applied Voltage (KV)**	**Applied flow Rate (µl/h)**	**Stand off Distance (mm)**	**Substrate Velocity (mm/s)**
$ZnSnO_3$	4.2	210	11	1
Ag	6	20	1.2	3

Firstly, the active layer of $ZnSnO_3$ was deposited and cured at 130 °C for 4h. Afterward, the Ag top electrodes were deposited (350 nm) on the active layer and cured at 80 °C for 30 m. fabricating multiple memristor devices on a single substrate as the layout diagram is shown in Figure 2.9. All the devices sharing the active layer and bottom electrodes, whereas the top electrodes are separately deposited for each device. The fabricated memory device is shown in Figure 2.9b, the inset shows zoomed image of the devices where PET substrate, active layer and top Ag electrodes can be seen.

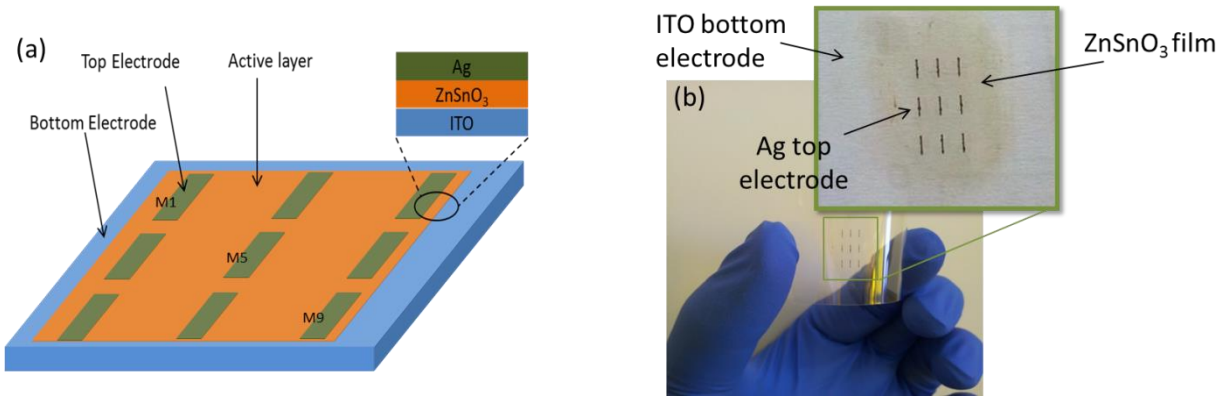

Figure 2.9. (a) Layout diagram of the memory devices on a single substrate, (b) Fabricated memory devices on PET substrate through EHD system, the inset shows zoomed image of the devices showing substrate, active layer and top electrodes.

2.5.2 Characterizations

2.5.2.1 Surface morphology

The EHD fabricated memory devices were analyzed for their morphology characteristics by using FE-SEM.

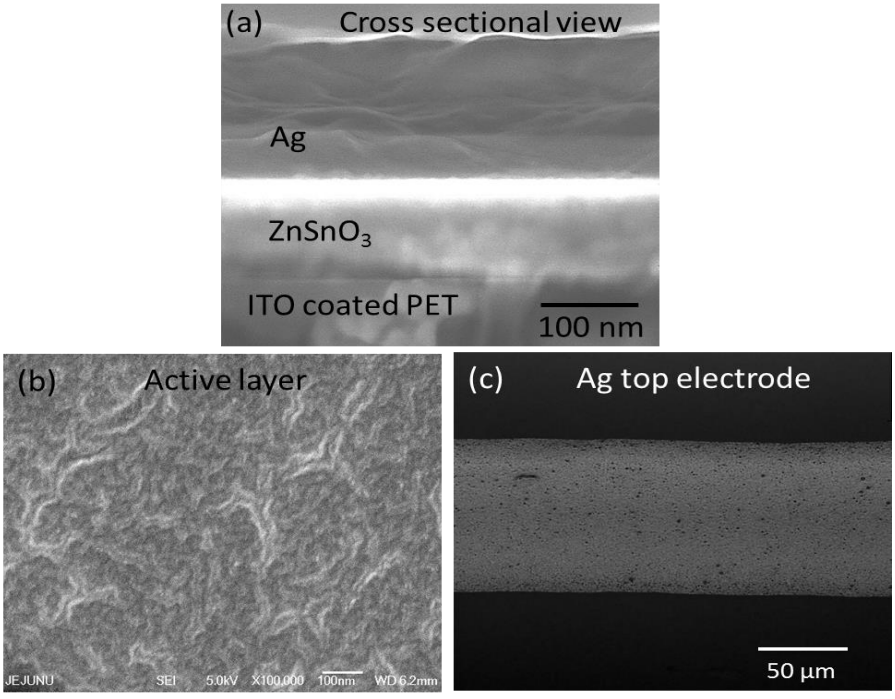

Figure 2.10. (a) Cross sectional SEM image of the device showing PET/ZnSnO3 layer/Ag, (b) FE-SEM image of $ZnSnO_3$ active layer deposited through EHD, (c) Zoomed image of the silver top electrode.

Figure 2.10a shows the cross sectional FE-SEM image of the single resistive device, it can be seen that the active layer is properly deposited over the ITO coated PET substrate. Although the active layer and top Ag electrodes are deposited through open air operated EHD system, even though the layers are properly deposited with a little bit variation in the thickness. To analyze the active layer for more surface morphology details, FE-SEM image was taken as the image is shown in Figure 2.10b. This shows that the film is uniformly deposited and properly centered. The silver electrodes were analyzed with microscope to make sure the physical structure. It was observed that the electrodes are properly deposited with average width of 100 µm and thickness of 350 nm, as the zoomed image is shown in Figure 2.10c.

2.5.2.2 Electrical characterization

$ZnSnO_3$ based resistive memory device was characterized for its electrical characteristics by using Agilent B1500A Semiconductor Device Analyzer. Memory device was placed in an adjustable samples holder inside the probe station and probes were connected to the individual devices of the memory array to check all the memory cells one by one. The dual polarity voltage sweeps were applied initially ±2 V to avoid damage of the device due to high current, and then gradually the voltage window was increased to find the suitable switching voltage for the device where it can switch fully between HRS and LRS with enough off/on ratio. Experimentally it was found that ±8 V is suitable voltage for the device because in this range of voltage the device showed stable resistive switching. The device showed good resistive switching behavior between -8 to 8 V with 1 µA current compliance as shown in Figure 2.11a. The device showed stable behavior of switching between high state resistance HRS and low state resistance LRS as the inset shows I-V graphs of different memristors of the array in Figure 2.11a.

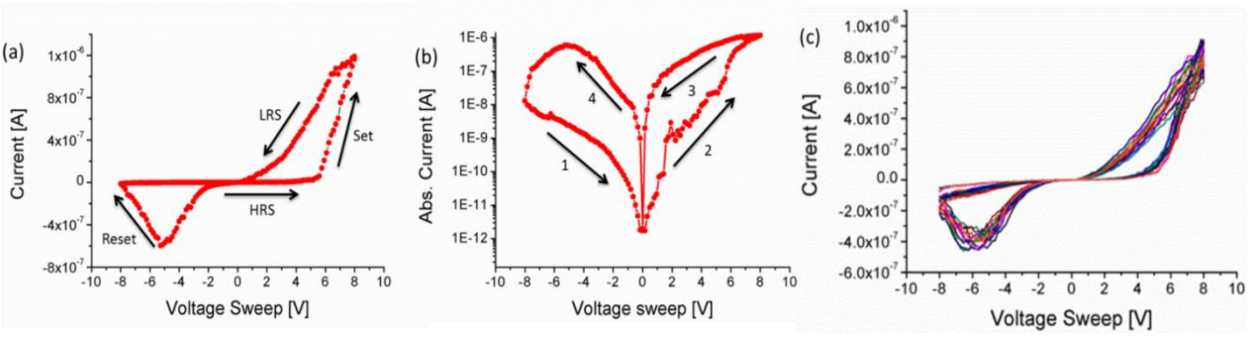

Figure 2.11. (a) Typical current-voltage (I-V) curve of the $ZnSnO_3$ based memristor, the inset shows stability of the device by multiple cycles of I-V sweeps, (b) Absolute current-voltage analysis of the $ZnSnO_3$ memristor.

The reset of memristor occurred around -5.4 V and set occurred around 5.8 V. The off/on ratio of memristor was measured at 5V and observed R_{OFF}/R_{ON} = 33 as an average value for 9 memristors. I-V curves of the 9 meristors are shown in the inset of Figure 2.11a. Individual memristors were tested by providing voltage sweep ±8 V with sampling delay of zero "0" sec.

The maximum operating frequency of Agilent B1500A Semiconductor Device Analyzer was 5 MHz, from the frequency the time of voltage sweep is 0.2 µs, which shows the device switching is sub microseconds. A dual polarity voltage was applied as one terminal to the ITO bottom electrode and other to Ag top electrode of the device. The voltage sweep took the device firstly from its initial state HRS to LRS (at 5.8 V) and again in the reverse sweep from LRS to HRS (at -5.4 V) hence, first memristor M1 remained in its HRS state and then the probes were connected to the next memristor for the testing. Every memristor was tested for more than 200 endurance cycles, this way all the memristors were tested successfully. To confirm the bipolar switching, absolute current voltage analysis was carried out by plotting the I-V curve on semi log scale, the current passes through zero voltage boundaries, which insures the bipolar switching of the device. From this absolute I-V graph, the off/on ratio of the device was measured at -5 V and found to be 300. During the voltage sweep from -8 to 8V, the device did not go in saturation as evident in the inset of Figure 2.11c. Reliability test of the resistive switching device was carried out by selecting a random memristor and switching 200 times for its HRS and LRS resistance values throughout the test, as shown in Figure 2.12a, where the reading voltage of 5 V was used for the measurement of resistances. There was a small deviation in both resistance states HRS and LRS but the ratio between them is negligibly changed until 200 endurance cycles. Retention time analysis of the memory device was carried out on two randomly selected memristors in such way that one memristor is holding HRS and the other is holding LRS state. A 5 V was applied to both memristors and their resistance values were measured. The measured resistance values of the both states were recorded against time for 200 min as shown in Figure 2.12b. A negligible change in resistance value was observed, that ensures good retention property of the device. HRS and LRS data of all devices of the 9 devices was measured at 5 V to compare with each other for the variability from device to device. The resistance values were observed with small changes in HRS and LRS, as shown in Figure 2.12c. The resistance range for LRS and HRS was observed to be 7.5 to 8.5 MΩ and 250 to 298 MΩ respectively. It shows that, all devices are fabricated uniformly and can be switched by same threshold voltage. The small change in the threshold of memristors is due to the uneven deposition of the active layer, as we have used EHD technique. These switches can be used in

memory for parallel read write, as variability is small from device to device in sense of threshold voltage and their state resistances. The achieved results suggest that the proposed resistive switches based on zinc stannate can be used for memory cells in resistive memories.

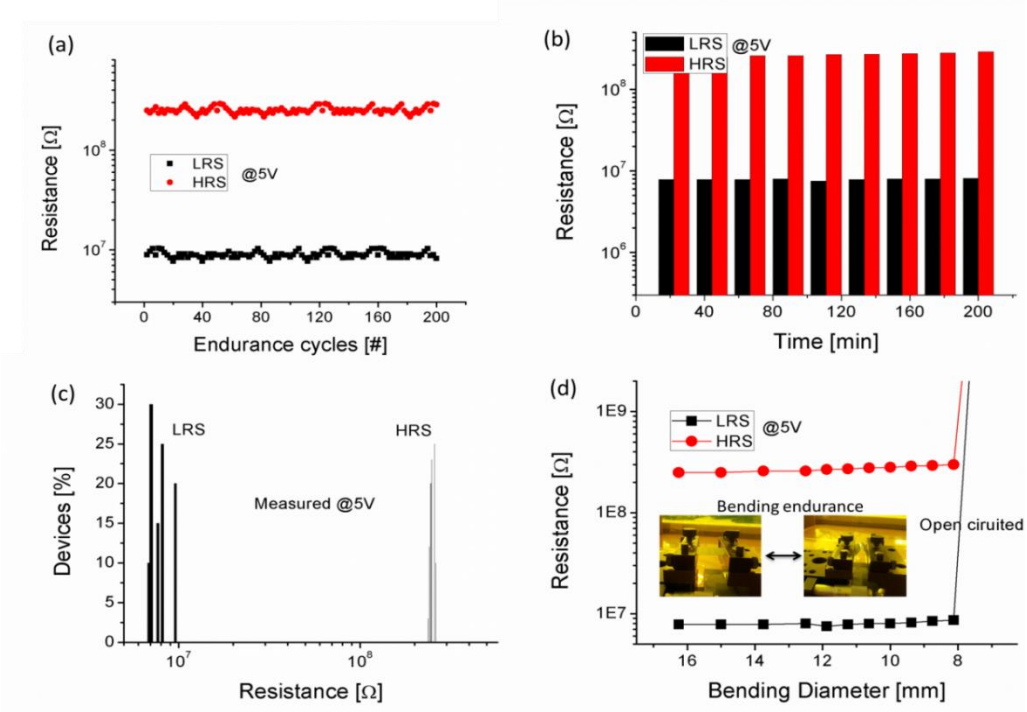

Figure 2.12. (a) Endurance cycles of the memristor for 200 cycles, (b) Retention time analysis of the $ZnSnO_3$ memory device for 200 min, (c) Variability analysis of the 9 memory devices, measured HRS and LRS values, (d) Bending the device on rods having diameters from 18 to 8 mm, the inset shows the automatic bending machine for the bending test.

2.5.2.3 Mechanical characterization

Apart from the electrical properties of the proposed resistive switches, the devices were characterized against bendability to make sure the application of these switches in flexible electronics. The resistive switches array was bent over various diameters starting from 18 to 8 mm. It was observe that the minimum bending diameter is 8 mm, as until 8 mm there is no significant change in the resistive states of the devices. Beyond 8 mm the device showed open circuited behavior as shown in Figure 2.12d. The open circuit behavior of the device was due to the Ag electrodes and active layer, which are sensitive to bendability beyond 8 mm. The endurance cycles of the device were carried out by bending the device on 8 mm diameter by using bending automatic machine for more than 200 times as shown the inset of Figure 2.12d, and there was no significant change in the device behavior of memristors. These results suggest the proposed device is robust

against mechanical stress as well as against ON/OFF cycles and it can be used in bendable electronic circuits down to 8 mm maximum.

2.5.2.4 Mechanism of switching

Oxygen vacancies in oxide materials are reported in the literature, they act as n-type dopants [28]. By controlling the oxygen vacancies at top electrode metal/oxide interface of the oxide layer, local filaments formation can be achieved. These local filaments results in tunneling effect at the metal/oxide interface and make a current flow through the oxide layer. This phenomenon can be understand as, when a negative voltage is applied on the top electrode, in the result it attracts positively charged oxygen vacancies in the oxide layer toward the top electrode. The vacancy dopants drift in the electric field and makes local filament with a high electrical conductivity. Because of the local filaments at the top electrode interface, the energy barrier is lowered and the resistance is reduced that is LRS state of the memristor. Once the device is switched in LRS state, it will remain in this state until the local filaments are not broken by applying opposite voltage at the top electrode. To switch the device back to HRS state, a voltage with reverse polarity at the top electrode is applied that is higher than the threshold, in the result the oxygen vacancies are repelled from the top interface and the original electronic barrier is recovered [29]. This state of memristor is HRS, hence the resistance of the device is modulated by external bias between HRS and LRS. The bipolar resistive switching in the ITO/$ZnSnO_3$/Ag devices is due to the formation and rupture of conducting filaments in the interface of Ag/active-layer at the top electrode only, not throughout the $ZnSnO_3$ bulk film. Because the I-V curve as shown in Figure 2.11 is not switching abruptly from HRS to LRS and vice versa but the transition is ohmic.

2.5.3 Summary

In the work, zinc stannate ($ZnSnO_3$) material for the sandwich layer of a memristor for the first time. 9 memristor devices were fabricated on a flexible single substrate PET through EHD technique. The array was consisted of ITO bottom electrode, Ag top electrode and $ZnSnO_3$ sandwiched active layer. The physical dimension of the single device was 2mm×100μm with active layer thickness of 130 nm. The device gave resistive switching behavior with R_{OFF}/R_{ON} = 300. Individual devices of the array were switched between HRS and LRS for writing the data in the form of memristor state at ±8 V, whereas reading voltage of 5V was selected experimentally.

Variability from device to device was characterized for the 9 devices and very small change was observed in the resistance values of HRS and LRS. The device exhibited endurance cycles for more than 200 cycles, retention time for 200 min, and bendability down to 8 mm. The surface morphology analysis was carried out with the help of microscope and SEM. The results of the proposed resistive switches suggest that these switches can be good candidates for non-volatile resistive memory applications

2.6 References

[1] L. O. Chua, IEEE Transactions on Circuit Theory 18 (1971) 507-519.
[2] Dmitri B. Strukov, et al., Nature, 453(7191):80{83, May 2008.
[3] L.O Chua, Applied Physics A, 102, 765-783, 2011.
[4] Jeremy T. Robinson, et al., Nano Lett. 10 (8) (2010) 3001-3005.
[5] Hu Young Jeong, et al., Nano Lett. 10 (11) (2010) 4381-4386.
[6] K. S. Novoselov, et al., Nature 490 (2012) 192-200.
[7] K. Geim, et al., Nature Materials 6 (2007) 183-191.
[8] Zurutuza, et al., Nature Nanotechnology 9 (2014) 730–734.
[9] Kinam Kim, et al., Nature 479 (2011) 338–344.
[10] Tae-Wook Kim, et al., Organic Electronics 15 (11) (2014) 2775-2782.
[11] Qiaoliang Bao, et al., ACS Nano 6 (5) (2012) 3677-3694.
[12] Jaeheung Ha, et al., Organic Electronics 14 (9), 2013, 2324-2330.
[13] Alexander A. Balandin, et al., Nano Lett. 8 (3) (2008) 902-907.
[14] E. Pollak, et al., Nano Lett. 10 (9) (2010) 3386-3388.
[15] Liang-shi Li, et al., J. Phys. Chem. Lett. (2010) 1 (17) 2572-2576.
[16] Mitchell Bacon, et al., P. & Particle Systems Characterization 31 (2014) 415-428.
[17] Rainer Waser, et al., Nature Materials 6 (2007) 833-840.
[18] M. N. Awais, et al., Electronic Materials Letters 10 (3) (2014) 601-606.
[19] J.J. Yang, et al., Nanotechnology 20 (2009) 215201-215210.
[20] N.G. Hackett, et al., IEEE Electron Device Lett. 30 (7) (2009) 706-708.
[21] D. Zhu, et al., Nano technology (2005) 296-299.
[22] Y. Vijayakumr, et al., International Conference on Advanced Nanomaterials and Emerging Engineering Technologies (ICANMEET), (2013), pp. 502-505.
[23] J. C. Yang, et al., Micro & Nano Letters, IET. 7 (2012) 244–247.
[24] E. Ngo, et al., Electron Devices, IEEE Transactions on. 60 (2013) 2372–2378.
[25] R. P. A. Hartman, TU Delft, Hagen, Germany, 1998.
[26] Hayati, et al., Nature 319 (1986) 41–43.
[27] S. Ali, et al., Applied physics A 119 (2015) 1499-1506.
[28] P. Knauth, et al., Journal of Applied Physics 85 (1999) 897–902.
[29] J. J. Yang, et al., Nature Nanotechnology 3 (2008) 429–433.

Chapter 3 Memristive Circuits

3.1 Introduction

Memristor is two terminals passive circuit element except it can change its resistance between two states HRS & LRS and retain the state in absence of power. This very feature makes the memristor an attractive circuit element especially where memory is concern. Apart from crossbar non-volatile memories, it can be used in discrete electronic circuits such as RC filters, parallel and series resistive circuits and in logic circuits. Some applications of the memristor in electronic circuits are described below.

3.2 Single bit voltage divider memory

Recently printed electronics has been widely researched in electronic industry and research groups due to its various advantages over conventional rigid electronic technology. Low cost, flexibility, rapid and easy fabrication process, and printing capability are the key features of printed electronics [1]-[5]. Many researchers are studying organic electronics including organic light emitting diodes (OLEDs), organic thin film transistors (OTFTs), organic solar cells, memristors, capacitors, and organic sensors [6–13]. In addition, organic electronics have opened a door for organic memories in the information technology such as Resistive Random Access Memorys (ReRAMs) based on memristive switching devices [6]-[8]. Integrated and high-density circuits based on organic electronics, however, are not matured at present time because of their fundamental issues in the circuit topology. In case of the crossbar structure of memristive memory array, crosstalk and sneak current problem are commonly occurred, which may result in unwanted switching [9]-[11]. Many researchers are also working on resistive memories in different combinations of memristors with transistors, diodes, and selector devices [12]-[14]. Every combination has its specific limitations toward the large-scale integration. In this work, we propose a novel non-volatile memory cell manufactured by the EHD, which is consisted of one organic resistor and one memristor connected in series. The proposed organic non-volatile memory cell is designed by adoption a voltage divider operation. The organic resistor for the device is fabricated for its resistance of 6.2 k by using the materials, poly(3,4-ethylenedioxythio-phene):poly (styrenesulfonate) (PEDOT:PSS). The memristor is made of Zirconium dioxide (ZrO_2) material and its resistance state is switched between high resistance state (HRS) of 4.3 kΩ and low resistance state (LRS) of 300 Ω

.Conceptually, the proposed organic device stores a logic‘‘0’’ or ‘‘1’’ as the resistance states of the memristor, and read by voltage division rule (VDR) according to the memorized resistance state of the memristor. The memorized bit data can also stably read and write against bending of the device.

3.2.1 Fabrication

The proposed non-volatile organic memory cell was fabricated through electro-hydrodynamic (EHD) technique. Stable cone jet and uniform spray deposition on substrate is required to fabricate a device, which is controlled by the ink flow rate and operating voltage. Ink flow rate and stage movement velocity are used to control the thickness of the deposited film. Different modes of spray are obtained during spray by adjusting ink flow rate and operating voltage including dripping mode, unstable mode, stable con jet mode and multi con jet mode. Summarized values of different flow rates and operating voltages for both memristor and resistor fabrication for the proposed device are shown in Figure 3.1 a and b. By utilizing poly(3,4-ethylenedioxythiophene):poly(styrenesulfonate) (PEDOT:PSS) material, the organic resistor was fabricated for the proposed memory cell. A patterned ITO coated Polyethylene terephthalate (PET) was used as substrate, and cleaned sequentially with ethanol, acetone, and deionized water for 10 min each. The sample was then kept in open air to dry, afterward UV treatment of the sample was carried out for 5 min. The ink for organic resistive layer was prepared by diluting (2 %wt) PEDOT:PSS with 5 ml of isopropanol and stirred for 30 min at 2000 rpm.

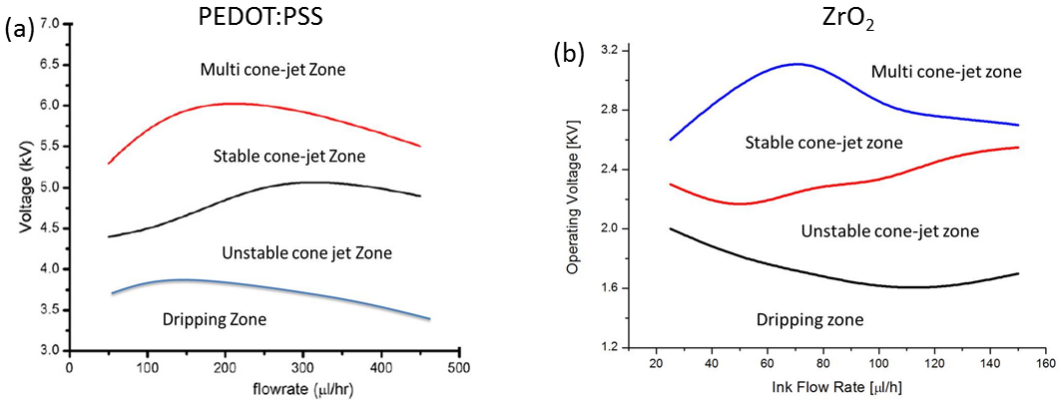

Figure 3.1. Ink flow rate and applied voltage curves during EHD deposition, (a) PEDOT:PSS (b) ZrO_2

Then 2 ml of deionized water was added and stirs for 2 h under a room temperature and open air. To increase the resistance of PEDOT:PSS ink, poly(methyl methacrylate) (PMMA) was added. The ink was prepared as: 16 mg/ml of poly(methyl methacrylate) was mixed in isopropanol and stirred

on a magnetic stirrer for 1 h. Both inks were prepared separately and then PMMA was added with 1:6 to the PEDOT:PSS to achieve the required resistivity. The resistor was made as length of 1 mm, width of 0.6 mm, and thickness of 1 l m, and the resistor was 6.2 k X . The memristor active layer ink was prepared as: 5 weight ratio ZrO_2 produced by Sigma Aldrich. Dispersion was mixed in ethanol with 1:1 volume ratio. Thereafter, the nanoparticle solution was sonicated for 30 min.

For the fabrication of the proposed single bit memory device, an ITO coated patterned PET substrate was used. Resistor was fabricated on simple PET whereas memristor was fabricated on

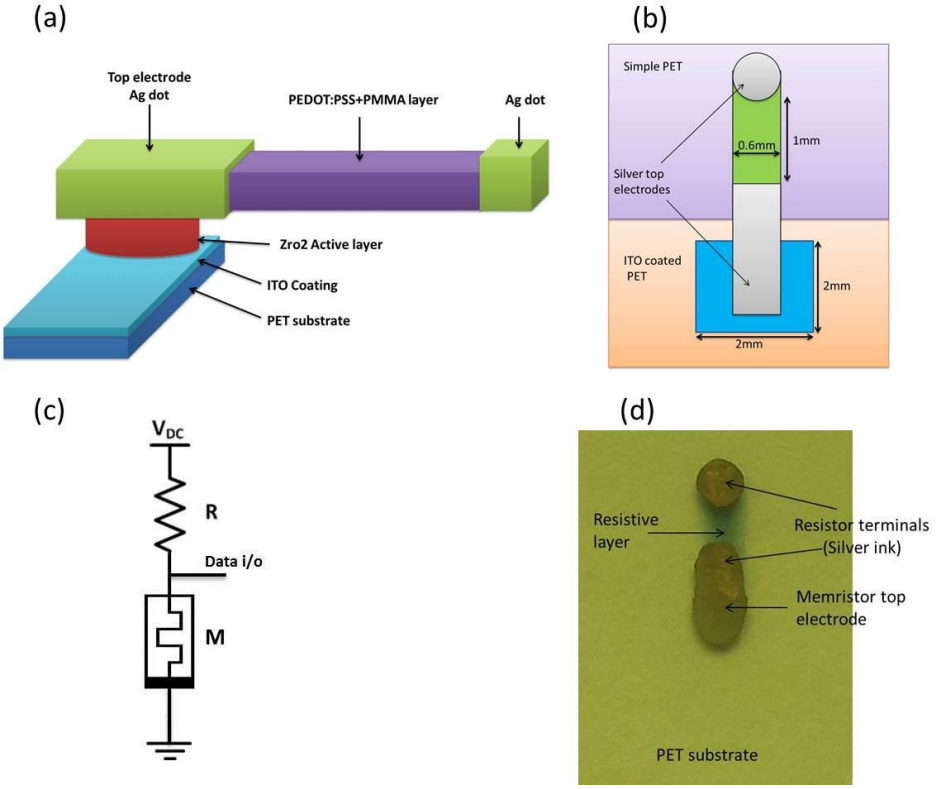

Figure 3.2. (a) Material diagram of the non-volatile memory cell. (b) Dimensions and top view of the memory cell on ITO coated patterned PET substrate, where memristor is fabricated on ITO coated PET and resistor is fabricated on simple PET. (c) Equivalent circuit diagram of the non-volatile memory cell. (d) Photograph of the non-volatile memory cell fabricated by the EHD system.

ITO coated portion of the PET. The prepared solution for the memristor fabrication was placed in the ink chamber and pumped to metallic nozzle at 5.2 KV. The substrate movement velocity was 2.4 mm/s and the ink flow rate was 55 ul/h with the nozzle to substrate distance of 1.5 mm. The organic resistor based on PEDOT:PSS on the simple PET substrate was fabricated as, the prepared solution of PEDOT:PSS was placed in a chamber and pumped at 200 ul/h to the metallic nozzle (inner diameter of 110 nm) with operating voltage of 5.3 KV and stage movement velocity of 3 mm/s. After the fabrication of both devices on the same substrate, the sample was kept for curing

at 130 °C for 1 h. Afterward Ag drops were placed on both ends of the PEDOT:PSS based resistor 1 mm apart, and on the ZrO_2 layer to complete the metal insulator metal (MIM) structure of memristor. Figure 3.2a and b shows the structure of the materials and the physical dimensions of the device on top view, respectively. An equivalent circuit diagram for the proposed non-volatile memory cell is presented in Figure 3.2c, where V R is a constant DC operating voltage for the proposed memory cell, and $V_{I/O}$ is a bidirectional port for reading and writing data. The fabricated memory device is shown in Figure 3.2d.

3.2.2 Characterization

3.2.2.1 Electrical characterization

The memory cell was placed in probe station for the current–voltage (I–V) analysis. Probes were connected to both terminals of the resistor, and the voltage sweeping from 0 V to 10 V were applied with current compliance of 100 mA. The measured resistance of the resistor is 6.2 k X which shows an ideal resistor characteristics with a linear relationship between current and voltage as shown in Figure 3.3a. The voltage sweep was repeated for 100 times to test the reliability of the resistor. As shown in Figure 3.3c, the measured resistance of the resistor for the 100 sweep cycles is bounded in between 6200 X and 6270 X . By these results, it can be said that the manufactured organic resistor is beneficially operated with a stable resistance characteristics for a general electronic circuit applications. The memristor was also analyzed individually for its I–V characteristics utilizing the measured data by the same Agilent B1500A Semiconductor Device Analyzer. With probes connected across the memristor, voltage sweeping from -3 V to +3 V was initially applied with current compliance (CC) of 10 mA, and then the sweeping voltages were increased up to ±5 V with current compliance of 1mA to find a maximum bearable voltage. The memristor shows a stable behavior without any state change in a voltage range between -1 V and +1 V as shown in Figure 3.3b. HRS/LRS switching of a memristance is occurred outside this range. To make sure the reliability of both states, the device was tested for more than 100 times ON/OFF switching. The ohmic values of both states were slightly increased with the number of switching cycles, but these are clearly discriminated on between HRS and LRS as the cumulative probability graph of the memristive states shown in Figure 3.3d.

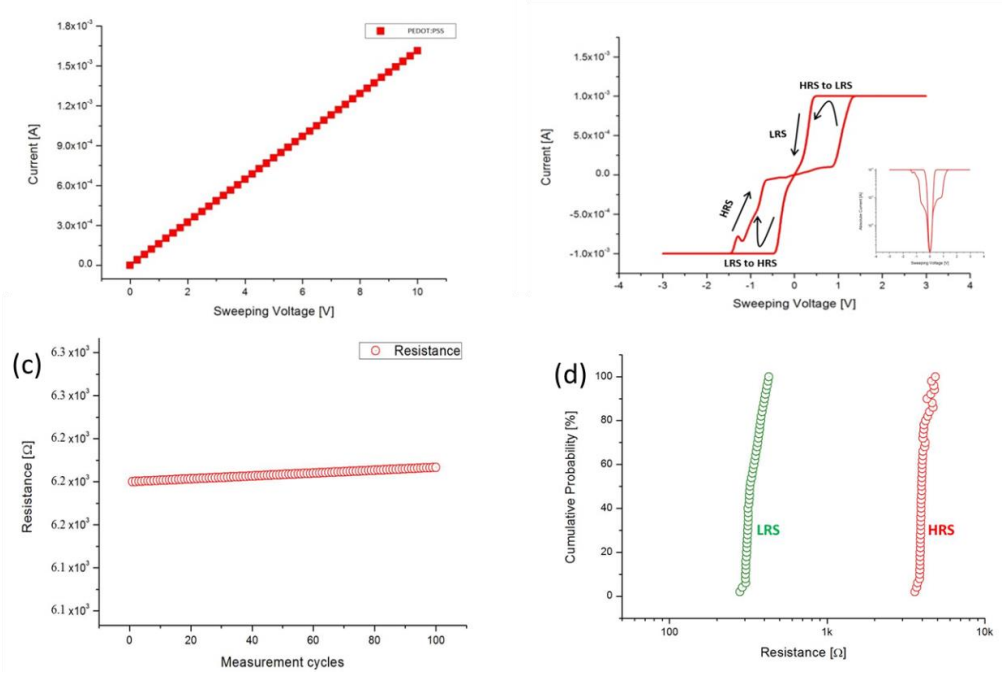

Figure 3.3. Electronic characteristics of the non-volatile memory cell; (a) voltage-current graph of organic printed resistor, (b) I–V curve of the memristor with current compliance of 1 mA (It shows resistive switching and absolute current graph.), (c) resistance endurance test for 100 measuring cycles (Resistance slightly increased with number of measurements.), and (d) Cumulative probability for a state resistance stability test of the memristor (Random variables are resistance of memristor states HRS and LRS).

The operation of the proposed memory cell is defined accordingly with the performance of both the resistor and the memristor as shown in Figure 3.4a. The proposed memory cell is described for data writing and reading cycles. In data writing mode, the V_R sets 0V to prevent excessive current flow through organic resistor. Then, ±4 V are applied on the port $V_{I/O}$ to write the logic value ‘‘1’’ or ‘‘0’’. The memristor is switched from HRS to LRS when +4 V is applied to the $V_{I/O}$, and it is reversely switched from LRS to HRS by applying -4 V as shown in Table 3.1.

Table 3.1. Data writing cycle of non-volatile memory cell, memristance states and their values.

Switching voltage	Memristance State	Memristance Value
-4 V	HRS	4.3KΩ
+4 V	LRS	300Ω

In data reading mode, if a constant voltage is supplied on the V_R , the logic value is detected on the $V_{I/O}$ depending on the state of the memristor. V_R = 2V for the data-reading mode and the logic ‘‘1’’

and ‘‘0’’ are theoretically read as the voltage level of 0.82 V and 0.091 V at the port $V_{I/O}$, respectively, by voltage division rule are given in equation 1 and 2. The reading cycle voltage along the state of resistance are given in Table 3.2.

Table 3.2. Data reading cycle of non-volatile memory cell, memristance states and their respective output voltages.

Operating voltage	Memristance State	Output voltage, V_o
+2	HRS	0.82 V
+2	LRS	0.091V

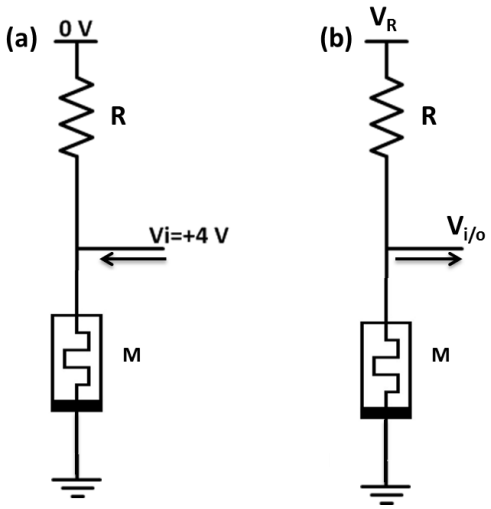

Figure 3.4. (a) Data writing circuit, (b) Data reading circuit.

$$V_{Low} = \frac{R_{LRS} * V_{DC}}{R_{LRS} + R} \qquad (1)$$

$$V_{High} = \frac{R_{HRS} * V_{DC}}{R_{HRS} + R} \qquad (2)$$

Here, V_{LRS} and V_{HRS} are output voltage at $V_{i/o}$ port for the states LRS and HRS, respectively, R_{LRS} and R_{HRS} are resistances of the memristor (M) on the states of LRS and HRS, respectively, and R is resistance of the resistor. Using above equations, the real voltages for the stored logic value ‘‘1’’ and ‘‘0’’ are defined, respectively. With these selected voltages, Vi/o for writing mode and V_R for reading mode, the memory cell demonstrates stable behaviors with good performance.

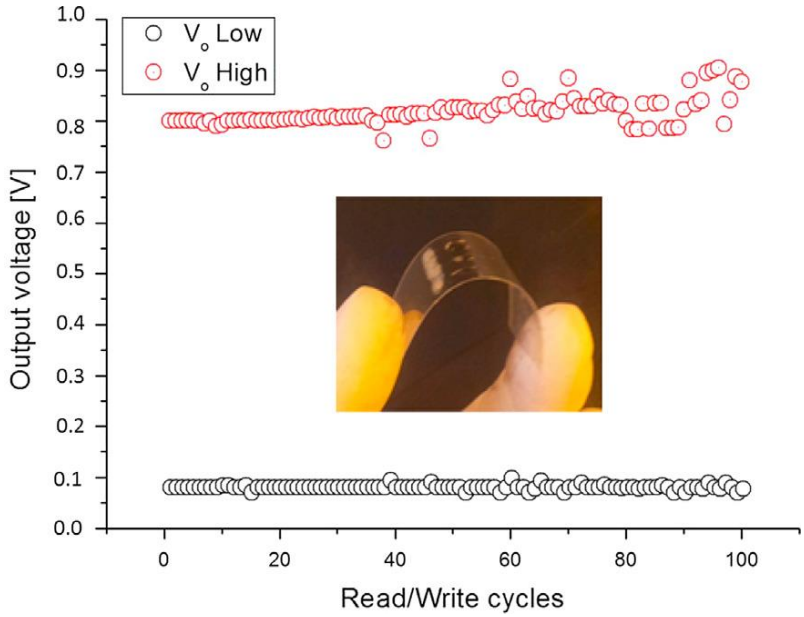

Figure 3.5. Data reading and writing performance in terms of output voltage at $V_{i/o}$ port for 100 endurance cycles.

The data reading and writing performance were tested for 100 cycles, and the stability of the memory cell in term of low and high voltage gathered at Vi/o was verified as shown in Figure 3.5. There were slight change in the voltage levels after 60 cycles but not overlapped until 100 cycles. Large enough detection margin between low level and high-level output voltages was maintained. To verify the reproducibility of this characterization, we fabricated 10 memory cells, and found the detection margin as example shown in Figure 3.5. The obtained detection margin was between 0.3 V and 0.6 V, and its detection error was zero. From these results, a bit data between logic ‘‘1’’ and logic ‘‘0’’ can be exactly detected.

The retention time analysis for the data holding was carried out for 100 min. There was no significant change in the output voltage levels along the time stress. This test was applied on two data types; one holding low voltage for logic ‘‘0’’ and the other holding high voltage for logic ‘‘1’’. The voltage levels in both states slightly increases along time as shown in Figure 3.6a, but large enough detection margin to detect an exact data still have been maintained. The power consumptions of the proposed device to write the logic value ‘‘1’’ and ‘‘0’’ are 1 mW and 1.25 mW, respectively. For read mode, the power consumptions for the logic value ‘‘1’’ and ‘‘0’’ are 380 µW and 614 µW, respectively. To find the bending limitation of the operation of the device, the memristor’s LRS and HRS were characterized for various bending diameters. The device was bent on the rod starting from 30 mm to 12 mm in diameter, and we measured the resistance of the

both memristive states HRS and LRS as shown in Figure 3.6b. Slight changes in resistance of both states were observed as the bending diameter decreases from 30 mm to 12 mm. However, sharply bent device beyond the 12 mm became an open circuit due to the breakage of silver electrodes. Data read/write speed is dependent on the transition time of the memristor from HRS to LRS, and the transition time also depends on its material. The proposed device can operates at 20 K read/write cycles per second. From the experimental results, we conclude that the proposed device is applicable for larger bending diameter than 12 mm.

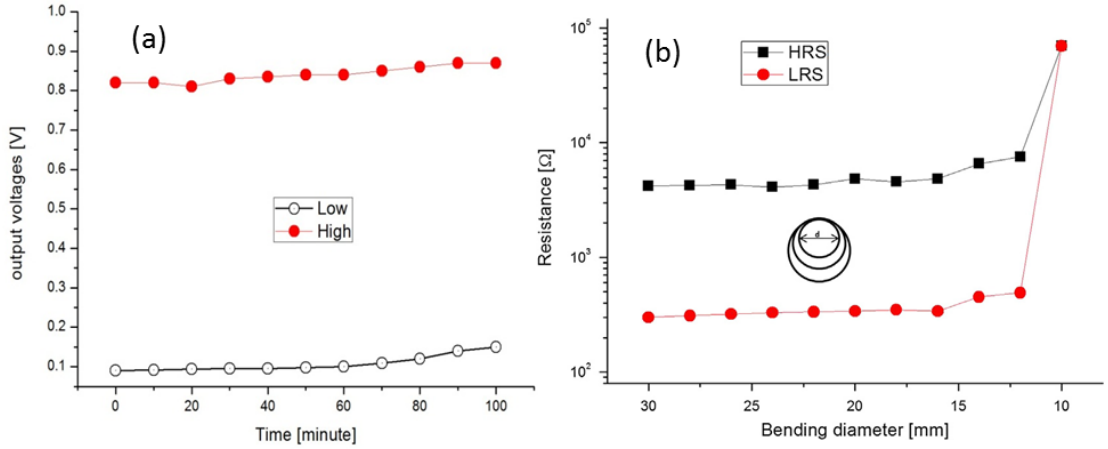

Figure 3.6. (a) Retention test of output state memorized in the non-volatile memory cell tested. (b) Resistance measured for the bendability of the device bent by using various diameter rods from 30 mm to 12 mm.

3.2.2.2 Surface morphology

The surface morphology of both active layers of the components resistor and memristor fabricated by the EHD were analyzed with a scanning electron microscope (SEM), Jeol JSM-7600F. The average grain size of 40 nm was observed in ZrO 2 , PEDOT:PSS SEM image as shown in Figure 3. 7a, and the ZrO 2 film shown in Figure 3. 7b. The thickness of the ZrO 2 film was measured with the thin film thickness measurement system (K-MAC ST4000-DLX), which was observed 76 nm. This was the optimum film thickness among samples with different thickness also the thickness of the PEDOT:PSS film was measured 600 nm. The thickness of the film was controlled during spray process by controlling the ink flow rate and stage moving velocity. These results show the proposed device is consistently fabricated by the EHD.

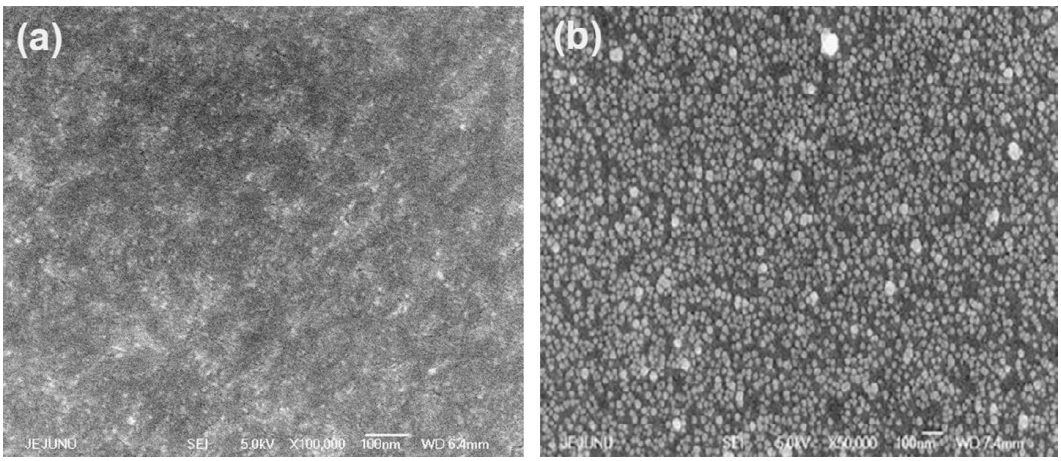

Figure 3. 7. poly(3,4-ethylenedioxythiophene):poly(styrenesulfonate) (PEDOT:PSS) Scanning Electron Microscope (SEM) images for active layer (a) of the resistor based on poly(3,4-ethylenedioxythiophene):poly(styrenesulfonate) (PEDOT:PSS) and (b) of the memristor based on ZrO_2.

3.2.3 Summary

The non-volatile memory cell capable of storing 1-bit data has been designed and fabricated on a patterned ITO coated PET substrate by utilizing the EHD technique. The memory cell was consisted of two devices, the organic resistor based on PEDOT:PSS with ohmic value 6.2 k Ω and the memristor based on zirconium dioxide (ZrO_2) with 4.3 k Ω for HRS and 300 Ω for LRS. These two devices were fabricated on a single patterned ITO coated PET substrate, and the memory cell was formed in a circuit of two components connected in series. The voltage $V_{R=}$ 2 V for reading mode was chosen to read a stored data from the memory cell. To write a bit data, the voltages (±4 V) at Vi/o was applied across the memristor through data line, which was a stable value for the operation of the memory cell. The average values of the memristor in HRS and LRS were 4.3 kΩ and 300 Ω , respectively. The device stability for data read/write cycles and retention performance were tested for more than 100 cycles and 100 min, respectively. The flexibility test was carried out to ensure the minimum applicable bending diameter that was obtained as 12 mm. The film surface morphology of active layers was also presented by taking SEM images to verify the consistency of the EHD.

3.3 Memristor based filters

In modern electronic circuits, the essential demands of a circuit are small size, low power, intelligent. Among the analog circuits, analog filters are the basic building blocks of wireless

electronic system. To overcome the circuit constraints of size, power and programmability, memristor is the best candidate for resistor capacitor RC filters. Memristor is a charge-controlled device that can switch between two resistive levels called high resistance state HRS and low resistance state LRS in analog way and it can memorize the last used state. Once it is switched in either state, it behaves like a linear resistor under its threshold voltage levels. This vey feature makes the memristor analog switch and memory device, which is the replacement of a transistor. Memristor behavior was investigated mathematically in 1971 by leon o chua [15], in 2008, the HP labs fabricate the first memristor and they physically demonstrate the properties of this special circuit component [16]. The resistive switching mechanism of a memristor is based on thermal, electrical or ion-migration-induced switching [17]. Due to the simple structure and small size, memristor is being researched in many applications including resistive memory ReRAM, neuromorphic, logic circuits and analog circuits [18]-[21]. Memristor has also investigated for analog circuit application by many researchers including filters, oscillators, and chaotic circuit [22]-[23]. To fulfill the demands of smart circuits, the analog filter should have a small size, dissipate a low power, and be easily programmable. The memristor has a small nano meter size, nonvolatile memory, and works at extreme low current. Furthermore, the memristor switching time is in sub Nanosecond range, all these advantages of a memristor make it potential candidate for the programmable analog filter applications.

3.3.1 Design of filters

Memristor capacitor (MC) filters for the low pass, high pass and band pass are design in the first order. The low pass filter schematic and layout diagram is shown in Figure 3.8a, input signal is provided to memristor and output is taken across the capacitor, as memristor can switch between its high resistance state (HRS) and low resistance state (LRS) and capacitor is of fixed value. When the memristor is in LRS state it makes a combination with capacitor and provide a cut-off frequency based on the current state resistance and capacitance. As the memristor is switched to its HRS state while the capacitor is the same, the cut-off frequency change to the other value as the RC combination is changed. In the same way, high pass filter is designed based on memristor capacitor MC components, where the input is provided to capacitor and output is taken across the memristor.

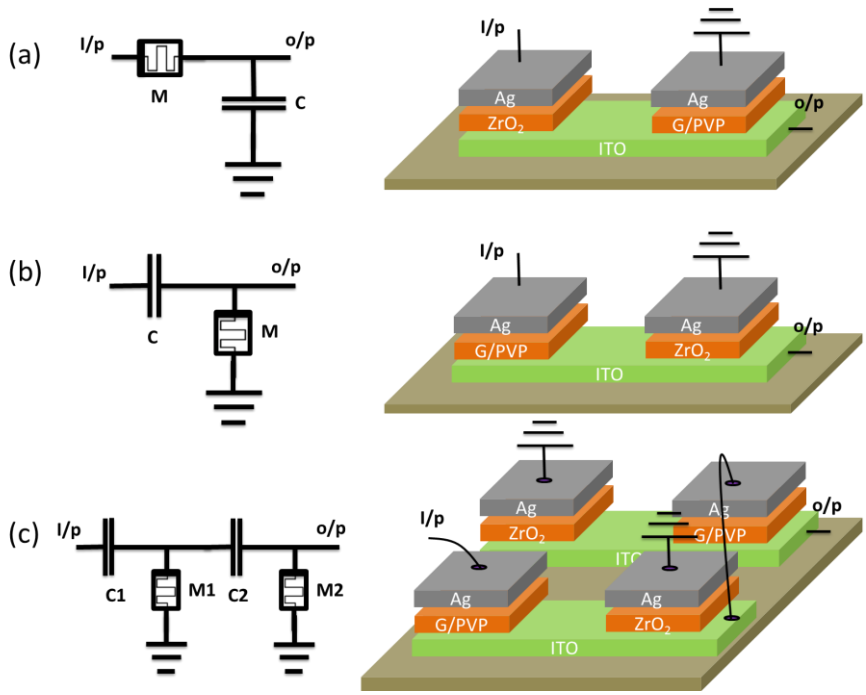

Figure 3.8. Filters with their schematic diagrams and layout diagrams (a) MC low pass filter (b) MC high pass filter (c) MC band pass filter.

In this configuration, the memristor is switched between its HRS and LRS, which results in different cut-off frequencies. The schematic and layout of the MC high pass filter is shown in Figure 3.8b. Combining two filters in cascade, a band pass filter is formed, where M1 and C1 are making high pass MC filter and M2C2 making low pass MC filter. The cut-off frequencies of the filter can be tuned by switching the memristors M1 and M2 in their either LRS or HRS resistive states, where as C1 is not equal to C2 but memristors are the same. The schematic diagram is shown in Figure 3.8c.

3.3.2 MC Filters Simulation

In our simulation, three types of MC filters, low pass MC filter, high pass MC filter and band pass MC filter are simulated in Matlab 2015. The cut-off frequency is controlled through the resistive state of the memristor (HRS or LRS). In our simulation, we have implemented the transfer function of low pass filter equation as given below

$$\frac{V_{out(s)}}{V_{in}} = \frac{\frac{1}{CR}}{s + \frac{1}{CR}} \qquad (1)$$

The cutoff frequency of the filter is given by the following equation

$$f_c = \frac{1}{2\pi RC} \qquad (2)$$

Where R shows the resistance and C used for capacitance. In simulation, memristor is used which can switch its state from HRS to LRS and vice versa. In simulation we have selected the average values of HRS and LRS states are 4KΩ and 300Ω respectively. As the memristor can switch between the HRS and LRS states, this effects the change in cutoff frequency of the low pass filter according to equation 2. The cutoff frequency is low when the memristor in HRS state (its average resistance is 4KΩ) and high for LRS state (when its resistance is 300Ω) of the memristor. We can change or tune the cutoff frequency of the low pass filter accordingly. The magnitude and phase response of the low pass filter is shown in Figure 3.9a. It can be observed from the figure that the cutoff frequency is changed from low to high when the memristor switched from HRS to LRS states.

Equation 3 shows the transfer function of the high pass filter. The transfer function is simulated with same HRS and LRS states values as used in low pass filter design. The capacitor of 1µF is used for high pass and low pass filter design. The response of this equation is shown in Figure 3.9b.

$$\frac{V_{out(s)}}{V_{in}} = \frac{s}{s + \frac{1}{CR}} \qquad (3)$$

The transfer function of band pass filter design is given in equation 4. In band pass filter design both high pass filter (HPF) and low pass filter (LPF) used as a cascaded model. The memristors used in HPF and in LPF can switch to either LRS or in HRS at the same time but not alternatively. The values for HRS and LRS is same as in case of LPF and HPF design, similarly capacitance of 1µF is used. The magnitude and phase plot of the HPF design is shown in figure 3. It can be observed from Figure 3.9c and d that the frequency band changed with the transition of memristors from HRS to LRS or vice versa.

$$\frac{V_{out(s)}}{V_{in}} = \frac{s\frac{1}{C_2R_2}}{s^2 + s\left(\frac{1}{C_1R_1} + \frac{1}{C_1R_2} + \frac{1}{C_2R_2}\right) + \frac{1}{C_1R_1C_2R_2}} \qquad (4)$$

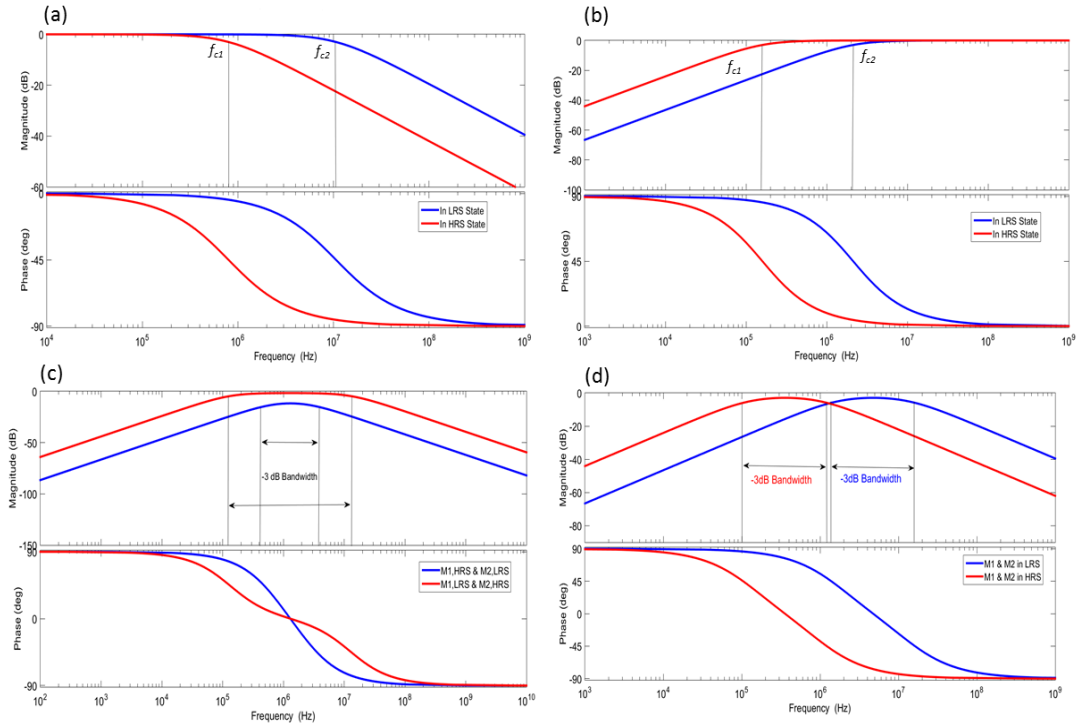

Figure 3.9. Simulation results of frequency selective MC filters (a) low pass MC filter with dual cut-off frequencies fc1 and fc2, (b) Highpass MC filter with dual cut-off fc1 and fc2, (c) MC tunable bandwidth filter, (d) MC band selective filter

3.3.3 Fabrication

Graphene platelets (<4 layers and surface area >750 m^2/g), 5% weight ratio ZrO_2 dispersion, N-methyl-pyrrolidone (NMP) solvent, and poly 4-vinlyphenol (PVP) from cheap tubes and Sigma-Aldrich were purchased respectively. Ink for the capacitor dielectric layer was prepared as: The graphene platelets of 0.84 mg and PVP of 0.40 g were dispersed in NMP (4 ml) solvent by bath sonication for 30 min at room temperature. The supernatant containing in PVP/graphene was collected by centrifugation at 3,000 rpm for 20 min. Memristor active layer material was utilized as 5% weight ratio ZrO_2 dispersion. Ink for the silver electrodes was prepared as: Ag nanoparticles ink was prepared by diluting the Ag Nano paste (PARU Corp.) by adding ethylene glycol as solvent in a 50 % concentration by weight. The solution was stirred for 15 min followed by bath sonication for further 15 min.

EHD system's parameters were tuned for each of the materials by adjusting applied voltage, ink flow rate and stand-off distance. Initially, flow rate and applied voltage values were kept 0 and then increased gradually to observe the stable con jet mode. In the case of graphene/PVP dielectric layer deposition, ink flow rate was 280 µl/h and voltage was varied from 0 kV to 6.5 kV. Same procedure was followed for the ZrO_2 (memristor active layer) and silver (electrodes). Details about the EHD fabrication technique can be found in chapter 1. Prior to begin with EHD fabrication for the devices capacitor and memristor, the substrate was rinsed with ethanol and then deionized water for 5 minutes each, and then dried. After confirmation of the EHD stable cone jet, substrate was place and masked for the fabrication of capacitor dielectric layer. Then mask of capacitor was removed and cured the sample at 100 °C for 1h. Mask for the memristor was placed on the substrate to deposit active layer of the memristor by ZrO_2 Material. The purpose of the substrate masking is that, to avoid unwanted material deposition on the substrate. The sample was again cured at 130 °C for 1h. To deposit the top electrodes of the devices, mask according to the plate area of the capacitor was placed on the capacitor dielectric layer and silver material was deposited to make the capacitor plate. The memristor's top electrode was deposited by masking and then depositing the silver material through EHD. Again, the device was cured at 100 °C for 30 min.

3.3.4 Electrical characterization

Figure 3.10a, shows I-V characterization of the memristor against voltage sweep of ± 5V where memristor switches from HRS to LRS at 4V and go back to -4V. The absolute I-V curve is shown in the inset that confirms the bipolar resistive switching of the device that pinches at 0V. Figure 3.10b shows endurance cycle test of the memristor for 100 cycles to confirm the stability of the device against multiple cycles. Figure 3.10c depicts the capacitor characterization against frequency sweep, two capacitors of 100 pF and 50 pF are characterized against frequency sweep. Figure 3.10 shows capacitance analysis of the capacitors against sweeping voltage. This analysis confirms the capacitor stability against changing voltages.

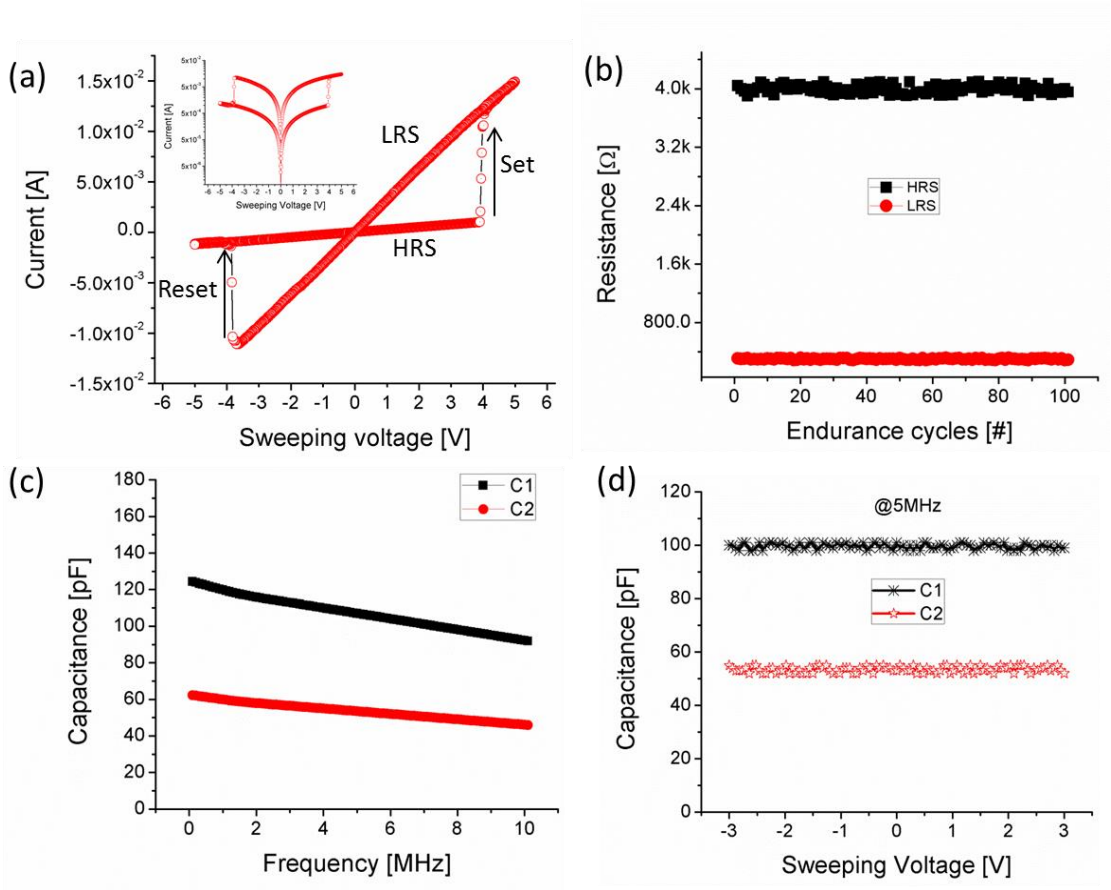

Figure 3.10. (a) voltage current (I-V) analysis of the memristor, (b) Endurance analysis of the memristor for 100 cycles, (c) capacitance vs frequency analysis of the capacitors, (d) capacitance vs voltage analysis of the capacitors.

3.3.5 Summary

In summary, we have demonstrated MC filters including low pass, high pass, and band pass fabricated on flexible PET substrate through EHD technique. The cut-off frequency 9of the filters are controlled through resistive state resistance of the memristor (HRS/LRS), as the resistance value changes the cut-off frequency also shifts. The simulated results are compared with measured results and almost same behavior is achieved. Change in the frequency behavior of the filters due to the ON/OFF cycles of memristor is addressed, which slightly changes the cut-off frequency.

3.4 References

[1] C.D. Müller, et al., Nature 421(2003) 829–833.
[2] G. Darlinski, et al., J. Appl. Phys. 97 (2005) 093708.
[3] T.W. Lee, et al., Adv. Mater. 17 (2005) 2180–2184.
[4] J.Y. Kim, et al., Science 317 (2007) 222–225.
[5] S.I. Na, et al., Adv. Mater. 20 (2008) 4061–4067.
[6] C.H. Cheng, et al., IEDM Tech Dig, 2010, pp. 512–515.
[7] S. Kim, et al., Nano Lett. 11 (12) (2011) 5438–5442.
[8] H. Wang, et al., Microelectron. Eng. 91 (2012) 144–146.
[9] K. Kinoshita, et al., Appl. Phys. Lett. 93 (2008) 033506.
[10] M.J. Lee, et al., Adv. Mater. 19 (22) (2007) 3919–3923.
[11] B.S. Kang, et al., Adv. Mater. 20 (16) (2008) 3066–3069.
[12] B. Cho, et al., Adv. Mater. 22 (11) (2010) 1228–1232.
[13] S. Kim, et al., Nano Lett. 11 (12) (2011) 5438–5442.
[14] C.H. Wang, et al., IEEE Trans. Electron Dev. 58 (8) (2011) 2466–2472.
[15] L.O. Chua, et al., IEEE Trans. Circuits Theory 18 (1971) 507–519.
[16] D.B. Strukov, et al., Nature 453 (2008) 80–83.
[17] R. Waser, et al., Nature Materials 6, 833 - 840 (2007).
[18] Sung Hyun Jo, et al., *Nano Letters* **2010** *10* (4), 1297-1301, DOI: 10.1021/nl904092h.
[19] Alexandros Emboras, et al., Nano Lett. 13 (12) (2013) 6151-6155.
[20] B.C. Bao, et al., Electronics Letters 46 (3) (2010) 228-230.
[21] S. Ali, et al., Organic Electronics 17 (2015) 121-128.
[22] Tian Xiao-Bo, et al., Chin. Phys. B 2013, 22 (8) 088501-088512.
[23] Bao B C, et al., Chin. Phys. B 19 030510
[24] S. Ali, et al., Appl. Phys. A DOI: 10.1007/s00339 -015-9127-y.

Chapter 4 Resistive Memory

Due to versatile properties of conducting polymers [1], various printed electronics based on polymer materials have been extensively researched because of their flexibility, eco-friendly, low cost, and easy fabrication [2]. Among the attractive applications of printed electronics, a flexible memory is essential part to realize a fully flexible system [5]. Due to the physical and economical limitations of CMOS technology [8],[9], memory researchers are actively researching new scalable nonvolatile memory technologies that can replace flash memories to achieve high density, small size, and low power[6],[7]. RRAM based on the resistive switching has extensively investigated due to its ample advantages over conventional flash memory [10]-[13], which has been considered as the next generation non-volatile memory NVM technology since it has the solution for low power consumption, high-speed response, high-density integration, high retention time, flexibility, and zero standby power [14]-[18]. To achieve high dense memory applications, crossbar array structures based on RRAM has been demonstrated [19], which have also many advantages of low power, nonvolatile nature, and ease fabrication. However, the crossbar array has several inherent problems including cell-to-cell interference called as sneak current problem and its power consumption. Especially, it requires peripheral circuits on reading cycle, which can just read a single bit at a time. The sneak paths result in extra power consumption due to leakage current of neighbor cells and the situation is further exacerbated if the resistance of the RRAM devices based on crossbar array is low [22]. The power consumption of the memory device also increases along the memory size, results in more sneak paths. The crosstalk problem depends a voltage margin between high resistance state (HRS) and low resistance state (LRS) of a memristor due to memory cell is sensitive to read/write voltage levels. The power consumption of the memory device also increases as the memory size increases that result in more sneak paths. In general, the previous crossbar arrays can reads one bit at one clock and can reads serial data in current. Hence, these require complex peripheral circuits to read data. To overcome these problems, a memory device should have high enough OFF/ON resistance ratio, low operating current, sufficient detection margin in reading and writing a logic data, low power consumption, and simple parallel voltage readable architecture.

4.1 Resistive Crossbar Memory with Pull-up Resistors

4.1.1 Memory architecture

In this section, a new architecture of crossbar array consisted of silver crossbar electrodes with PVP sandwiched layer and a pull up resistor connected in series with each column bar is presented. The proposed RRAM utilizes only a small number of resistors by sharing one pull up resistor with multiple memristors on a column expanded from the memory cell with the voltage divider operation proposed in 3.2, as shown in the inset of Figure 3.11a. The layout diagram of a single bit memory cell based on the voltage division rule which is consisted of two components, an organic resistor and a memristor as shown in Figure 3.11a. They are connected in series and data is taken/given on common point "Data i/o" port. Reading voltage VR is applied at the upper end of the resistor and the electrical ground is provided to the memristor through the row electrode. The theoretical data timings for the read and write operations are depicted in Figure 3.11b. In write mode, ±2 V on "Data i/o" port is applied to switch memristor from HRS to LRS for logic level "0" or from LRS to HRS for logic level "1", whereas the read voltage VR port is grounded. During the read mode, with VR of 0.5 V is applied to the memory cell at the upper terminal of the resistor as shown in Fig. 3a. Voltage accordingly to the stored logic level is measured at the "Data i/o" port as V_{Low} and V_{High} for logic "0" and "1", respectively.

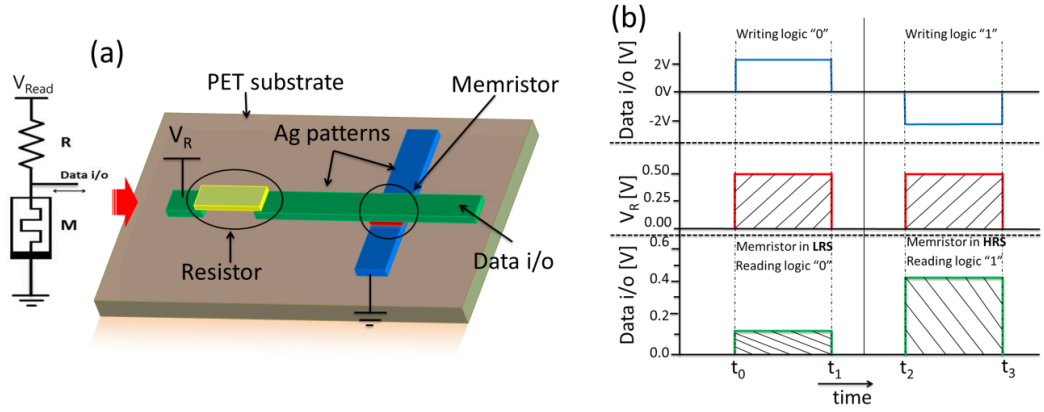

Figure 3.11. (a) Layout diagram of a single bit memory cell fabricated on PET substrate. Resistor and memristor are connected series, V_R is reading voltage, Data i/o is read/write port. The inset shows schematic equivalent circuit of the single bit memory cell. (b) Timing diagram of the single bit for read/write cycles and their voltage levels for logic 1 and logic 0. Here, read/write voltage = ±2V, reading voltage =0.5V. Output voltage is a function of memristance value.

Every single bit memory have one pull up resistor that makes the architecture difficult to fabricate, we have simplified the architecture by sharing one pull up resistor for multiple memristors connected on a row as shown in **Figure 3.12**a-c.

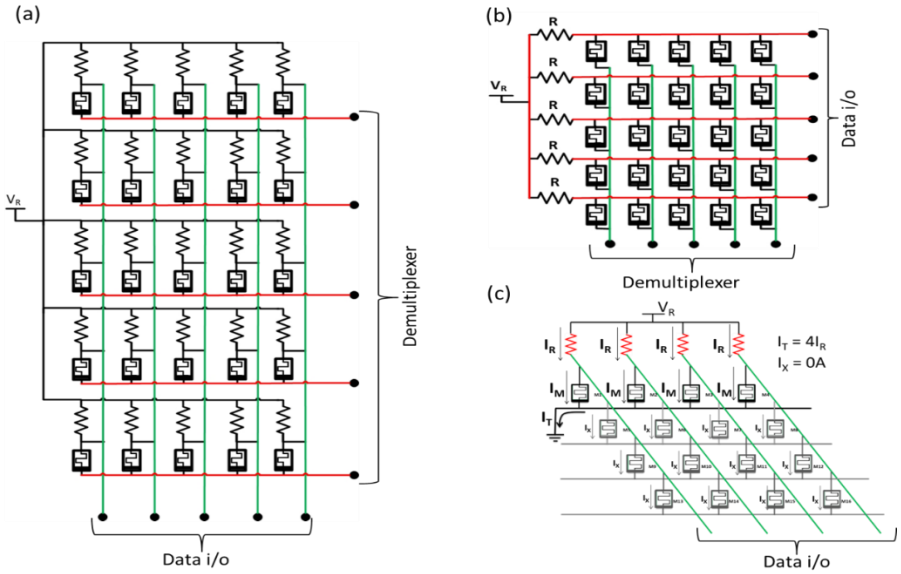

Figure 3.12. (a) 5x5 crossbar memory array based on one resistor one memristor. (b) Simplified 5x5 array sharing by one resistor for column. (c) Schematic equivalent circuit of the array.

Since it is composed of one resistor and one column memristor (1R-1CM) memory cell, it can read parallel logic values in the form of voltage instead of current. The 1R-1CM RRAM consumes extremely low power because of low operating current (10 to 100 nA/cell), where the sneak current is also proportionally lowered. The power consumption was lowered by the high resistance of a single memory cell, in our case the memristor has the high OFF/ON resistance ratio of ~1000 with the HRS and LRS resistances of 10 GΩ and 10 MΩ, respectively, while the optimally designed organic printed resistor is 10 MΩ. This ratio of memristor lead to high margin in reading the data, hence logic detection error is reduced. To verify the proposed flexible memory, a 4×4 dimensional memory array is fabricated trough the electrohydrodynamic (EHD) printing technique which is verified from the viewpoint of parallel read, power consumption, and sneak current on writing cycle.

4.1.2 Fabrication

A PVP is one of the most commonly used polymers in dielectric and memory applications in thin films [20],[21]. Active layer of the memristors were prepared as: the PVP of 0.40 g was dispersed in NMP (4 ml) solvent by bath sonication for 30 min at room temperature followed by centrifugation at 3,000 rpm for 20 min. The viscosity was measured (22.3 mPa) by viscometer VM-10A system. The surface tension of the ink was found to be 20-24 mN/m. Ink for resistors is prepared as: mixing MEH:PPV and PMMA in acetonitrile as reported in previous chapter. Ink for silver electrodes is

prepared as: Ag nano particle paste sigma Aldrich 55 %wt is diluted in 10 ml ethylene glycol solvent mixed for 1h on magnetic stirrer and then 20min bath sonication. Ag ink has a surface tension of 24 mNm, viscosity of 11.3 mPa.s, and specific gravity of 1.66 gm/ml.

The layout diagram was realized through EHD technique. The EHD system can be operated as drop on demand (DOD) and the electrostatic spray deposition (ESD) (or the EHD atomization) processes. The DOD EHD was used to fabricate fine patterns for the crossbar of the memory, whereas ESD was used to deposit active layer of the memristors. The proposed 1R-CM RRAM memory on PET substrate was fabricated as, silver electrodes (width 100µm and average thickness 300 nm) and

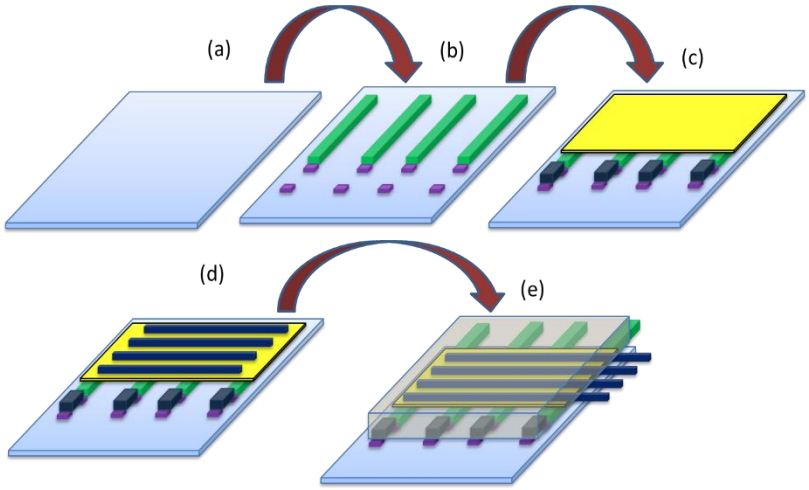

Figure 3.13. Fabrication steps of the memory array through EHD system.

resistor contacts at 2 mm distance on the PET substrate were deposited through the DOD EHD. The electrodes were cured at 120 °C for 30 min. The active layer of meristors was deposited through ESD with average thickness of 120 nm and cured for 2 h at 120 °C. Finally, top electrodes and resistive patterns were deposited through the drop on demand EHD system. Lastly, polydimethylsiloxane (PDMS) material was deployed on the device for encapsulation. Depiction of the fabrication steps are illustrated in Figure 3.13a-e. Figure 3.14a, shows a 3x3 the equivalent schematic diagram of the resistive memory array where columns are indicated to be ground and columns as data read/write bus. Top ends of the resistors are connected and reading voltage is applied. Figure 3.14b shows the layout diagram of the proposed memory device with memristors in a crossbar array structure on a flexible substrate. Silver (Ag) top and bottom electrodes (100 µm width) in the crossbar structure are deposited on PET substrate and PVP layer 120 nm thick is sandwiched between the top and bottom electrodes.

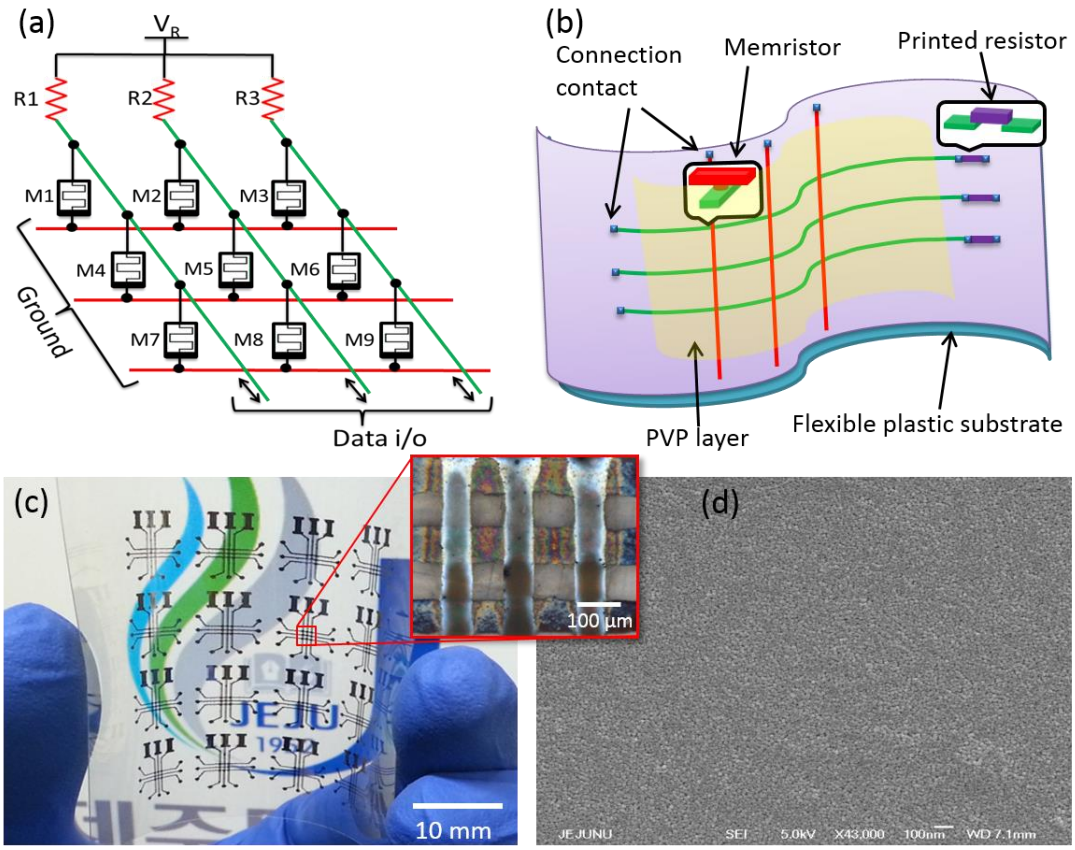

Figure 3.14. (a) Equivalent schematic circuit diagram of the proposed 3x3 crossbar memory array. Memristors are connected in rows and each row could be connected to ground one by one. Columns are connected with pull-up resistor and Data i/o bus. (b) Layout diagram of the 3×3 memory array where bottom and top electrodes silver (Ag) and active layer of memristor (PVP) is shown (c) Fabricated multiple memory arrays on a single PET substrate, fabricated through EHD system. The inset shows zoomed image of one memory array of 3x3. (d) The scanning electron microscopy (SEM) image of the PVP active layer, the inset shows cross sectional Focused Ion Beam (FIB) image of Ag/PVP/Ag structure on PET substrate, which shows that, the layers are properly deposited, and active layer is not short-circuited.

From this sequence of materials depositions, the memristor structure is metal-insulator-metal (MIM). Pull-up resistors are located at the ends of column bars on the terminal pads. Resistive material is deposited in between two silver dots (terminal pads) and the resistance is precisely controlled through the resistivity method. The proposed memory array is fully print-able with direct printing technology. Figure 3.14c shows the fabricated 3x3 memory arrays on single PET substrate, these are encapsulated with polydimethylsiloxane (PDMS) to avoid oxidization of the device from the ambient environment. Multiple arrays of 4×4 were fabricated on a single PET substrate, one of the 4×4 arrays is shown in zoomed image in the top right inset of Fig. 1c and zoomed image of the crossing point is shown in the left top inset. The average width of electrodes is 100 µm and thickness of 300 nm, and trace-to-trace clearance is 300 µm. Figure 3.14d shows FE-SEM image of the PVP film taken through Jeol JSM-7600F. Upper right inset shows Focused Ion Beam (FIB) image at a

crosspoint of electrodes, three smoothly deposited layers with thicknesses of bottom electrode, sandwiched layer and top electrode.

4.1.3 Optical and chemical characterization

Figure 3.15a shows the X-ray Photoelectron Spectroscopy (XPS) analysis graph of the PVP layer. The prominent peaks are ascribed to C (carbon) and O (oxygen) elements. The C 1s peak is present at the binding energy of 282 eV and the O 1s peak is situated at the binding energy of 530 eV. Figure 3.15b shows the transmittance spectrum of the memory device film in the ultraviolet (UV), visible, and near-infrared spectral ranges by using UV/Vis spectrometer (Shimadzu UV-3150). The transmittance is 80 to 83% in the visible range that indicates that the device can be used in transparent applications.

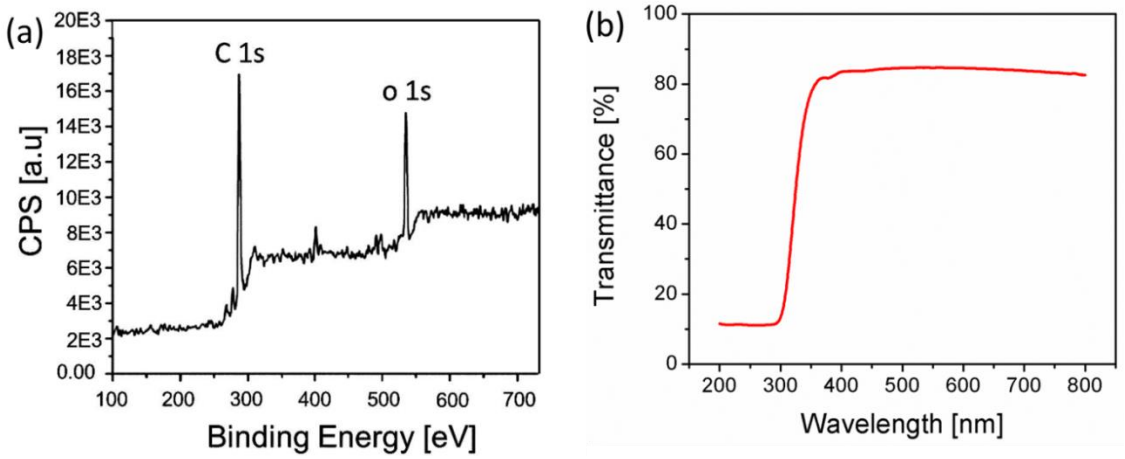

Figure 3.15. (a) Elemental composition analysis of the PVP layer through X-ray Photoelectron Spectroscopy (XPS), which shows two dominant elements, carbon and oxygen peaks situated at 288eV and 530 eV respectively. (b) UV/Vis spectrum of the device showing 83% transmittance at 500 nm.

4.1.4 Electrical characterization

Figure 3.16a shows a typical current-voltage (I-V) curve of a randomly selected memristor, an average threshold voltage of the memristor switching was observed as ±1.4 V. From the memristor I-V curve shown in Figure 3.16a and its inset, the average off/on resistance ratio of ~1000 at 0.5 V was obtained, and both resistance states (HRS and LRS) of the memristors exactly maintained their states between -1.4 V and 1.45 V. These high off/on resistance ratio will help to distinguish the stored bit states. The average resistances of the memristors for the HRS and LRS are 10 GΩ and 10

MΩ, respectively. Figure 3.16b shows the retention time performance of two randomly selected memristors. For this test, one memristor was switched in to HRS and other one was set in to LRS. When the resistance values of HRS and LRS were measured for 180 days, a negligible amount of resistance drift was observed in both HRS and LRS. This is because the fabricated device was encapsulated with PDMS right after curing to avoid the oxidation from the environment, and even after the encapsulation the device hold the promise of flexibility. The encapsulation is the essential process since the stability of the memory cell is directly dependent on the retention time.

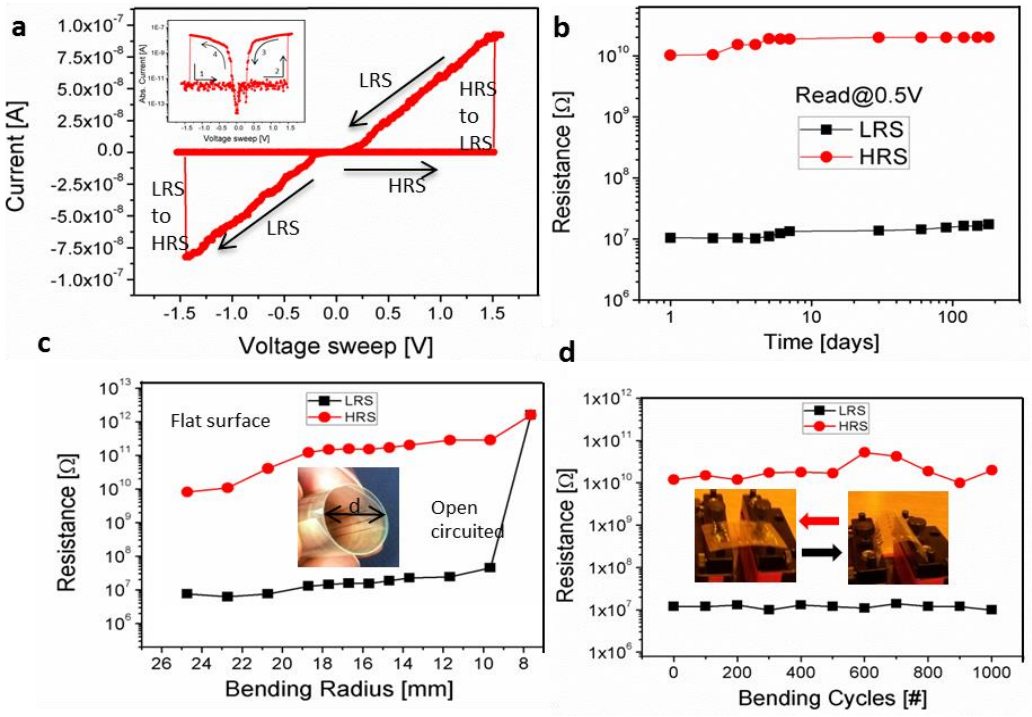

Figure 3.16. (a) Typical current-voltage (I-V) curve of the PVP based memristor, measured by voltage sweeping from -1.5V to 1.5V with 100nA current compliance (cc). Inset shows absolute current analysis of the memristor on semi-log scale. It ensures the bipolar switching of the device. (b) Retention time analysis of a randomly selected memristor of the memory array. (c) Flexibility analysis of the memory array, measuring state resistances against bending diameter, the device showed open circuit behavior at diameter less than 10 mm. Hence, it is bendable down to 10 mm diameter. (d) Bendability test analysis of the device for 1000 endurance cycles.

Encapsulating the device helps to increase the retention time performance for much longer than 180 days, and the trend of measured voltage-time graph indicates the actual retention time would be much longer than 180 days. As shown in Figure 3.16c, the flexibility of the memory array was verified by analyzing resistance variations of two randomly selected memristors (one in HRS and the other one in LRS) for various bending radiuses. Their resistance variations against bending diameter was tested by wrapping the flexible array around the metal rods from 26 mm down to 8

mm in diameter. The minimum rod diameter with which the device performance is maintained was ~10 mm. Bending the device beyond this diameter caused device failures forming an electrically open circuit. A homemade automatic bending machine performed bendability test for 1000 cycles as shown in Figure 3.16d, the resistance of both HRS and LRS of the selected device was negligibly deviated. The experimental results prove that the proposed memory device is robust over cycle-to-cycle endurance, long retention time, and bendability, which are essentially demanding features of flexible and wearable electronics.When the voltage V_R is applied to devices, during the read mode, memristors maintain their previous states and the output voltages at "Data i/o" ports are produced almost instantly. Table 3.3 summarizes the voltages used/sensed and power consumptions during read/write modes. The capabilities of the extremely low power consumption and robust data read/write operations, together with its simple structure, the proposed flexible memory device can be a good candidate in low cost disposable electronics, where all components are fabricated at ambient conditions.

Table 3.3. The operating voltages of each single cell and its power consumption when reading and writing the data logic 0 and 1, the power consumption per cell is very low which enables the high integration array with low power consumption.

Parameter	Write "0"	Write "1"	Read "0"	Read "1"
Voltage	2V	-2V	0.15V	0.45V
Power	400nW	400pW	8.33nW	25pW

4.1.5 Summary

A flexible 1R-1CM RRAM memory array fabricated on a plastic substrate through the direct printing fabrication technique (EHD) was proposed. The structure of the memory device is in a simple crossbar memristors array, and the optimized pull-up resistor is added in series with each column bar to provide reading voltage during the read mode. Unlike the conventional crossbar memory, the proposed memory array read the logic data in the form of voltage levels instead of current. For data reading mode, a 0.5 V reading voltage is applied to the pull-up resistors and the electrical ground is provided through the row selector. Logic data in the form of voltage of the whole row is collected on "Data i/o" bus in parallel. For data writing mode, write voltage of ±2 V

is applied directly to the column bar one by one, that changes the state of a chosen memristor. The proposed flexible memory device demonstrated robust functionalities including reliable read/write operations, long endurance and retention time, and large voltage detection margin between logics "1" and "0". The robustness and retention time were increased by encapsulating the device with PDMS. The proposed RRAM memory is bendable down to 10 mm in bending diameter. The physical dimension of memory array can be further reduced by using high precision fabrication process for printing finer crossbar electrodes with good conductivity and uniformity.

4.2 Tri-state memory cell

Here in this section, a new architecture resistive memory based two memristor connected (2MMC) in voltage divider configuration to achieve a tri-state non-volatile memory cell is presented. The working principle of the single cell is based on voltage divider rule, voltage is dropped across both components (M1 and M2) according to their state resistance value. Due to high resistance, this memory cell consumes ultra-low power and exhibits high switching speed during read/write of the data. The proposed cell offers very high resistance which results in reduction of sneak path current and high margin between logics "1" and "0" which solving the problem of crosstalk. The schematic diagram is shown in Figure 4.1a, two memristors connected in series having three terminals. While writing data to the memory cell, T1 and T2 are connected writing voltage while T3 is grounded. To switch M1 to LRS and M2 to HRS, T1 is connected to +2V and T2 is connected +2V volt, while T3 is grounded. This combination of writing voltage switches the M1 to set/LRS and M2 to reset/HRS. The memory cell can be switched in 4 different states (LRS/HRS, HRS/LRS, HRS/HRS, LRS/LRS) by applying writing voltage at T1, T2 and grounding T3.

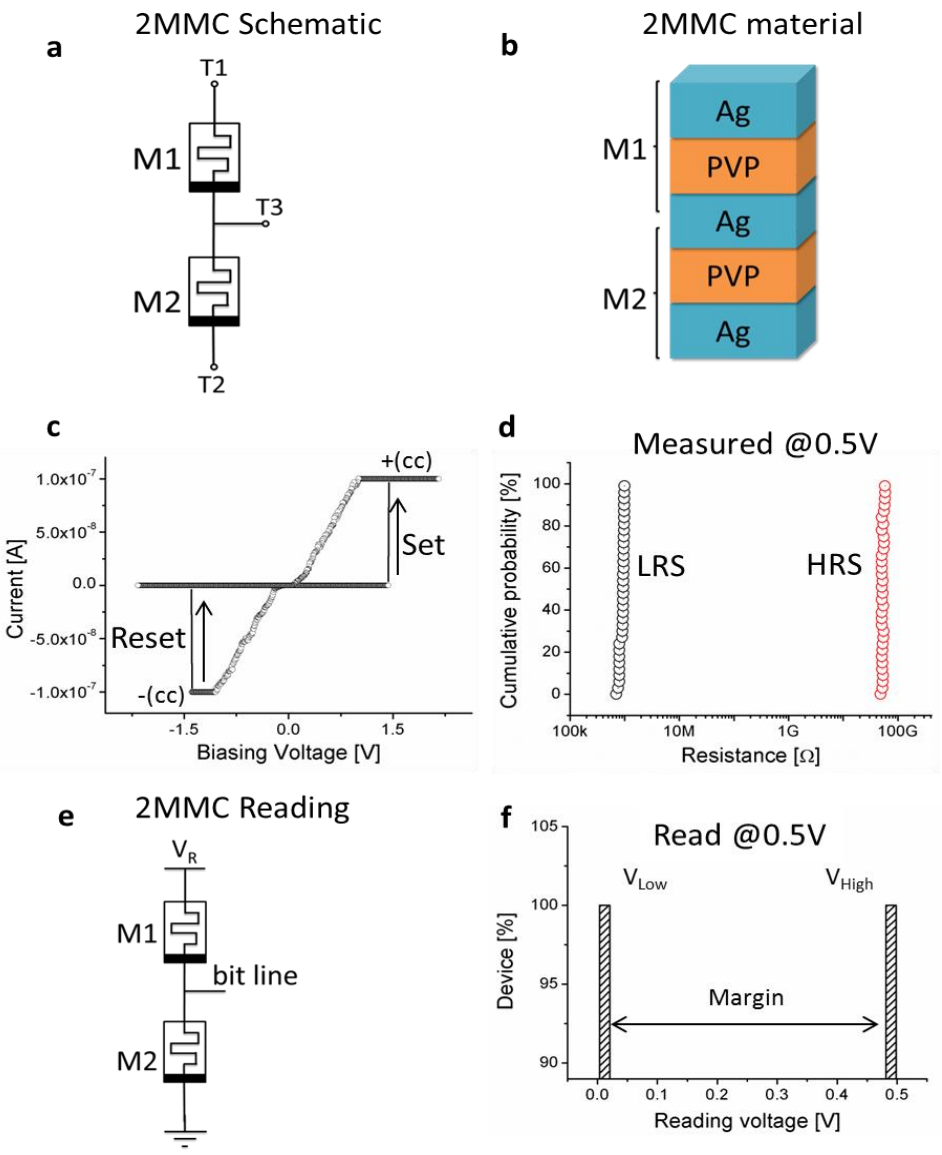

Figure 4.1. Figure 1 (a) Schematic diagram of two memristors memory cell, common point is grounded, upper terminal of M1 and lower terminal of M2 are connected to V_{Set}/V_{Reset} to control the resistive state. (b) Materials and layout diagram of the two memristors memory cell, showing layers of the device (c) Measured current voltage (I-V) curve of the typical memristor (Ag/PVP/Ag), showing large margin between HRS and LRS (~6000). (d) Cumulative probability analysis.

The materials layout diagram of 2MMC is shown in Figure 4.1b, both memristors are fabricated vertically stacked on the PET substrate by using EHD fabrication system, after curing the device it is encapsulated with Al_2O_3 to protect from environmental effects. The electrodes are fabricated of silver (Ag) and active layer is fabricated of graphene quantum dots and PVP composite. Both memristors are stacked in such way to make connection with T1 and T2, and a middle terminal which connects the common point of the memristors, the total thickness of the stacked devices is

less than 1 µm. The typical current voltage (I-V) curve is shown in Figure 4.1c for the metal insulator metal (MIM) memristor. This graph represents the switching behavior of both the memristors because of their same materials. It shows the set and reset of the memristor (M1 and M2) with distinction margin of state resistances (HRS/LRS~6375). The device is switched between HRS and LRS states with in the boundary of -1.5V and 1.5V with current compliance (cc) 100nA. To make sure the reliability of the state resistances of memristor, cumulative probability of HRS and LRS is obtained as shown in Figure 4.1d. The average value of LRS is 8MΩ and HRS is 51GΩ these values were measured at 0.5V. Once the 2MMC is written with a logic data, it can be read as the schematic circuit is shown in Figure 4.1a, ground is provided at T2, reading voltage (V_R=0.5V) is provided to T1 and bit line T3 produces the stored logic in the form of voltage levels without any delay as no switching is involved in the reading cycle. The bit line voltage ($V_{bit\ line}$) is measured against each logic data as shown in Figure 4.1f. This memory cell produces output voltage levels for data with high margin (~6000 times) and extreme low current Pico ampere (pA). The parameters of operation for read/write cycles are summarized in Table 4.1 for single bit 2MMC ReRAM. There are 4 different states of the proposed memory cell, where two states are the same in sense of reading voltage (HRS/HRS and LRS/LRS). But first two switching states provides very high margin between logic data, it is recommended to be used for the logic states.

Table 4.1. Possible states of the 2MMC and operating voltage values.

Logic value	**M1**	**M2**	**$V_{bit\ line}$(v)**	**V_R(v)**	**V_{Write}(V) M1/M2**
1	LRS	HRS	0.49	0.5	+2/+2
0	HRS	LRS	0.01	0.5	-2/-2
X	HRS	HRS	0.250	0.5	+2/-2
X	LRS	LRS	0.250	0.5	-2/+2

The timing diagram of the two memristors memory cell is shown in Figure 4.2, the memory is demonstrated for its data read/write cycles. Computer controlled signals are applied to the memory cell to read/write the data. In the 1st cycle, the cell is written for logic "1", turning the M1 to LRS and M2 to HRS by applying +2/+2 voltage respectively to the cell (0~50ms) where state of M1 and M2 can be seen in the graph LRS/HRS. To read stored data from the cell 0.5V is applied, data is appeared at the bit line in the form of voltage (0.49V) representing logic "1" (50~100 ms). In the

2nd cycle M1 is turned into HRS (reset) and M2 is switched to LRS (set) at time (100~150 ms) by applying -2/-2V at T1 and T2. At 0.5V reading voltage, the memory cell produces 0.01V at the bit line representing logic "0" (150~200 ms). In 3rd cycle, both memristors are in the LRS/LRS state by applying +2/-2V at T1 and T2 respectively (200~250 ms). While reading the logic (250~300 ms) it produces 0.25V at reading voltage of 0.5V. In 4th Cycle, -2/+2 is applied at T1 and T2 respectively which result M1 and M2 to HRS/HRS (300~350 ms).

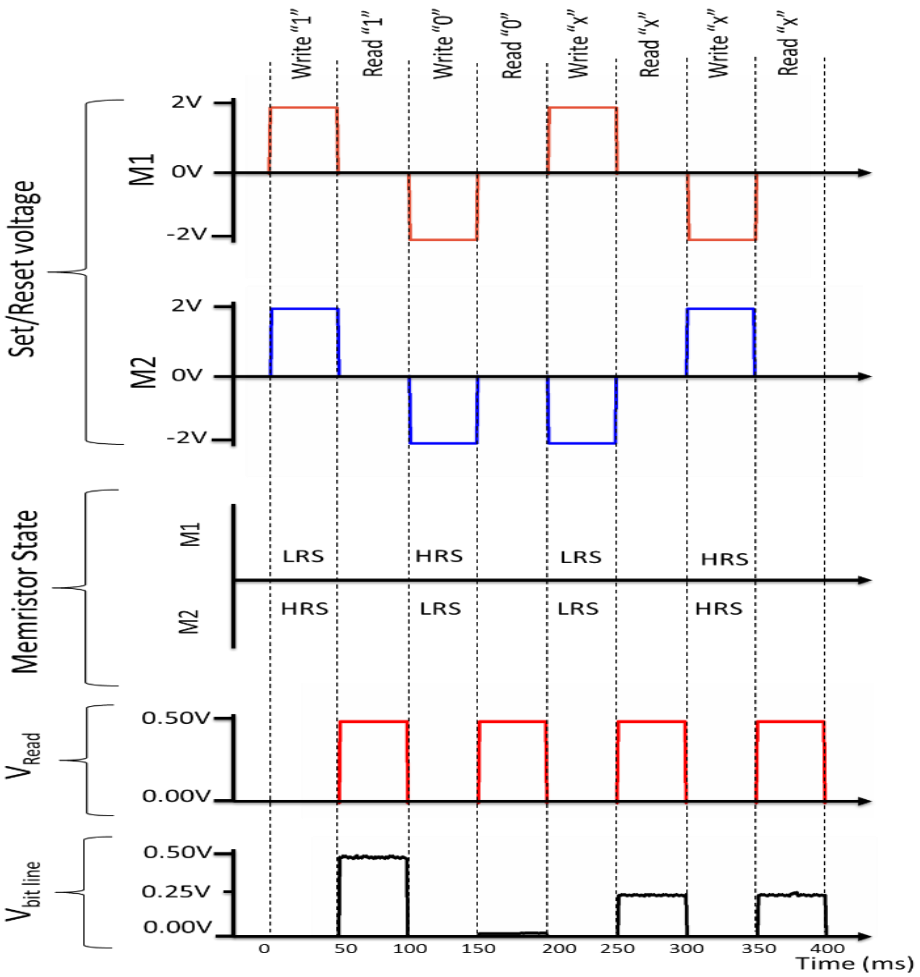

Figure 4.2. Timing diagram of the two memristor memory cell (2MMC), in each 50 ms the cell is written for the required logic and in next 50ms the cell is read, 4 possible states are demonstrated where 2 states are the same.

During read operation (350~400 ms) the output voltage is 0.25V which is same as the 3rd cycles voltages. Hence the last two states are the same as both memristors M1 and M2 is switched in their HRS or LRS states. In both cases the output voltage is 0.25V as the voltage divides equally on both memristors because of their same resistance. Hence by using first two states of the memory cell, this provides very high margin in data reading as logic "1" is at 0.499V and logic "0" at 0.001V,

this solves the problem of cross talk in the memory cells. The memory cell can be programed for the first two states by applying +2V at both ends of the memristors or -2V it turns the memristors in opposite resistance states. The proposed memory cell consumes ultra-low power, gives high switching speed and produce output with extreme high margin, due to these features, it is good candidate to be use in flexible memory applications.

4.2.1 2MMC memory array

This 2MMC ReRAM memory cell keep promise of crosstalk elimination and sneak path current reduction when an array is formed from these elements. Bottom and top terminals (T1 and T2) of memristors M1 and M2 are connected with Top row and bottom row bars respectively and common points of memristors are connected with column bars as shown in Figure 4.3. In this architecture the total resistance of a memory element from top row to bottom row is equal to HRS+LRS, as memristors switches complementary in first two logic states of the memory cell. the total resistance value against each memory state is given in Table 4.1. This extreme high resistance of the memory cell reduces the sneak path problem in addition of ultra-low current operation which makes the proposed memory extreme low power device.

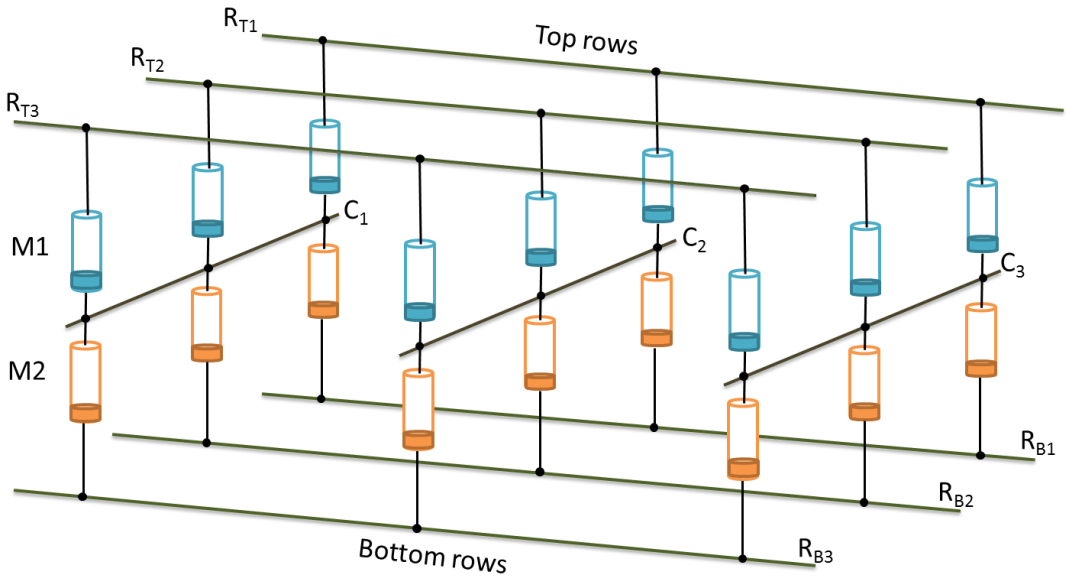

Figure 4.3. Schematic diagram of 3x3 memory array based on the 2MMCs.

4.3 References

[1] Heeger, et al., *Rev. Mod. Phys.* 1988*, 60,* 781-850.

[2] T. Sekitani, et al., *IEEE Trans. Electron Dev.* 2009, *56,* 1027-1035.

[3] S.R. Forrest, *Nature* 2004, *428,* 911-918.

[4] T. Sekitani, et al., *Science* 2009, *326,* 1516-1519.

[5] C. H. Cheng, et al., Adv. Mater. 23 (2011) 902-905.

[6] D. B. Strukov, et al., Nature 453 (2008) 80-83.

[7] L. O. Chua, IEEE Transactions on Circuit Theory 18 (1971) 507-519.

[8] R.D. Isaac, EPElP, 1998. IEEE 7th Topical Meeting on, 1998, pp. 26-28.

[9] N.Z. Haron, et al., Design and Test Workshop, IDT 3rd International, 2008 pp. 98-103.

[10] Torrezan, et al., *Nanotechnol.* 22, 485203-485213 (2011).

[11] *Jo, S.H.,* et al., *Nano Lett.* 9(2), 870–874 (2009).

[12] Jeong, H. Y., et al., *Nanotechnol.* 21, 115203–115208 (2010).

[13] Lee, M.J., et al., Adv. Funct. Mater. 19, 1587-1593 (2009).

[14] Torrezan, C., et al., *Nanotechnology* 2011, *22*, 485203-485213.

[15] Strachan, J. P., et al., *Nanotechnology* 2011, *22*, 505402-505407.

[16] Jeong, H. Y., et al., *Nanotechnology* 2010, *21*, 115203–115208.

[17] Lee, M.J., et al., *Adv. Funct. Mater*. 2009, *19,* 1587-1593.

[18] Miao, F., et al., *IEDM Tech Dig*. *(IEEE* 2009), 1-4.

[19] Hwan Kim, et al., Nano Letters 9 (2) (2009) 870-874.

[20] Cho, B., et al., *Adv. Mater.* 2010*, 22,* 1228–1232.

[21] Kim T. W., et al., *Adv. Mater.* 2009*, 21,* 2497–2500.

[22] Linn E., et al., *Nat. Mater.* 9, 403–406 (2010).

Chapter 5 Printed Organic Resistor

5.1 Introduction

Printed electronic technology is rapidly grooming in research groups and electronic industry because of its advantages over conventional rigid electronics technologies including, low cost, flexibility, rapid fabrication, and printability [1-3]. Printed organic electronic devices are somehow matured to be used in the integrated circuits and discrete electronic circuits [4, 5]. In the design of electronic circuit, the basic components are needed such as inductors, capacitors and resistors. In literature, printed inductors, printed capacitors and printed resistors are reported in the printed form with their design formulas and materials [6-10]. The resistor design is also reported in several literatures, where resistance is controlled through the dimension of resistive layer, high value resistance cannot be realized due to the fabrication facility limitations [8]. In small size electronic circuits, the component area constraint becomes dominant factor [9], hence resistivity controlled method is the best candidate to fabricate a resistor with dimensions constraint. poly(3,4-ethylenedioxythiophene):poly(styrenesulfonate) PEDOT:PSS is a conductive polymer having versatile electrical properties which are further enhanced by different techniques to utilize in organic light emitting diodes and solar cells as an electron transport layer [11-13]. Some studies presented the electrical conductivity of PEDOT:PSS is controlled by solvent to fabricate a printed resistor [14], but, with this method a wide range of resistances cannot be fabricated. In order to fabricate wide range resistances, the resistivity of PEDOT:PSS material can be controlled by blending with insulator or conductor material. To overcome the size problem resistivity (ρ) control of the material can be used to design a resistor with in the size and ohm value constraints. Resistors with different values on the same dimensions will be possible to fabricate through printing technique.

This research work is focused on the organic printed resistors to design and fabricate the required value and size resistor by using the printed electronic technology EHD, based on resistivity (ρ) control method. We are also investigating the design of a resistor with low (ohm) and high (kilo ohms and mega ohm) resistance to full fill the requirement of any type of printed electronic circuit with frequency less than 10 MHz. Materials are blended for different resistivity to control the

resistance and make the resistor in any size and value predictable to be printed. Materials used for the fabrication of the resistive layer are PEDOT:PSS, poly(methyl methacrylate) (PMMA), and silver nano-particles. Because PEDOT:PSS is conductive material, PMMA is added with different ratios to make it less conductive and increase the resistivity to a required value, and this way high value of resistance is achieved. By adding silver nano-particles with PEDOT:PSS material the resistivity of the PEDOT:PSS material is decreased to fabricate low value resistances. By adding PMMA and silver nano-particles into the PEDOT:PSS, the resistivity is changed along the materials mixing ratio. In this paper, we have proposed two resistivity design functions of the mixing ratio for both [PEDOT:PSS]:[PMMA] and [PEDOT:PSS]:[Ag], and how to get these functions. Their validity are also verified by the comparison the measured and the theoretical values.

For the printed electronic devices and circuits, there is a variety of fabrication techniques available including, screen printing, sol gel, and EHD/ESD [14-16]. All fabrication facilities have their advantages and disadvantages due to their working requirements, some fabrication techniques needs heat and vacuum chamber for the device fabrication which is not suitable for heat sensitive material. Comparatively spin coating is easy and need no such requirement but it is not for multiple devices fabrication on single substrate. Among all the fabrication facilities, the EHD technique is suitable candidate for fabrication of multiple printed electronic devices on a single substrate at ambient temperature [17]. The EHD system is to fabricate the devices as discussed in EHD section in chapter 1. In this research work I am using different materials in sense of conductivity so different operating voltages are required for the same flow rate for the stable con jet. After fabrication by EHD technique, the devices were cured and then Ag electrodes at specific length (l) were deposited on the resistive layer to make resistor's contacts. The fabricated samples of different resistors were characterized to verify their performance and the design method. Current-voltage (I-V) analysis of the samples was carried out with different voltage sweeps and current compliances. Endurance time of the proposed resistors was analyzed for more 30 days to ensure the reliability of the device in open air. Bendability test of the device was carried out up-to sub-millimeter diameter bending, to analyze the temperature dependency of the device temperature analysis test was carried out from 20 °C to 100 °C and also the frequency response of the devices was characterized to ensure the functionality of the device in AC applications. The design and fabrication method of the organic printed resistors are described in section 5.2.3, characterizations of the proposed devices are presented in section 5.3 and conclusions are given in section 5.4.

5.2 The proposed organic printed resistor

5.2.1 Material synthesis

Poly(3,4-ethylenedioxythiophene):poly(styrenesulfonate) (orgacon) was supplied by Agfa Materials Japan Limited, Japan. Poly (methylmethacrylate) (PMMA), polyethylene terephthalate (PET) substrate, ethanol, isopropanol and silver nano-particles were purchased from Sigma Aldrich, South Korea. First of all the PEDOT:PSS solution was prepared as, diluting (2.6 %wt) PEDOT:PSS with 10 ml of isopropanol and 3 ml of deionized-water, stirred at 2000 rpm for 2 hours under ambient conditions [18]. To increase the resistivity of PEDOT:PSS ink, poly(methyl methacrylate) (PMMA) was added with different ratio 1:0, 1:1, 1:2, 1:3 and 1:4. The ink was prepared as, 16 mg/ml of poly(methyl methacrylate) was mixed in isopropanol and stirred on magnetic stirrer for 1 hour. Both inks were prepared separately and then PMMA was added with different ratios to the PEDOT:PSS and again stirred for 20 minutes at 2000 rpm each separately. Silver (Ag) nano-particle paste 20 %wt was diluted in 10 ml ethylene glycol solvent, ink was mixed for 1 hour on magnetic stirrer and then 30min bath sonication. Afterwards silver (Ag) nano-particles ink was mixed with PEDOT:PSS ink with 1:0, 1:1, 1:2, 1:3, and 1:4, and stirred for 2 hours. The resistivity of PEDOT:PSS is degraded by a conductor and enhanced by a polymer insulator. In the paper, we have utilized silver (Ag) for a conductor and PMMA for a polymer insulator because they have a good electrical properties with low cost and a high solubility.

5.2.2 Resistivity control

The PEDOT:PSS is a conductive material with electrical conductivity of 7.5 μS/cm, the conductivity was reduced by adding PMMA with PEDOT:PSS, hence the resistivity increased to fabricate high value resistances. Conductivity of the PEDOT:PSS material was increased by adding silver (Ag) nano-particles to achieve low resistivity (ρ) for the fabrication of low value resistances. The relationship between resistivity and materials ratio was observed that, resistivity increased along with material's ratio in the case of PEDOT:PSS with PMMA as shown in **Figure 5.1**a. In **Figure 5.1**b, the resistivity was reduced along with the material's ratio in case of PEDOT:PSS with silver (Ag) nano-particles, both cases follows the exponential function. The resistivity of materials with five different mixing ratio was measured with resistivity meter (Pro4-440N, 4 probes resistivity meter), their resistivity and mixing ratios are summarized in

Table 5.1, for [PEDOT:PSS]:[PMMA] and [PEDOT:PSS]:[Ag]. I have obtained the theoretical formula resistivity function $\rho(x)$ in Eq. (1) based the measured values given in
Table 5.1. To design a specific value resistor, the resistivity value can be calculated by using our proposed resistivity function $\rho(x)$ in Eq. (2). This equation calculates the mixing ratio of inks to design a required value of resistor with specific dimensions. The size constraint of the resistors can be solved with our proposed resistivity control method.

Table 5.1. Materials with different ratio and resistivity for both ([PEDOT: PSS]:[PMMA]) and ([PEDOT: PSS]:[Ag particles]).

Ratio	1:0	1:1	1:2	1:3	1:4
Materials	PEDOT:PSS and PMMA				
Resistivity (mΩ-cm)	48	20.25	12.31	8.24	6.13
Materials	PEDOT:PSS and silver (Ag) nano-particles				
Resistivity (mΩ-cm)	48	71.4	105.2	150.5	210.3

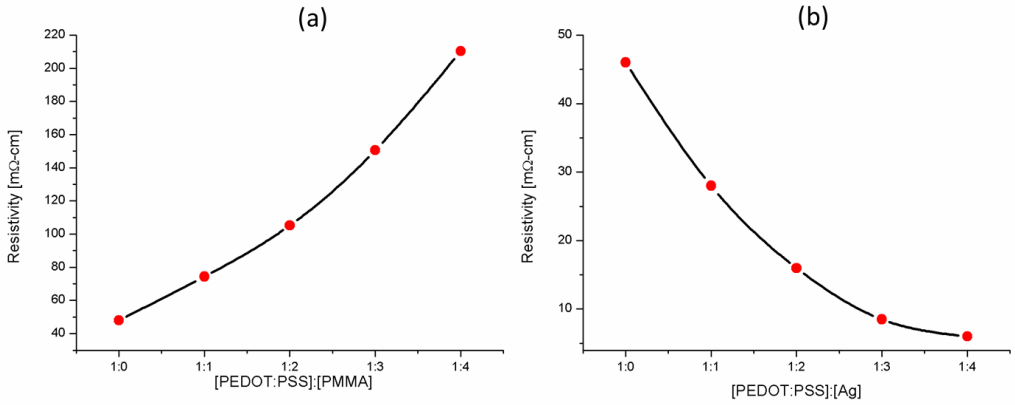

Figure 5.1. (a) Resistivity and material ratio (PDEOT:PSS and PMMA). (b) Resistivity and materials ratio (PEDOT:PSS and silver particles).

5.2.3 Resistor design

Samples of resistors were design with same dimensions but different resistivity to verify the role of resistivity (ρ) control. The physical dimensions of the samples for [PEDOT:PSS] and PMMA based resistor were w=5 mm, l =22 mm, and h=1 µm. For the [PEDOT:PSS] and silver nano-particles based resistor were w= 5 mm, l =15 mm, and h=3 µm. The resistivity values used for both types of resistor samples from Table 1. For the designing of the printed organic resistors, the following equation was used:

$$R(x) = \rho(x)\ \frac{l}{A} \tag{1}$$

Here, *x* is the mixing ratio of the inks such as PMMA/[PEDOT:PSS] and Ag/{PEDOT:PSS], *R(x)* is function for a resistance changed by variable *x*, *ρ(x)* is the resistivity function of the *x*, l is length of the resistive layer, and *A* is the cross sectional area of the resistive layer. *A* is calculated by using the width of the layer (*w*) and thickness of the resistive layer (*h*) as shown in Fig. 3a. Thickness was controlled through the ink flow rate and substrate moving velocity during EHD deposition. The function ρ*(x)* is fitted from red circles in **Figure 5.1**(This measured data values are denoted in Table 1.), I approximately set that the resistivity function of mixed ration (*x*) as

$$\rho(\mathrm{x}) = a_0 x^n + a_1 x^{n-1} + \cdots + a_{n-1} x + a_n \tag{2}$$

The coefficients $\{a_i\}_{i=0}^{n}$ are determined from circles in **Figure 5.1** as following steps: (i) To obtain more exact coefficients, there interpolate using cubic spline data interpolation [19, 20] in between circles shown in **Figure 5.1**. (ii) We can find the coefficients from optimally polynomial curve fitting as sold lines (see Fig. 2) using a least squares method [19,20]. In this work, I consider two combinations of mixed materials ([PEDOT:PSS & PMMA] and [PEDOT:PSS & Ag]). The obtained coefficients $\{a_i\}_{i=0}^{n}$ are for (2) are {0.0729, -0.2414, 5.4069, 18.1450, 48.0286} for ([PEDOT:PSS & PMMA] and {0.4603, -5.2656, 22.5304, -45.8299, 48.1806} for [PEDOT:PSS & Ag] in the mixing ratio (*x*) between 0 and 4. To verify the obtained coefficients of the function ρ(x), I have compared the calculated resistivity with the measured ones for the mixed material of ([PEDOT:PSS]:PMMA) at $x = \{0.5,\ 1.5,\ 2.5,\ 3.5\}$. The calculated resistivity and the measured resistivity are {58.43, 86.97, 126.26, 178.36} and {59.2, 88.9, 127.7, 180.4}, respectively. A norm value of the difference between the calculated and the measured resistivity is 3.25. These show the useful function to estimate the resistivity by the mixed ratio of the inks, and the proposed ρ(x) can be variously used. Using the obtained polynomial function Eq. (2), one can easily design an organic resistor from the minimization of the cost function, $\theta(\mathrm{x}) = R_{ideal} - R(x)$, where R_{ideal} is an ideal resistance. The optimum mixed ratio of the cost function, $\theta(\mathrm{x})$ can be directly obtained from an optimization method in mixed ration bound [19,20]. The layout diagram of the device is shown in Figure 5.2a and fabricated resistors are shown in Figure 5.2b. The thickness (h) was controlled through the ink flow rate and substrate moving velocity during EHD deposition. From these results

in Figure 5.1, resistors with high and low resistance can be fabricated through mixing of high resistivity material or low resistivity material with PEDOT:PSS respectively, for a required dimensions of resistor. Using the proposed design method, any value of resistance can be fabricated without of dimension limitations. However, very small value (under 50 Ω) of resistors are not feasible due to the inherent problem of the PEDOT:PSS temperature dependency.

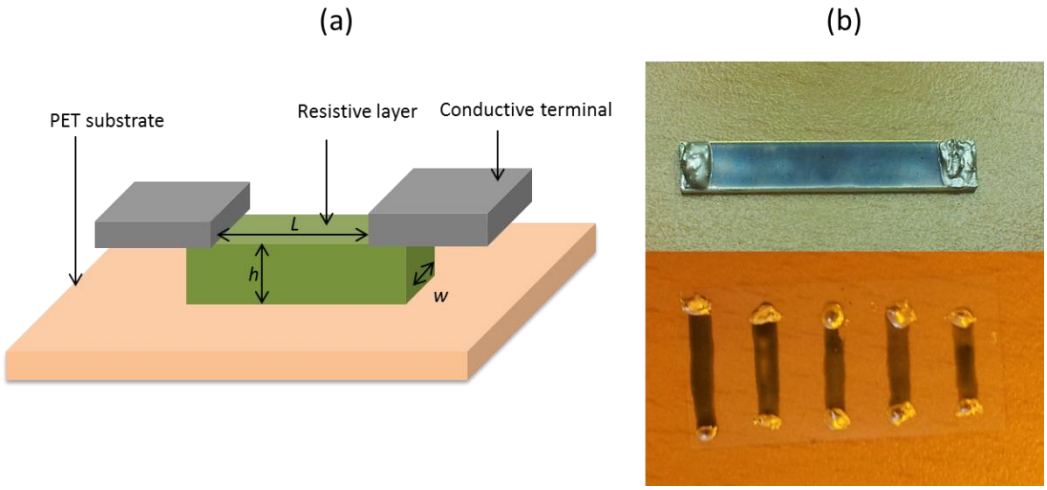

Figure 5.2. (a) Dimension of the resistive layer and material diagram of the device. (b). Fabricated organic resistors on PET substrate.

5.3 Experimental results

The organic printed resistors were analyzed for their electrical characteristics by using Agilent B1500A Semiconductor Device Analyzer. The probes were connected to the terminals of the resistor and voltage sweep from 0 V to 10 V was applied. The device showed linear behavior in the entire voltage sweep region. Five different devices of each inks with different material's resistivity (ρ) and same dimensions were analyzed, PEDOT:PSS without PMMA showed the least resistance. As the ratio of PMMA in PEDOT:PSS increases the resistance of the device also increases whereas the dimensions of all the samples are the same, the I-V analysis is shown in Figure 5.3a. By adding silver nano-particles in PEDOT:PSS ink, the resistivity of the ink further decreases and the resistance value of the device decreases, I-V analysis of the four different samples with same dimensions are shown in Figure 5.3b. As the result of these graphs, the value of resistor can be controlled by resistivity, where the dimensions are the same. Any value of resistor with required dimensions can be design by estimating the required value of resistivity, hence with our proposed

resistor design method, constraint of the resistor size can be solved. The resistance stability test was also carried out with respect to time, to analyze the time effect on the resistance value. For this characterization I fabricate an organic printed resistor with 3.15 kΩ, and the dimension for the test resistor were w=2 mm, l = 6 mm, h= 1 µm, and resistivity ρ=150.2 mΩ-cm from Table 1 (theoretical value of ρ(x) was 151.6 mΩ-cm calculated through Eq. (2).

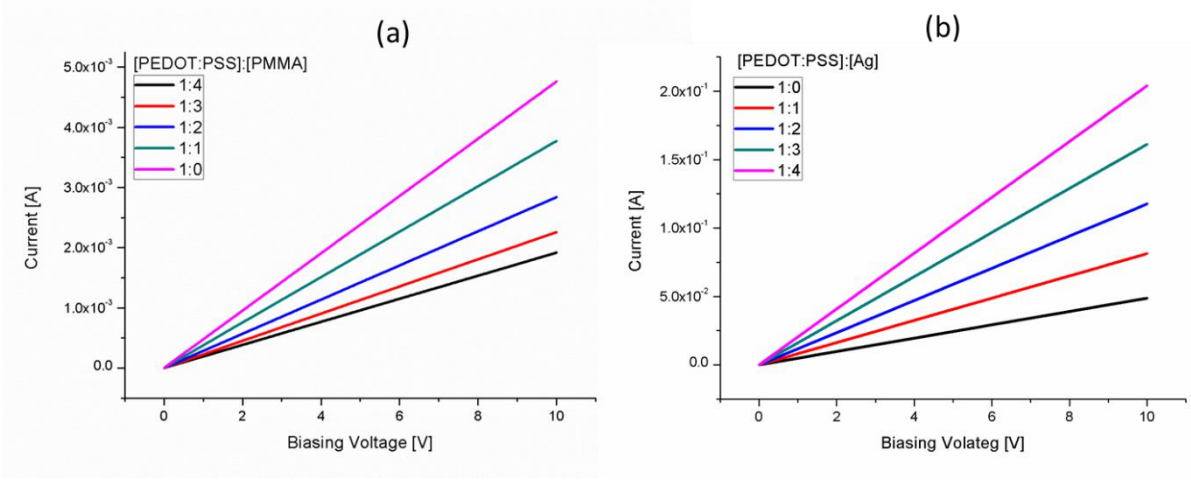

Figure 5.3. (a) Current-Voltage (I-V) analysis of different resistors with same dimensions and different resistivity. (b) Current-Voltage (I-V) analysis of different resistors.

The resistor value was measured for 30 days at 30 % humidity level, the resistance changed from 3.15 kΩ to 3.21 kΩ in 30 days as shown in **Figure 5.4**a. **Figure 5.4**b shows the current-voltage (I-V)

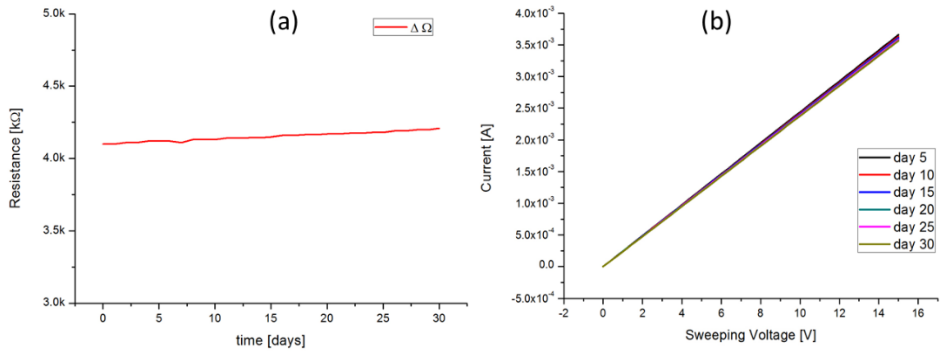

Figure 5.4. 30 days analysis of the organic resistor: (a) Resistance measurement, (b) Current-Voltage (I-V) analysis of the organic resistor after each 5 days.

curves of the resistor measured in 30 days. A small change in the current degradation along the time can be seen, which shows the resistance increment along the time. Since the PEDOT:PSS is humidity dependent material, the resistivity changes along humidity level. For this property, it is frequently utilized in fabrication of humidity sensors [21, 22]. To reduce the humidity dependency,

it should be properly coated with Polydimethylsiloxane (PDMS) or Al_2O_3. From the results, it is concluded that the resistance value is maintained with the stability reliably; hence this resistor is durable and can be used for long life printed electronic circuits.Resistor was analyzed for its temperature dependency [23], for this test the resistor was kept on a variable temperature heater, and values of the resistance were recorded against the temperature values. It was concluded that, the resistor made up with PEDOT:PSS and PMMA 1650Ω (l=7 mm, w= 3 mm, h=1 µm, ρ=71.4 mΩ-cm) is more affected by temperature, and the resistance was increased along the temperature from 1650Ω to 1842Ω. PEDOT:PSS and silver nano-particles based resistor did not show much dependency on temperature, the fabricated resistance was resistance 120 Ω (l=6 mm, w= 3 mm, h=1µm, ρ=6.13 mΩ-cm) and after it increased from 120 Ω to 165 Ω as shown in **Figure 5. 5**a. As a conclusion of temperature analysis, these resistors are good for low temperature applications only.

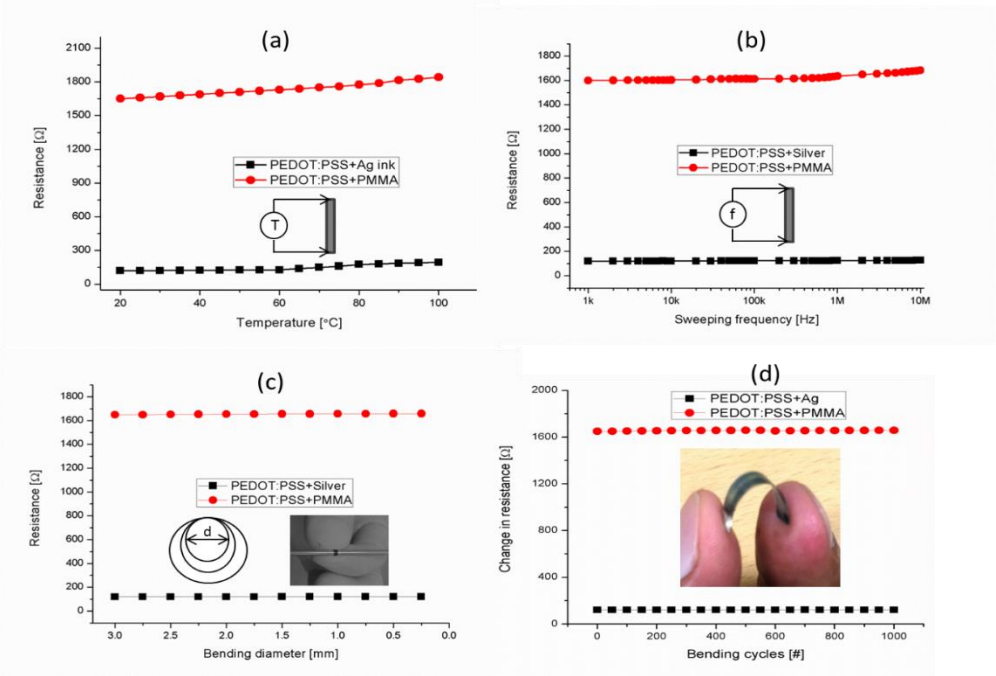

Figure 5. 5. (a) Temperature analysis of the organic resistor. (b) Frequency analysis of the organic resistor. (c) Bendability analysis of the printed organic resistor. (d) Bending endurance analysis of the device for 1000 cycles.

However, when the resistance value is lower, it allows high current which results in rising the temperature of the device and affects the performance. To prevent temperature influence on the resistance performance, it is advisable do not fabricate such low value resistors due to it will consume high power and the temperature of the device will rise. Organic resistor was also analyzed for the frequency response by using impedance analyzer, a frequency sweep was applied from 1 kHz to 10 MHz, it was observed that the PEDOT:PSS and PMMA based resistor showed increment in resistance after 1 MHz frequency, in PEDOT:PSS and silver particles based resistor did not show

much variation in resistance as shown in **Figure 5. 5**b. As a result of this characterization these resistors can be used in such electronic circuits where the frequency is less than 10 MHz. Bendability analysis was carried out for both types of resistors, resistors were wrapped around the rods of different diameters, starting from 3 mm and reducing to 0.25 mm and at each bending diameter the resistance value was recorded as shown in **Figure 5. 5**c. There was (120 Ω) ohms change in the value of resistance which is ignorable. The bending endurance test was carried out on both resistors to make sure the reliability of the devices, both resistors were bent at 0.25 mm diameter rod for more than 1000 times as shown in **Figure 5. 5**d. Hence these results confirmed that, these resistors are good candidates for flexible electronic circuits up to sub-millimeter bendability.

5.4 Summary

Organic resistors based on resistivity (ρ) control method have been proposed in this paper. Materials used for the fabrication are poly(3,4ethylenedioxythiophene):poly (styrenesulfonate) (PEDOT:PSS), poly(methyl methacrylate) (PMMA), Silver nano-particles ink, Polyethylene terephthalate PET flexible substrate, ethanol, isopropanol, and silver (Ag) paste. Inks were synthesized to achieve high and low resistivity values to full fill the area and size constraints of the printed resistor. Resistivity of the material was controlled by changing the ratio of silver nano-particles and PMMA with 1:0, 1:1; 1:2; 1:3; and 1:4 in PEDOT:PSS ink, and resistivity values were recorded for both types against each mixing ratio. The resistivity estimation function ρ (x) was also proposed to estimate the required resistivity for the design of resistor by mixing a particular ratio of inks. The validity of resistivity estimation function was verified by comparing measured and theoretical values of resistivity and found the results with 2% error. To verify the proposed method, resistors with same dimensions and various resistance values were fabricated by using resistivity (ρ) control method. Current-voltage (I-V) characterization was carried out of resistors with different resistivity of material and device dimensions. Stability of the 3.15 kΩ resistance was characterized for 30 days, the resistance value was changed only by 3.1 %. Which shows a reliable organic resistance to be used in next generation printed electronics for integrated circuits or discrete electronic circuits. I also showed the resistors are flexible and can be bend till 0.25 mm for more than 1000 times. The fabricated resistors were analyzed for temperature dependency. A negligible change in resistance was found from 20 °C to 60 °C, it is suitable to be used at ambient temperature. Frequency analysis of the resistors were also carried out, and found to be used in circuits operating at frequency less than 10 MHz.

5.5 References

1. M. Berggren, et al., Nat. Mater. 6, 3 (2007)
2. M. Chason, et al., MRS Bull. 3, 471 (2006)
3. K. Lian, et al., ECS. Trans. 6, 35. 3074 (2008)
4. Sekitani et al.,MRS Bull. 37, 236 (2012)
5. S. K. Volkman, et al., MRS Proceedings 814, I7.8 (2004)
6. Liangbing Hu, et al., Appl. Phys. Lett, 96, 183502 (2010)
7. Aleksandar B. et al.,IEEE Trans. Elect. Devices 60, 2 (2013)
8. Sungjune Jung , et al., Organic Electronics 14, 699 (2013)
9. Adam C. et al., Adv. Funct. Mater. 20, 28 (2010)
10. J. Chen , C. Li , and G. Shi J. Phys. Chem. Lett. 8, 4 (2013)
11. Jaber Saghaei, et al., Organic Electronics 19, 70 (2015)
12. Wenfeng Zhang, et al., Organic Electronics 15, 3445 (2014)
13. Amare Benor, et al., Organic Electronics 11, 938 (2010)
14. Yijie Xia et al., J. Appl. Phys. 98, 1 (2005)
15. J. J. Yang, et al., Nanotechnology 20, 215201 (2009)
16. M. N. Awais et al., Jpn. J. Appl. Phys. 52, 5 (2013)
17. I. Hayati, et al., Nature 319, 41 (1986)
18. M. Nardesa, et al., Org. Electron. 9, 7 27 (2008)
19. W. H. Press, et al., Numerical Recipes in C, 2th ed. (Cambridge, New York, 1992)
20. J. Stoer and R. Bulirsch, Introduction to Numerical Analysis, (Springer-Verlag, New York, 1980)
21. Peter Pacher, et al., Sensors and Actuators B Chemical 145, 181 (2010)
22. Yotsarayuth Seekaew, et al., Organic Electronics 15, 2971 (2014)
23. E. Vitoratos, et al., Organic Electronics 10, 61 (2009).

Chapter 6 Light Emitting Device

In the present era of smart and intelligent electronics, electronic display is needed everywhere to facilitate the users. Extending these displays from TV, computer and smart phones to advertisements big size LED displays on the streets [1]. Printed electronic technology and organic materials making the realization of environment friendly, large size very thin displays fabricated on papers and plastic substrates by direct printing technique [2],[3]. Many researchers studied thin film displays based on OLEDs [4],[5]. To operate LED display it needs a driving circuit capable of high current, which is a constraint of printed transistors. A display with electronic memory to hold data can be used for food canes and wrappers to show the manufacturing date and health of the food inside. During transportation and handling of the most sensitive chemicals or food the health can be affected by virus, temperature, and shocks therefore, continuous health monitoring is the best available option. The same concept can be used for the posters and hanging banners used for advertisement by using the disposable electronic display. In this case, the price of the electronic display must be comparable with the wrapper of food or banner. To fabricate this kind of display, it must be of low cost comparable with colored ink used for the posters or wrappers and second most important thing is it should be highly environment friendly as it is direct interacting with food and air. Flexible display, flexible memory and disposable Electronic circuits are feasible in printed electronics [6],[7]. However, in large-scale printed electronic circuit's excessive mechanical and electrical stress, high switching power, and distribution are the basic limitations for high-dense electronic applications [8]-[10]. At the present time large scale circuits are not practical in printed electronic, but somehow in low scale integration of devices implementation is feasible. To reduce the number of devices in printed electronic, devices needs to be integrated and compact to avoid power, space and interconnections between the devices.

In 2008, the HP labs fabricate the first memristor and they physically demonstrate the properties of this special 4^{th} circuit component [11]. The memristor basic functionality is that it can switch between two resistive levels in analog way and it can memorize the last used state either it was in high resistance state (HRS) or Low resistance state (LRS). If the active layer of a memristor is consisted of ionic transition metal complex, it can emit light along the resistive switching [12].

6.1 Printed Light Emitting Device

In this section, I demonstrate an organic light emitting device (OLED) fabricated through EHD printed technology at room conditions on PET substrate. This is a two terminals device that can be switched between ON and OFF states by applying external threshold voltage. Once the device is switched in either state, it retains the state for long time act as non-volatile memory. If a voltage below threshold is applied to the device, it starts emitting light if it is in ON state. The device emit light in one polarity, it is optically unipolar.

6.1.1 Fabrication

The materials used in this research work were purchased from Sigma-Aldrich South Korea.
Indium tin oxide (ITO) coated PET was used as a substrate, the substrate was cut in 22x20 cm dimensions then substrate treatment was carried out in acetone for 15 minute in stirring bath and then washed with deionized water for few dips, afterwards UV and plasma treatments were carried out to make the substrate hydrophobic for better ink adhesion. The fabrication facility Electrostatic spray Deposition (ESD) system was used for the deposition of active layer and switching layer. The ink flow rate was set to 60 ul/h with X-Y axis movement velocity of 5m/s and voltage at 5.6 KV for active layer and for the G-O layer, 4.5 kV with 120 ul/h. The nozzle used in this experiment was 110 µm with substrate to nozzle distance of 18 mm.

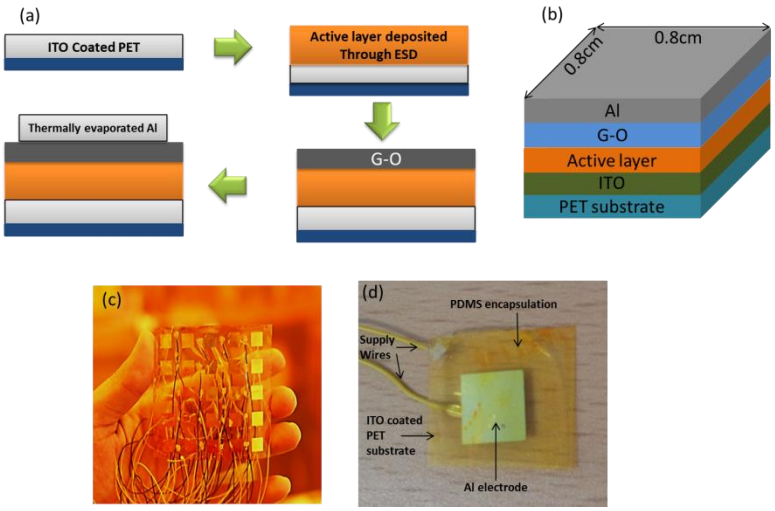

Figure 6.1. (a) OLED fabrication steps. (b) Dimensions and material layers of single cell OLED device. (c) Fabricated 5x5 array of OLED devices on PET substrate. (d) Fabricated device zoomed image of single cell.

The device was fabricated in a clean room under the normal room temperature and atmospheric pressure, no chamber was used throughout the fabrication process. The device was cured at 130 °C for 2 h. After curing the device active layer properly, a mask of 5x5 array having cell size of 0.8x0.8 cm was placed on the active layer and top electrode (15 nm) was deposited by Al thermal evaporation. The Fabrication steps are shown in Figure 6.1a, material and layer diagram is shown in Figure 6.1b, fabricated array of 5x5 OLED devices on single PET substrate is shown in Figure 6.1c and zoomed image of single cell is shown in Figure 6.1d.

6.1.1.1 Electrical characterizations

A single device can be switched between on and off states by external voltage, hence they can be programed for a specific character by placing them in matrix form. For this characterization, a 5x5 array was fabricated by using the OLED devices as shown in Figure 6.2a. Desired devices were switched in on state while the other devices were switched on off state of the array. By applying voltage of 3.8V, the array showed character "J" which was programed and all other devices showed no light while all devices are connected to 3.8V shown in Figure 6.2b. This characterization shows that by making an array of the OLED devices, desired character can be displayed. This device serves as memory and light emitting device.

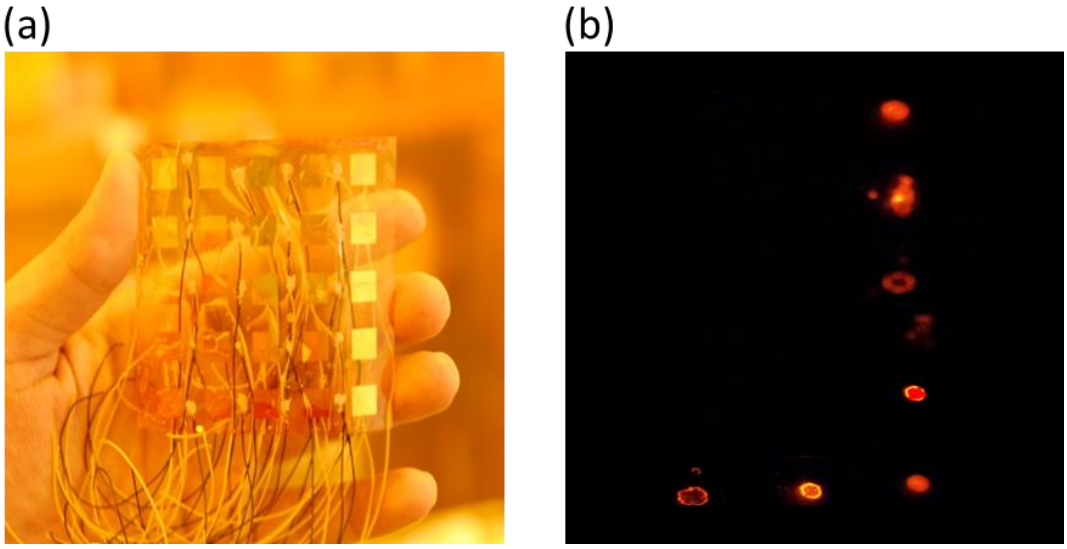

Figure 6.2. (a) 5x5 OLED device on PET substrate before programing and bias (b) OLED device show J character at 3.8V.

6.1.1.2 Luminous characterization

High voltage analysis of the proposed device was carried out to analyze the luminous as a function of applied voltage and current. For this test, a variable voltage supply was used along a current meter and device was placed on a lux meter and then placed in a black box to measure the light intensity of the device. Firstly, the device was switched in LRS state and voltage was applied across it. It was observe that the light intensity increases as the input voltage crosses 4V and keep increasing till 10V as shown in **Figure 6.3**a. the device gave stable performance till 10 volt where 5 lux light intensity was record, at 12 V the device burned out. Due to memristive behavior the initial value (until 4v) of light intensity is very low because the memristor is in OFF state (HRS), after this

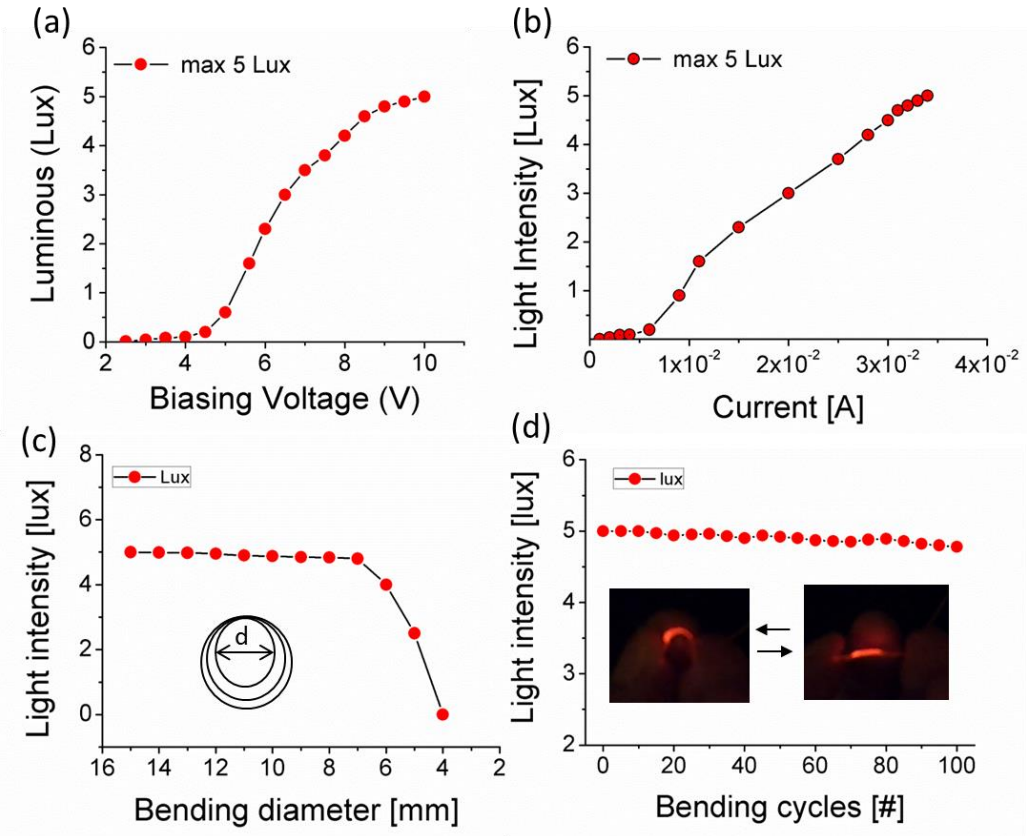

Figure 6.3. (a) Light intensity in lux vs biasing voltage. (b) Color coordinates. (c) Bendability analysis. (d) Bending endurance cycles.

Value the device almost follows resistive path, as the voltage increases the light intensity also proportionally increases, the ohmic behavior of the device after 4V can be seen in the light intensity vs current graph. At 4V few filaments take place and with increasing voltage number of filaments increases, the current value follows linear path after filaments formation and reaches its limit at 30 mA. Beyond 30 mA the device became open circuited because of excessive current through the

device which fuses the filaments. As the device is fabricated on flexible substrate PET and encapsulated with PDMS, it is bendable. The flexibility test is carried out by bending the device on different metallic rods having diameter from 15mm to 2 mm. till 7mm the device showed normal behavior, beyond this diameter the device showed high resistance and reduced the light intensity as shown in **Figure 6.3**c. Bendability endurance test is carried out by bending the device at 8mm diameter for 100 cycles as shown **Figure 6.3**d. The device showed negligible changes in the light intensity, which ensures the device application in the flexible electronic. Device was also analyzed for the wearable electronics applications to check the compatibility with wearable devices while the OLED is on. Voltage was applied to the device and it was bend with fingers as shown in Figure 6.4.

Figure 6.4. Device bending test under biased conditions.

6.2 References

[1] C. David Müller, et al., Nature 421, 829-833 (2003).
[2] H. Takao, et al., Proceeding of the 34th European , pp.309,312, 21-23 Sept. 2004.
[3] Jong-Kwon Lee, et al., Electron Device Letters, IEEE , 31, 8, pp.833,835, Aug. 2010
[4] Raffaella Capelli, et al., Nature Materials 9, 496–503 (2009).
[5] Hajime Nakanotani, et al., Nature 136, 9256–9259 (2014).
[6] Wang ZQ, et al., IEEE Electron Device Lett 2011, 32:1442–1444.
[7] Kim S, et al., Nano Lett 2011, 11:5438–5442.
[8] Kim S, et al., IEEE Trans Electron Devices 2009, 56:696–699.
[9] D.B. Mitzi, Solution Processing of Inorganic Materials, John Wiley Sons, Inc., New Jersey, NJ, 2009.
[10] T. Prodromakis, et al., Proc. IEEE CNNA Conf. (2010).
[11] D.B. Strukov, et al., Nature 453 (2008) 80–83.
[12] R. Waser, et al., Nature Materials **6**, 833 - 840 (2007)
[13] C. H. Wang, et al., IEDM Tech Dig.2010, pp. 664-667.
[14] J.J. Yang, et al., Nanotechnology 20 (2009) 215201.
[15] N.G. Hackett, et al., IEEE Electron Device Lett. 30 (7) (2009) 706.

Chapter 7 Printed Sensors

7.1 Temperature sensors

Among the printed electronic devices, printed temperature sensors have been studied from many aspects including materials, geometry, fabrication technique and substrates [1]-[5]. There are two main types of temperature sensors contact based temperature sensor and non-contact temperature sensors. Contact type of temperature sensors are required to be in physical contact with the object being sensed and use thermal conduction to monitor temperature changes, whereas, the non-contact type of temperature sensors use convection and radiation. These sensors can be used to detect solids, liquids, or gases over a wide range of temperatures. To measure the temperature of a human skin, integrated circuit chips based on contact type temperature sensors were demonstrated [1]. Even though these sensors give high resolution and accuracy, the architecture is complex and rigid. To fabricate this type of sensors, conventional electronics manufacturing systems based on lithography are used due to well precise, controlled and capable of reproducing the exact parameters of the device. However, this fabrication process is quite complicated, time consuming and requires various steps, control of temperature and pressure, the throughput limitations, lack of batch processing, rigid substrates and use of corrosive chemicals [6]-[11]. To keep apart from the complex fabrications of the electronic chip sensors, many researchers have studied metal-based printed temperature sensors utilizing including platinum, gold, and copper materials to achieve higher temperature coefficient of resistance (TCR) [6]-[8]. However, these materials cannot be processed on flexible substrate as their curing temperature is very high [10],[11]. Comparatively, silver (Ag) material is cheap and commercially available in the form of nanoparticles ink, which can be used for low cost fabrication of flexible temperature sensors through printing techniques. The melting temperature of Ag is compatible with plastic and paper substrates. In flexible electronics, PET substrate is commonly used which have melting temperature around 260°C. Temperature sensors based on Ag are reported on flexible substrates using printing technologies [12],[13]. However, when a metallic thin film pattern is deposited on a flexible substrate at low temperatures, its resistivity varies along the bending diameter because of the compression and tension of the film particles as shown in Figure 7. 1. Hence, it introduces a measurement error in temperature and cannot be used in wearable electronics [14]. In order to measure accurate temperature of flexible or

curved surfaces such as in wearable electronics [15],[16] the sensor should be stable against mechanical stresses.

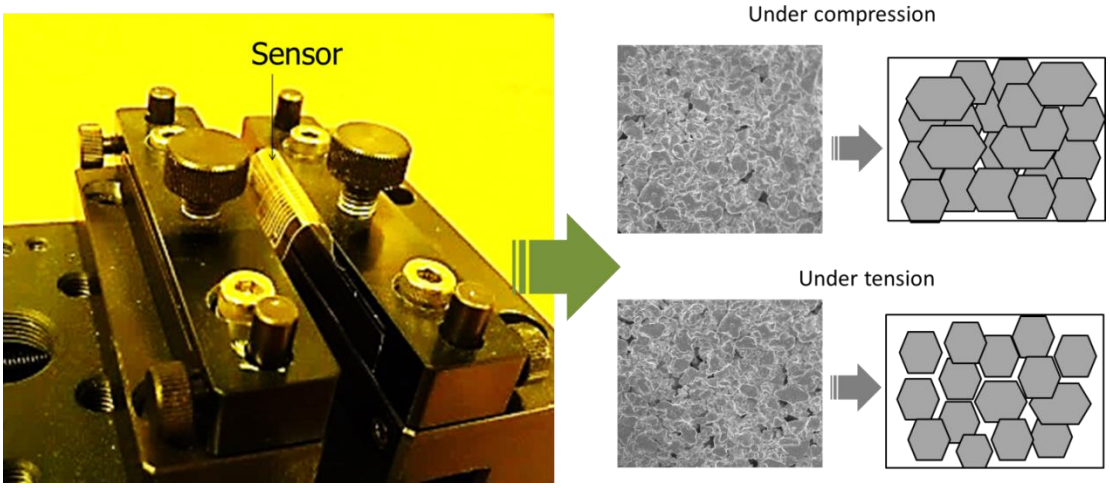

Figure 7. 1 Silver pattern printed on PET substrate for temperature sensor application, the pattern resistance varies under compression and tension.

7.1.1 Bending effects of metallic temperature sensors

In this work, I propose a differential temperature sensor through inkjet material printed technology at room temperature in a single step. The proposed sensor can be used to measure the temperature on curved and flexible surface, moreover it can measure a bending curvature of a body at the same time. The design of the proposed sensor is consisted of two back-to-back printed meander coils connected in series. Under mechanical bending, one meander pattern observes tension while the opposite side pattern observes compression and vice versa. Due to the resistance of a single meander coil increases under tension and decreases under compression when this serial connection of meander patterns is used, overall resistance of the sensor is consistently maintained. From these differential values of each resistance, bending and shape can be also detected. Each meander pattern is fabricated on a plastic PET substrate by utilizing silver nanoparticles ink with line width of 300 µm and spacing between lines is 400 µm. Dimatix inkjet material printer DMP-3000 is used to deposit the metal wire pattern in a single step at ambient conditions. To achieve precise patterns, parameters of the printing facility such as drop spacing, drop velocity, and substrate temperature were optimized. The fabricated device was cured at appropriate temperature and characterized for temperature and strain sensing in straight and curved positions. Morphological characterizations were carried out through scanning electronic microscopy (SEM) and microscope. The low cost

differential temperature sensor is fabricated in easy and single step fabrication process, which eliminates temperature measurement error caused by bending under various stresses and measure it's bending as well.

7.2 Differential temperature sensor (DTS)

This problem is overcome with proposed differential temperature sensor (DTS) as the layout diagram is shown in **Figure 7.2**a. It is a back-to-back printed sensor on a flexible PET substrate with the same pattern and size. As the connection diagram shown in **Figure 7.2**b, both side patterns are connected in series. For the temperature sensing, terminals 1 and 3 are used, for the strain sensing terminals 1 and 2 or 2 and 3 are used of the DTS. The schematic diagram is shown in **Figure 7.2**c, two resistors R_A and R_B are representing the sensors on side A and side B. If the DTS is bent on side A, the resistance of meander coil A will decrease because of compression while on side B the resistance would increase because of tension. Bending the differential sensor on either sides, the resistances R_A and R_B varies differentially and the total resistance of the sensor remains unchanged under mechanical deformation as shown in Figure 7.2d. The resistance remains unchanged as one resistor observes $-\Delta R$ while the other side resistance observe ΔR, hence both sides cancel out their change in resistance when they are in serial configuration. The temperature can only change the total resistance of the differential temperature sensor without the mechanical deformation, as temperature would increase the resistance of both serially connected resistances. This differential resistance variation suggests that the back-to-back printed sensor could be installed to measure the temperature of curved, circular or flexible surfaces. To demonstrate the proposed DTS for flexible surface temperature measurements, I have connected one ohmmeter with the terminals 1 and 2 and another ohmmeter was connected with terminals 2 and 3 of the sensor. The DTS was bent from 8 mm down to 2 mm. It was observed that the resistance was drastically increased from 73 Ω to 78 Ω of ohmmeter 2 ($R_A+\Delta R$), and from 73 Ω down to 65 Ω of ohmmeter 1 ($R_A - \Delta R$) as shown in **Figure 7.2**d. ΔR is the change in resistance due to bending effect of the sensor over the surface. By bending the sensor on either side, it observes change in resistance for R_A and R_B differentially. By measuring the resistance of one side sensor pattern, the curvature of the implanted body can also be detected. If the resistance is increased with $+\Delta R$, it shows that the body is bending in convex shape while in reduced resistance case with $-\Delta R$, it indicates that the body shape is concave. When the ohmmeter was connected across terminals 1 and 3 of the DTS, a nominal changed (below 1 Ω) was

observed against bendability of 2 mm diameter as shown in Figure 7.2d. Hence, the proposed differential sensor remained stable under bendability stress showing the accurate temperature measurement as shown in the inset of Figure 7.2d.

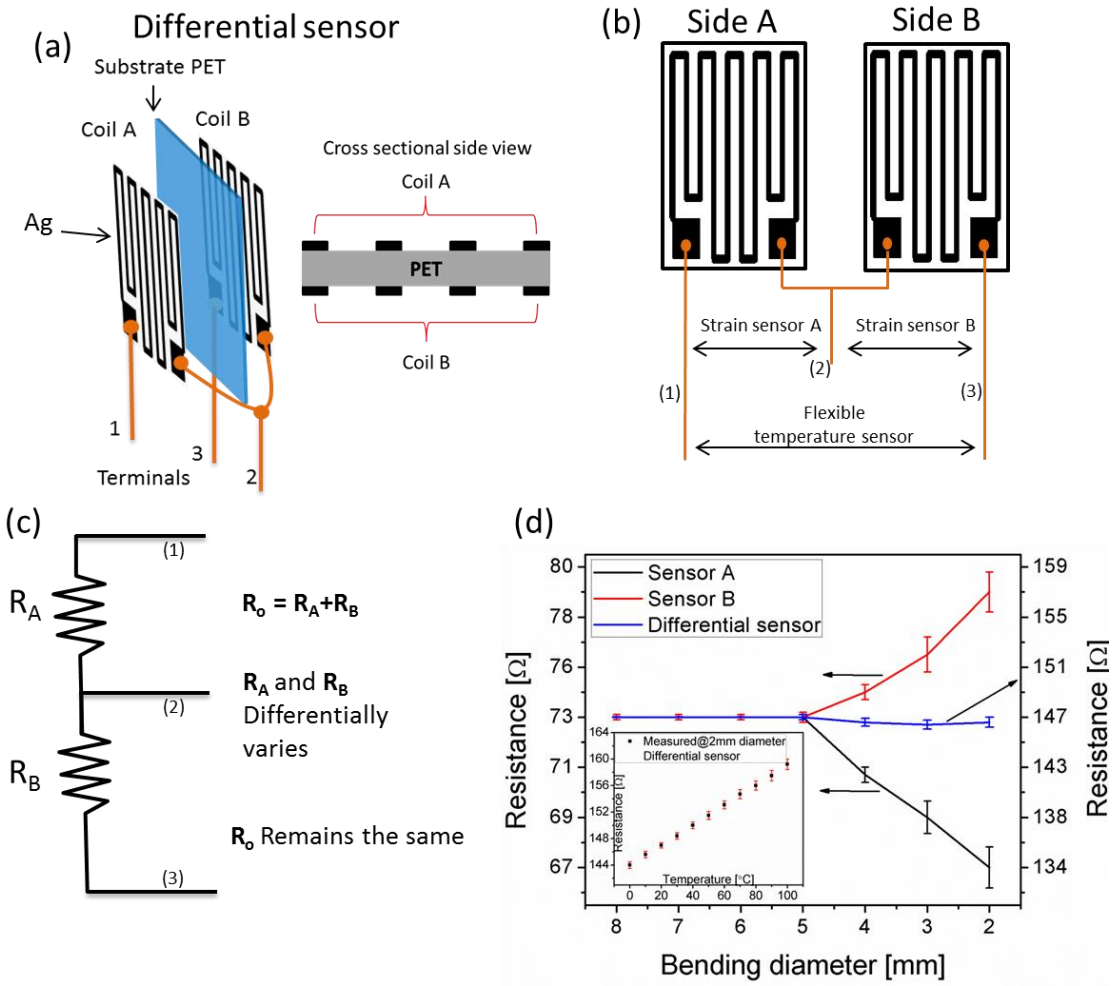

Figure 7.2. (a) Layout diagram of the back-to-back printed differential sensor. (b) Connection diagram of the back-to-back printed sensor. (c) Schematic diagram of the differential sensor consisted of R_A and R_B. (d) Bending analysis of the differential temperature sensor, only sensor A, only sensor B and differential sensor, that drastically reduces the mechanical deformation effect.

7.2.1 Mechanical characterization

To ensure the bending reliability of the DTS for wearable electronics, it was bent over 5 mm diameter for more than 300 cycles and at each cycle the resistance was measured, the sensor did not show any change in resistance value as shown in Figure 7.3 with solid line. When the sensor was bent over 2 mm diameter for 300 cycles, a negligible change (as shown by solid red circles in Figure 7.3) in sensor's resistance was observed. However, the overall behavior of the DTS remained stable

under deformation. These results suggest that the proposed temperature sensor can be used in flexible and curved surfaces for the measurement of the temperature. For the practical application demonstration, I have installed the DTS an electric motor body, the resistance against temperature was recorded. The sensor was installed on a curved electric motor body and run for 30 min. As the resistance of the sensor and temperature curve shown in Figure 7.3 b, it can be seen that the sensor behavior is linear as compare to the straight position measurements of the sensor. In this case, the resistance values of the proposed DTS can measure the temperature variations without affected by the body shape of the motor body. On the motor body, the resistance R_A = 73.35 and R_B = 74.4 were measured, the bending shape can be estimated as concave as R_A is decreased and R_B is increased.

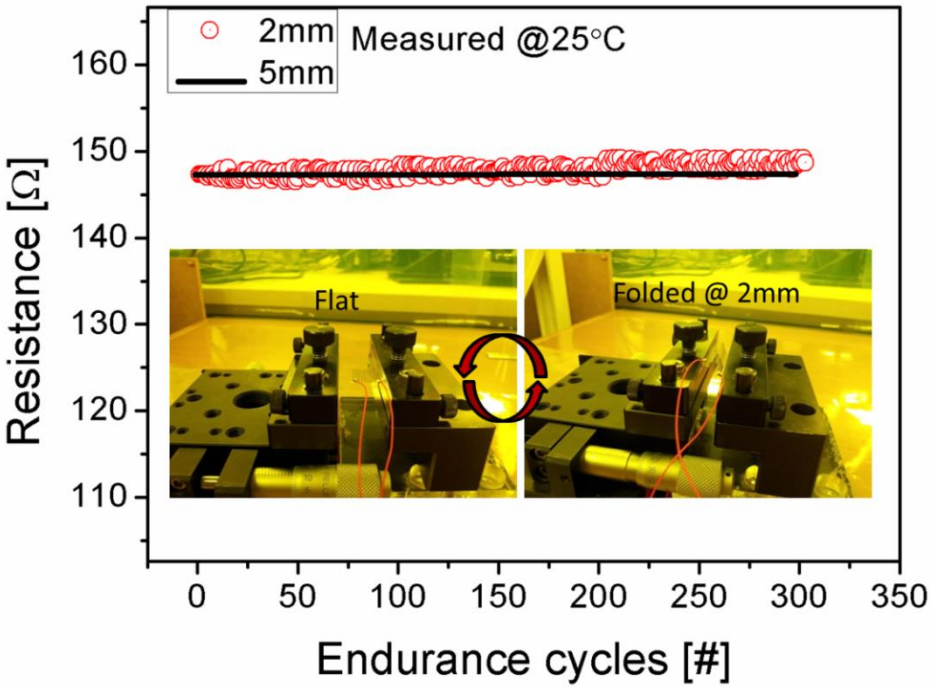

Figure 7.3. Bending endurance test of 300 cycles, the sensor in differential mode was bent on 5mm and 2mm diameter by using homemade bending machine.

7.2.2 Sensor fabrication

Schematic diagram of the meander patterns for the proposed differential sensor were designed in ACE 3000 version 7. Four different patterns were designed to observe the length dependency of the temperature sensor as well as the bending effects, the sensors geometry is shown in Figure 7.4. Firstly, I have fabricated single sided meander patterns to analyze temperature and bending sensing ability.

Secondly, we have fabricated the differential temperature sensor to overcome the mechanical deformation effects of the flexible surface. In all cases, the track width is 300 µm, spacing between lines is 400 µm, and lengths of the patterns are 75, 150, 225, and 300 mm respectively. These designs were exported to ACE 3000 software in drawing exchange format that contains all the geometrical dimensions of the design. The file was converted to bitmap image file format by using ACE 3000 software and then I exported the bitmap file in the Dimatix Drop Manager (software to control Dimatix Printer) which converted the bitmap file into its compatible format. Ag ink (3 ml) was loaded in the cartridge containing 16 nozzles. Silver nanoparticles paste (purchased from sigma Aldrich) 55 wt% is diluted in 10 ml ethylene glycol solvent mixed for 1 hour on magnetic stirrer and then 20 min bath sonication.

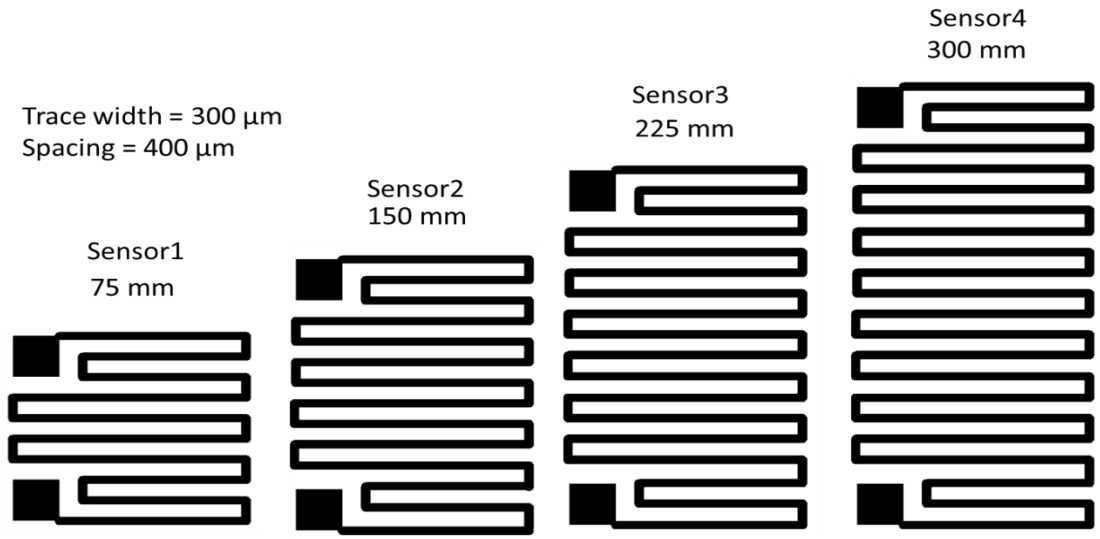

Figure 7.4. Layout diagrams of the single sided four different meander patterns for the realization of temperature sensing and bending effects.

Ag ink has a surface tension of 36.7 mNm (analyzed with surface electro optics), viscosity of 11.3 mPa.s (by using Viscometer VM-10A system), and specific gravity of 1.66 gm/ml. Prior to printing, the substrate was pretreatment with ethanol and distilled water for 5 min each. Silver nanoparticle ink was printed with a commercial drop-on-demand (DoD) Dimatix DMP-3000 material inkjet printer with a 10 pL cartridge drop size. The coffee ring effect occurs when the substrate temperature is not appropriate [17]. To overcome the coffee ring effect, the printhead temperature was set to 25°C and the stage was set to 30°C. Afterward, the samples were cured at 130°C for 30 min.

7.2.3 Surface morphology

The fabricated temperature sensors on a plastic substrate are shown in Figure 7.5a, and Figure 7.5b shows the zoomed image of the single sensor. Microscopic image of the silver line is shown in Figure 7.5c, it can be seen that the silver ink is deposited uniformly on the PET substrate. For the high-resolution morphology, scanning electron microscopy (SEM) analysis was carried out as shown in Figure 7.5d. Small pours were found in the silver line, this increase the overall resistance of the silver line and provide high resistance variation under bending. In other words, the resolution of the strain sensor is increased due to porous film. To make a differential temperature, two meander patterns were fabricated back-to-back on a PET substrate and connected in series by using silver epoxy and connecting wires.

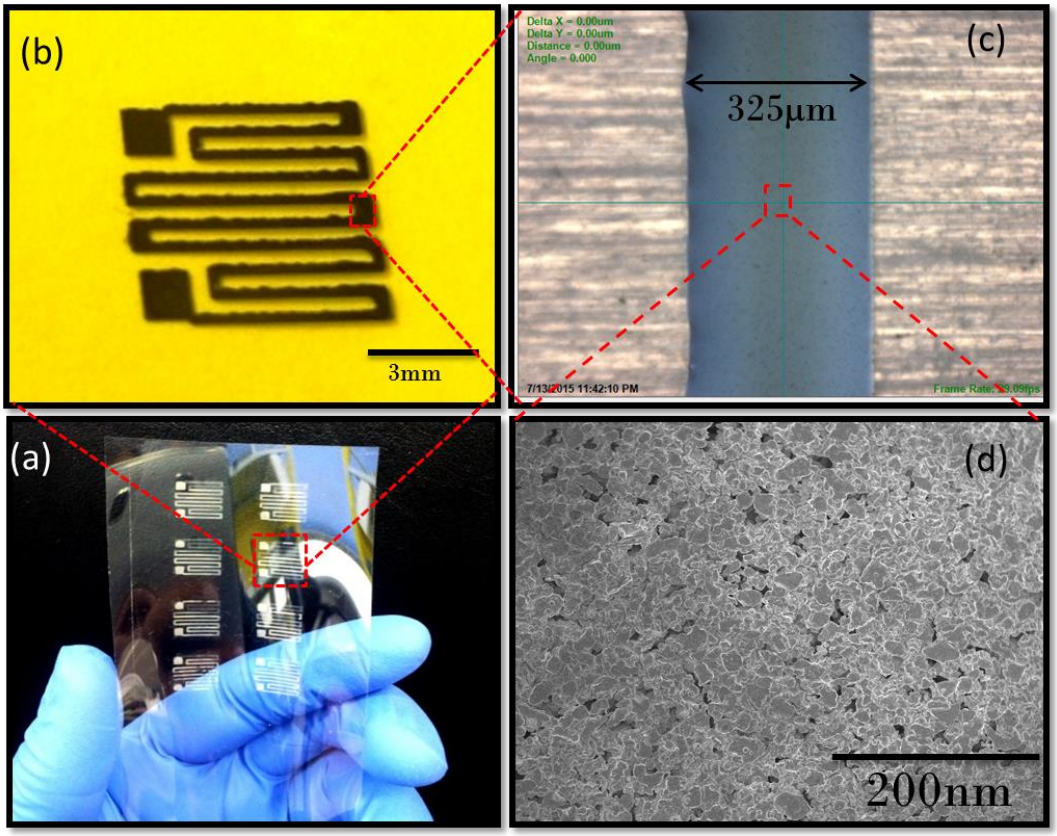

Figure 7.5. Fabricated temperature sensors on a PET substrate through inkjet material printer (b) Zoomed image of the single sensor device (c) Zoomed image of the silver trace (d) SEM image of the silver line.

7.2.4 Bending effect of the temperature sensor

The bending sensing characterization of the proposed sensor was carried out at 25°C and 35% humidity by using a homemade bending machine as shown in **Figure 7.6**a, inset shows the image of

sensor that is under test for the bending sensing. Sensor was bent from 8 mm to 2 mm diameter and the resistance value was recorded, it was observed that the resistance changes along the bending diameter. When the sensor is bent outward, the gap between Ag particles increases and when it is bent inward the gap between Ag particles decrease, the gaps between Ag particles changes the resistivity of the film as shown in Figure 7.6b. This characterization was applied on four different

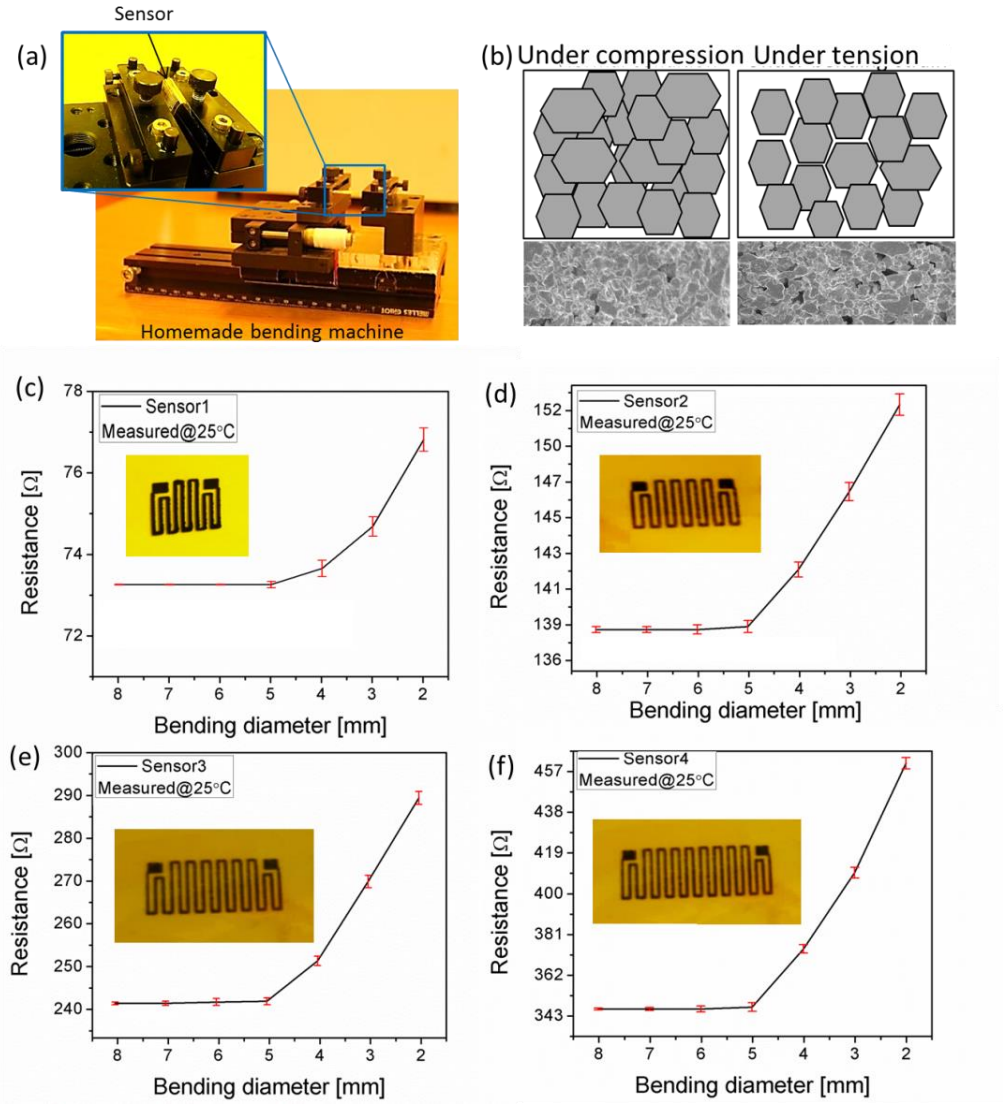

Figure 7.6. Strain sensing characterization of the single meander pattern. (a) Homemade bending machine. (b) Compression and tension phenomenon of the silver film. (c) Strain sensor with total wire length 75mm, (d) 150 mm, (e) 225 mm, and (f) 300mm.

Sensors sensor 1, sensor 2, sensor 3 and sensor 4. It was observed that the sensors showed change in resistance as the bending diameter go below 5 mm. Sensor 1 showed resistance change from 73.5 Ω to 77 Ω as shown in Figure 7.6c. Sensor 2 with total pattern length of 104 mm, showed change in resistance from 139 Ω to 152 Ω as shown in Figure 7.6d. Sensor 3 exhibited change in resistance

from 243 Ω to 290 Ω mm as shown in Figure 7.6e. Sensor 4 having pattern length of 300 mm showed resistance variation from 348 Ω to 457 Ω as shown in Figure 7.6f. As the total length of the sensor increases the sensitivity of the bending also increases. By using single meander pattern, this characterization shows that it is impossible to measure the accurate temperature of the flexible or curved surface because it is acting like a bending sensor rather than a temperature sensor. From this result, this sensor is only suitable for rigid and straight surfaces temperature measurement.

7.2.5 Temperature sensitivity

Resistance temperature detector (RTD) is the contact based temperature sensors that changes its resistance along the change in temperature [18]. The energy of the atoms increases with the rise of temperature in metallic body. Hence, the atoms vibrate and there is a collision of moving electrons in the conduction band. These collusions result in zigzag flow of electrons and increase the resistance. This variation in resistance caused by temperature change is used to detect the temperature. The advantage of RTD type temperature sensors is that, it is small in size, highly accurate, short response time and simple architecture [6]. The temperature coefficient of the sensor (TCR) can be calculated by the following equation [19].

$$TCR = \frac{R_b - R_a}{R_a(\Delta T)} \quad (1)$$

Here, $\Delta T = T_b - T_a$ is change in temperature of the sensor, T_a is the room temperature of the sensor, T_b is the current temperature of the sensor, R_a is initial resistance of the sensor, and R_b is the current resistance at any temperature. The sensitivity of the temperature sensor is calculated by

$$S_{sens} = \frac{\Delta R}{Ra} \quad (2)$$

Here, the S_{sens} is the sensitivity of the temperature sensor, $\Delta R = R_b - R_a$ is change in the resistance of the sensor. The variation in resistance with respect to temperature was observed by using our proposed sensor for different sizes of pattern. For this test, 4 different size sensors were fabricated having length of 75 mm, 150 mm, 225 mm, and 300 mm for sensor 1, sensor 2, sensor 3 and sensor 4, respectively. These sensors were placed on a variable temperature hot plate one by one, terminals of the sensor were attached to the ohmmeter and resistance was measured at 10°C step of temperature. To obtain the change in resistance of the sensor (ΔR) along the increasing temperature, the temperature controlled as a step 10°C from 0°C to 130°C. It was observed that the sensor

resistance has a linear relationship with the temperature as the curve is following a linear path from 0°C until 100 °C, after this point the TCR got changed and the relationship was no more linear. Sensor 2 showed a liner behavior from 0°C until 95°C, and sensor 3 showed a linear region from 0°C until 90°C and sensor4 showed linear region from 0°C until 86°C. These results show a trend between linearity and length of the sensor, as the length increases the linear region decreases accordingly. The TCR was observed 0.00113888 °C-1 by using equation 2. TCR values of 100 measurement iterations for all sensors were used to calculate the sensitivity of each sensor as shown in Figure 7.7.

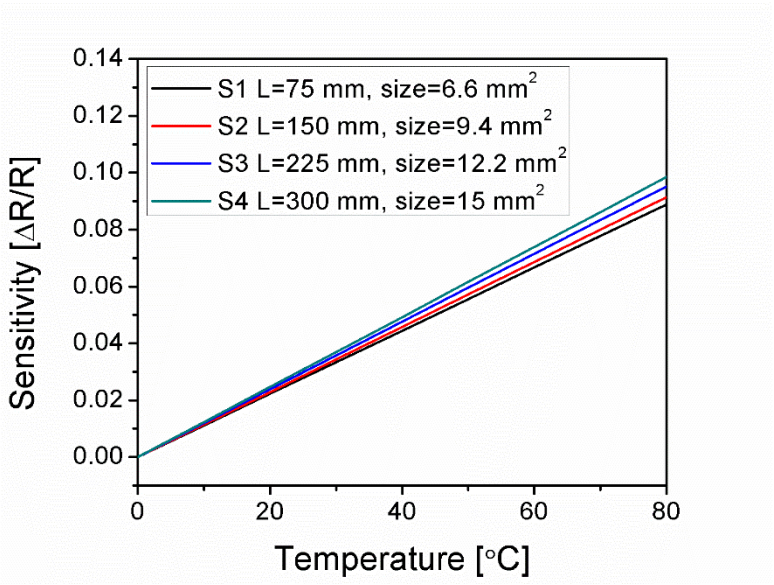

Figure 7.7. Sensitivity vs temperature curve of the sensor 1, sensor 2, sensor 3, and sensor 4 for the temperature span from 0° C to 130 °C.

7.3 Humidity Sensor

Humidity monitoring is an important environmental sensing factor in daily life such as medical, food, and industrial environments [20]. Humidity sensors detect the water content in the air through change in various parameters including resistance, capacitance, surface acoustic waves, and piezo electric [21]-[25]. Especially, resistive and capacitive sensors got a great interest in terms of their low cost, ease of fabrication, and integration in electronic circuits because of direct electrical readout [26]. Among the other parameters of the humidity sensor, its sensitivity is one of the key features. Sensitivity of a humidity sensor is defined as the minimum input of %RH that can create a detectable change in the output. In the case of resistive sensors, it is defined as ΔR/R while for the capacitive sensors it is ΔC/C. Here, R is a resistance at a reference % RH, ΔR is its resistance

variation, C is a capacitance at a reference % RH, and ΔC is its capacitance variation. Capacitive humidity sensors based on polymers are highly sensitive to low and high humidity levels, but they require complex interfacing circuitry. Resistive sensors are good for middle range measurement of humidity level, but they are not sensitive to low humidity levels as their impedance is very high [27]. To increase the sensing range, a conductive material is generally mixed with insulating material such as polyvinylpyrrolidone (PVP)/Polyvinyl alcohol (PVA) composite in which the impedance of the PVP is decreased by the addition of conductive material [20],[26]-[28]. However, the sensitivity of these sensors is still small and the response time is high. Multi wall carbon nanotubes (MWCNTs) and polyamide composite has been used for the humidity sensing however, it offered only a small change in resistance against its full range [29]. Silver nanoparticle and PVA composite based resistive humidity sensor was reported to sense low humidity range from 0% to 60% RH [[30]]. A wide range and fast resistive humidity sensor, based on quaternized polypyrole material has been reported with 10-90% RH sensing range and response time of 40s [31]. Other humidity sensors based piezoresistive phenomena are presented which were fabricated through inkjet printer by utilizing PEDOT:PSS material but these sensors are also limited by sensing range and response time [32].

Apart from polymeric materials, various other materials have been reported for humidity sensors such as metal oxides [33], carbon nanotubes (CNTs) [21],[34], carbon nanowires (CNWs) [35], graphene [22], and G [23]. Among these, the graphene is notable new class of two-dimensional (2D) material with its unique electrical characteristics [36], recently being investigated for deployment in various fields. The graphene is high conductive material and very sensitive to a number of gases (even showing sensitivity against a single molecule change) [37] because of their p-orbital electron, which forms pi-bonds with nearby atoms creating a new structure with high carrier mobility [38]. These pi-bond electrons are very sensitive to change in their immediate environment, making it more promising for biological and chemical sensors. Several resistive graphene-based sensors have been reported to sense the humidity levels. However, due to high conductivity of the graphene, it is very less sensitive to humidity levels, in other words change in resistance to % RH is very low. It makes difficult to detect change in resistance at higher humidity (% RH) levels. To overcome these problems, the sensitivity and sensing range of the humidity sensor could be improved by blending another material with graphene. Apart from this, most of the above reported sensors utilize conventional electronics manufacturing systems based on vacuum technology, which is well precise, controlled and capable of reproducing the exact parameters of

the device. However, this fabrication process is quite complicated, time consuming and requires various steps, control of temperature and pressure, rigid substrates and use of corrosive chemicals [39]. To be utilized in wearable and flexible electronics, printed fabrications to enable low temperature and ambient conditions should be used.

7.3.1 Graphene/methyl-red humidity sensor

In this section, a new inter-digital inkjet printed sensor covered with G and M-R composite material is proposed for the potential wearable electronic applications. The G/M-R composite thin film based humidity sensor has quick response and recovery time of 0.251s and 0.35s respectively under standard temperature and pressure. The proposed sensor is highly sensitive of 96.36% in detectable range from 5% to 95% RH, which has negligible cross sensitivity from other constituents in air due to addition of M-R in the graphene. The interaction of water molecules with the composite of G and M-R is highly detectable as the electrical resistance of the sensor goes down by completing the current paths with water molecules. The proposed sensor is fabricated on a low cost flexible PET substrate with simple inkjet print technology such as Dimatix material inkjet printer (DMP-3000) for silver electrodes and electrohydrodynamic (EHD) for the composite sensing thin film layer, and thereby, is suitable to integrate with wearable electronic devices.

7.3.2 Working principle of the proposed sensor

Humidity changes the electrical resistance of the sensor inversely. The sensing thin film is deposited on the inter-digital electrodes, this kind of electrode is more sensitive as many fingers detects the change in electrical property of the film. The schematic diagram of the proposed humidity sensor is shown in **Figure 7.8**. The terminals of the electrodes are connected to an ohmmeter that reads the resistance of the sensor at various % RH. The phenomena of water vapors interaction with the graphene/methyl-red composite film is shown in the inset of **Figure 7.8** . As the humidity level increases, more water vapors are adsorbed by the surface of the proposed sensor and decrease the resistance. Likewise, when the water vapors are desorbed from the sensor's surface the resistance is increased.

In the steady state, the electrical resistance of a graphene sheet is very low, however its resistance increases since it reacts with oxygen, where oxygen groups capture free electrons. The oxygen

groups engage the free electrons, which are responsible for the conduction of current. Hence, the resistance of the graphene sheet increases in presence of H2O vapors and decreases in the absence of water vapors. This resistance modulation of the graphene sheet makes it attractive candidate for the humidity sensing applications. However, in the proposed sensor, I utilize few layer graphene flakes instead of graphene sheet, its individual layer graphene flakes are not electrically connected with each other. Hence, a film fabricated as few layer graphene flakes has very high resistance.

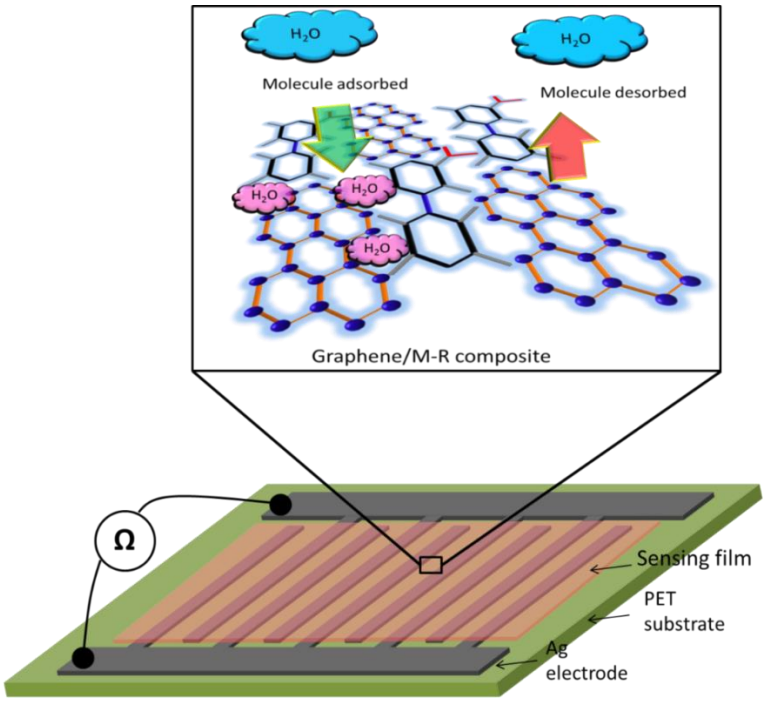

Figure 7.8. Schematic representation of a sensing phenomenon of the proposed humidity sensor, where, water vapors being blown and evaporated onto the surface of the sensing film that changes the electrical resistance of the sensor.

However, the resistance of the graphene film can be decrease if graphene flakes are electrically connected to each other in some way like water vapors absorption. Hence, methyl-red blended with graphene flakes is playing an important role in making electrical connection flake-to-flake, since it binds the flakes together with very high electrical resistance. Therefore, in absence of water vapors the resistance of the sensing film is very high. When water vapors fall on the sensing film, the methyl-red absorb the vapors and decreases its resistance that makes connection between flakes. In this mechanism, the proposed sensor is detecting the humidity levels due to modulation of electrical resistance of the graphene/methyl-red composite film by water vapors. The resistance change of the composite film is collected through the multiple fingers of the inter-digital electrodes to enhance the sensitivity. The proposed sensor is particularly sensitive to the water vapors in the air because of electrostatic forces between water and graphene, as among all air constituent water is the only

molecule that can create a dipole. Many researchers showed the effect of water molecules interaction with the graphene [24],[42].

I have used methyl-red in combination with graphene, which has humidity sensing property. It has very high resistance, however when water vapor falls on it, its resistance decreases. Combination of methyl-red with graphene plays two major roles, first, as the water vapors fall on the surface of the sensor the methyl-red absorbs the water molecule and reduces its resistance, which decreases the overall film resistance. Secondly, methyl-red fills the gaps between graphene flakes, when water vapors fall on the surface, it completes the current paths between graphene flakes and functionalizing it. In our proposed sensor, the sensitivity is high because of the combination of graphene/methyl-red materials, where both materials sense the water content in the air that makes the sensor more sensitive against humidity.

7.3.3 Fabrication of the proposed sensor

7.3.3.1 Inter-digital electrodes

The humidity sensor utilizes inter-digital electrodes as shown in **Figure 7.9**a. I have utilized inter-digital electrodes to improve the sensitivity of the sensor as it contains many electrode fingers to sense cumulatively. Inter digital electrodes are more sensitive as compare to simple two electrodes, because the change in electrical property of the film is collected on all the fingers of the electrode. The length and width of the inter-digital electrodes are 4 mm and 200 µm respectively. The spacing between fingers of inter-digital electrodes was experimentally selected to be 400 µm, resulted in wide range humidity sensing (The detailed explanation describes on Section A in Supplementary Information.). The thickness of the deposited silver pattern in 0.4 µm as cross section view of the sensor layout is shown in **Figure 7.9**b. The design patterns for the interdigital electrodes of the proposed sensor are fabricated through the commercialized Dimatix Material Inkjet Printer (DMP-3000).

The silver nano particle ink was purchased from sigma Aldrich South Korea, and was filled (3 ml) into the cartridge containing 16 nozzles. The commercial 100-micron thick PET film (purchase from sigma Aldrich) was used as a substrate for the proposed sensor. Prior to printing on the substrate first, we cleaned it with ethanol baths at ambient conditions and then rinsing with water and dry it at 100 °C for 2 min. We printed the sensor after cleaning procedure but silver nanoparticles were randomly spread over the surface. To resolve this issue, the PET substrate was

UV treated for 30 s. This process was carried out to make the surface rough to avoid the random spread of silver nanoparticles over the surface. The UV tread PET was placed onto the plate of material inkjet printer for printing the proposed sensor. The proposed sensor was fabricated by utilizing a single nozzle to ensure high accuracy of ink deposition on the substrate. The humidity sensor's electrode is fabricated on PET substrate as shown in **Figure 7.9**c. The zoomed image of the printed sensor is shown in **Figure 7.9**d with 200 µm track width, which shows clear deposition (without spread) of silver ink over the substrate.

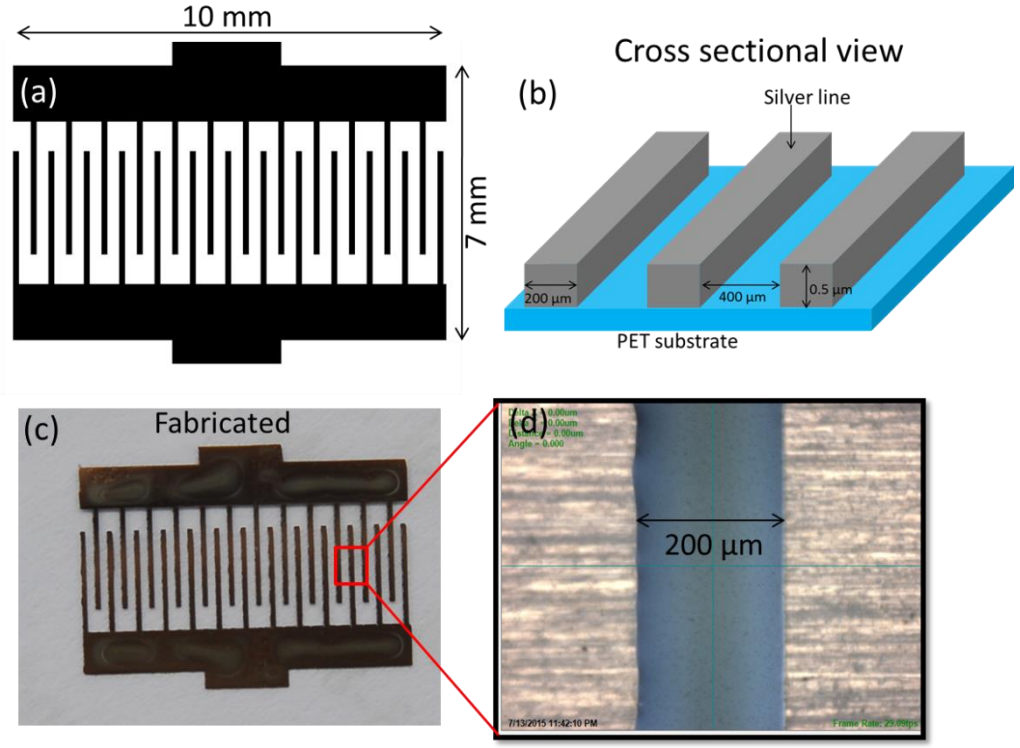

Figure 7.9. (a) Design layout of interdigitated electrodes without graphene/methyl-red compsoite. (b) Cross section vew of inter-digital electrodes with track width and height of 200 µm and 0.5 µm, respectively and the spacing between electrodes isof 400 µm. (c) The inkjet printed sensor with sliver ink. (d) Zoom image of the area sef off by a red solid line with 200 µm track width of silver electrode.

7.3.3.2 Sensing layer material

The sensing layer is the most important component of the humidity sensor. The electrical resistance of the sensing layer changes as the water vapors blown on it, this change in resistance is easily collected on the fingers of inter-digital electrodes. For manufacture the sensing layer, two materials graphene and methyl red were synthesized. Graphite powder and N-methyl-pyrrolidone (NMP) solvent were purchased from Sigma Aldrich. The graphite powder (0.05 g) was dispersed in NMP (10 ml) solvent. The solution was then bath sonicated for 30 min at room temperature. After bath sonication of the ink, large un-exfoliated graphite flakes were removed by vacuum filtration. The

ink was further purified with centrifugation. It was carried out for 30 minutes at 4000 rpm and supernatant was separated from sediment. The viscosity of the ink was measured to be 23.6 mPa by using Viscometer VM-10A system. The surface tension of the ink was measured around 65~68 mN/m by using Surface-electro-optics (SEO)'s contact angle analyzer. The electrical conductivity of the ink was 28.7 µS/cm measured by using conductivity meter (Cond6+ meter). Methyl red powder and Dimethylformamide (DMF) was purchased from Sigma Aldrich. 10-weight percent methyl red was prepared in DMF by bath sonication for 2 h at 30 °C, because at lower temperature (less than 15 °C) the methyl red in DMF makes gel. The graphene and methyl-red inks were mixed with optimum 2:1 ratio. This ratio was obtained experimentally to achieve RH range from 5% to 95% as well as high sensitivity. The mixed ink was placed on a bath sonicator at ambient conditions for 1h to make uniform dispersion solution of graphene flakes and methyl-red.

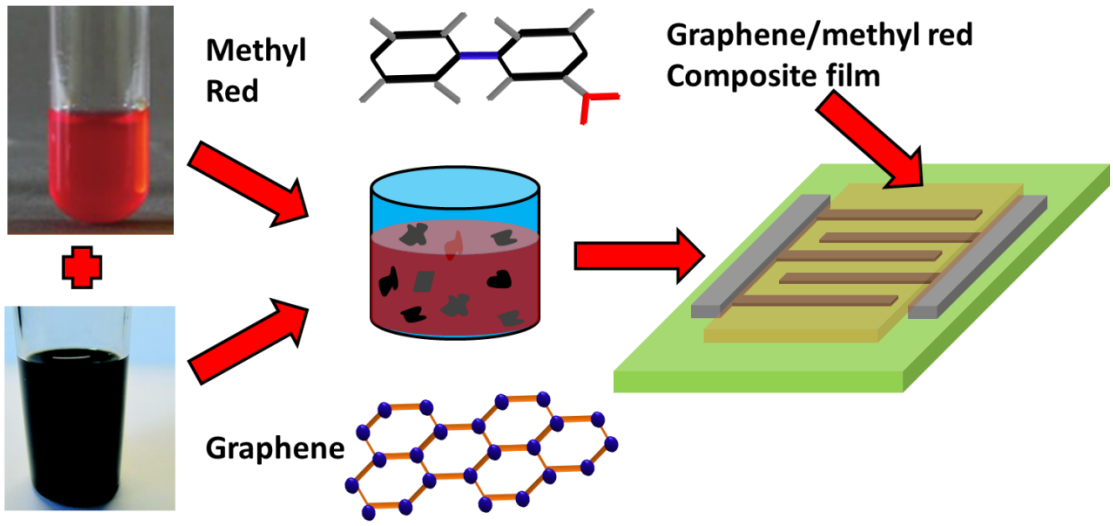

Figure 7.10. Schematic representation of the graphen/methyl-red composite based humidity sensor.

To fabricate the sensing layer, Figure 7.10 shows the chemical structure of graphene and methyl-red. Using this graphene/methyl-red composite material, the thin film of sensing layer was deposited over the silver printed interdigital electrodes by using electrohydrodynamic (EHD) technique. Substrate was placed on the moving stage, high voltage was applied to the nozzle through the high voltage source and ground to the substrate holder. During the thin film deposition, the EHD parameters were tuned such as, applied voltage 4.5 kV, ink flow rate 150 µl/h, nozzle inner diameter 110 µm, standoff distance 15 mm and substrate moving velocity was 3 mm/s with these parameters almost 300 nm thin film was deposited on the inter-digital electrodes (The detailed explanation describes on Section A in Supplementary Information). More details about the EHD can be found

in our previous work [[40],[41]]. After successful fabrication of the sensor, it was cured at 130 °C for 2 h. Connecting wires were attached to the terminal electrodes of the sensor through silver epoxy for the direct electrical readout, it was again cured at 80 °C for 15 min.

7.3.4 Morphology characterization

NV-2000(Universal) non-contact surface profiler with Nano level accuracy was used for surface morphology measurement in phase shifting interferometry (PSI) mode. In Figure 7.11a, 3D profile of Ag electrodes is shown covering two fingers, and it can be seen that the electrodes deposited through the commercialized DMP-3000 inkjet printer are uniform with thickness of almost 400 nm. Figure 7.11b shows the 3D profile of graphene/methyl red composite film. It can be seen that the composite film is uniform over the surface of the electrodes and substrate. The scanning electron microscopy (SEM) images were obtained by using Jeol JSM-7600F. Figure 7.11c shows the composite film SEM image at 10 µm scale, where the film can be seen uniformly deposited, the Figure 7.11d shows the composite film at 1 µm scale to show the zoomed view of the film.

The fabricated composite film was further evaluated by Raman spectroscopy as shown in Figure 7.12a. Peaks were observed at 1355 and 1596 cm-1 indicates the presence of the D and G bands of the graphene. The optical properties of the developed graphene/methyl-red composite thin film were measured with UV-IR spectrophotometer (Hewlett Packard HP-8453). As the measured transmittance of the composite film is shown in Figure 7.12b, it shows that the composite graphene/methyl-red thin film is transparent up to 80% at 400 nm and it approaches to 90% above 550 nm wavelength of the visible light spectrum. Since the sensing film is transparent and do not absorb light in the entire visible spectrum, it is not affected by visible light when used in such applications where the device is exposed to intensive light. In other words, if the film is absorbing some of the light spectrum, it will gain energy and the resistance could be changed due to light as well. The film transparency ensures its application in transparent application in combination with transparent electrodes.

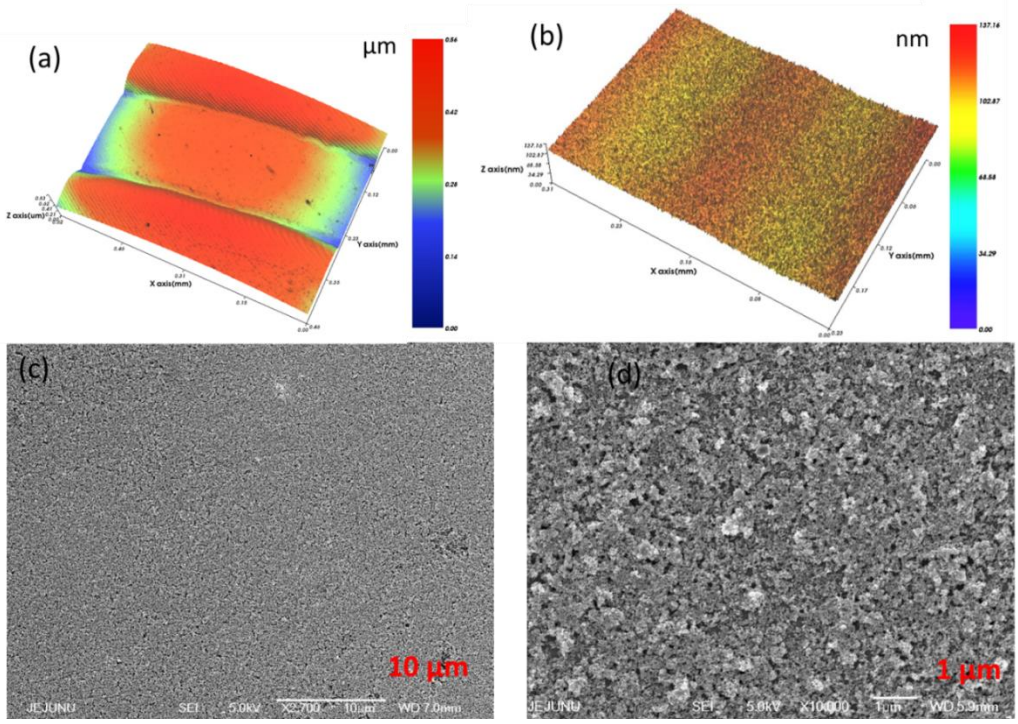

Figure 7.11. (a) 3D nano surface profile of the silver electrode with 0.5 µm height. (b) The graphen/methy-red composite Sensing layer surface profile with 300 nm height. (c) Scanning electron microscopy (SEM) image (10µm) of the graphene/methyl-red composite sensing layer. (d) The magnified image (1µm) of graphene/methyl red compsite.

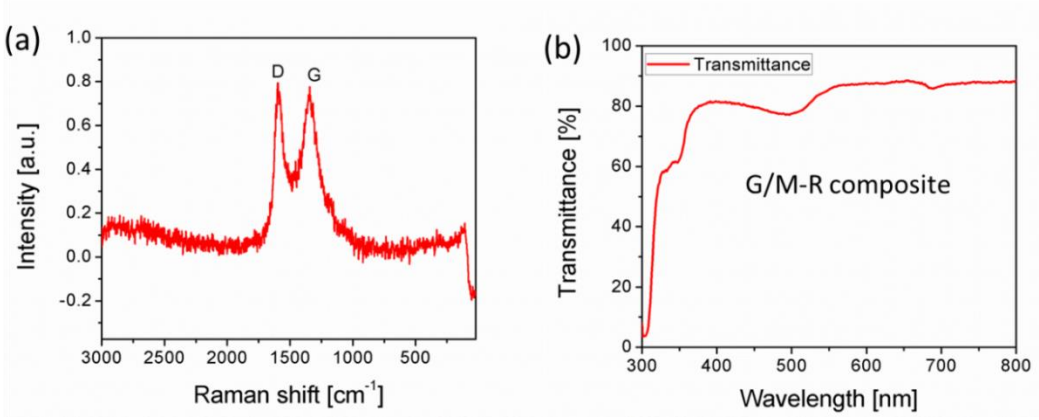

Figure 7.12. (a) Raman Spectrum of the sensing layer with two peaks D and G indicating the presence of the graphene in the composite film. (b) FTIR spectrum of the sensing layer showing the transmittance of light through the mentioned composite film.

7.3.5 Characterization

The proposed sensor is characterized for its electrical, optical, surface morphology and chemical characteristics.

7.3.5.1 Measurement set up

As the humidity measurement, setup block diagram shown in **Figure 7.13**a, it is consisted of a homemade airtight chamber, LCR meter, humidifier, nitrogen gas, reference humidity sensor, data acquisition (DAQ) circuit and oscilloscope. The physical humidity measurement setup is shown in **Figure 7.13**b, where all components are shown with their nametags. The humidity chamber covered the full range of relative humidity from 0% to 100%. Both the proposed and the reference commercialized digital humidity sensor (HTU21D) were placed inside the homemade humidity chamber. The reference sensor has resolution of 0.04% RH, accuracy of ±2% RH and response time is less than 5s. The nitrogen (N_2) was used to decrease the relative humidity level from 40% to 0%. The injection rate of N_2 into the chamber was controlled by external valve. The humidity in the chamber was increased from 0% to 100% by increasing the water vapors in the chamber at constant pressure. The commercialized humidifier was used to increase humidity inside the chamber by increasing the water vapors through a pipe. The humidity level inside the airtight customized humidity chamber was controlled by controlling the flow rate of N_2 and water vapors of humidifier. The experiments were carried out on three different humidity sensors including sensor 1 (methyl red), sensor 2 (graphene) and sensor 3 (composite). The device under test (DUT) was placed inside the airtight chamber, and leads were connected to the LCR meter. The humidity of the chamber was reduced to 0% by injecting the N_2 gas. Sensor 1 was placed inside the chamber and leads were connected to the LCR meter. First, the humidity was decreased to 0% through N_2 gas injection.

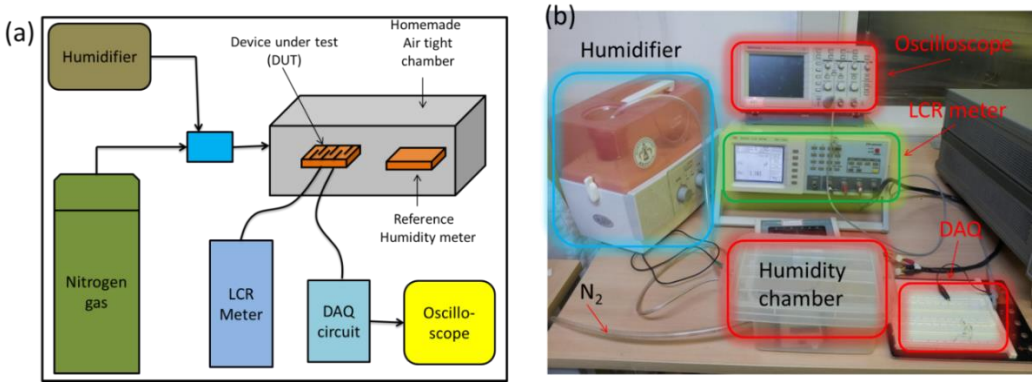

Figure 7.13. (a) Block diagram of humidity testing and data acquisiton setup. (b) Characterization setup for humidity monitioring.

7.3.5.2 Electrical characterization

To characterize the sensor against the humidity an experiment was conducted in which humidifier was used to increase the humidity of the chamber from 0% to 100% RH with increment step of 10% RH. Sensor 1 showed resistance change from 36 kΩ to 23 kΩ against RH from 0% to 100% as shown in **Figure 7.14**a. The prominent resistance variation of 13 kΩ was observed at humidity levels 5% to 70%, whereas after 70% the sensor was saturated against the humidity. Sensor 2 based on pure methyl-red was placed inside the chamber, resistance change was recorded against the RH for the 0% to 100% range. It was observed that the resistance prominently changed from 45 MΩ to 14 MΩ against humidity level of 30% to 90% as shown in **Figure 7.14**b.

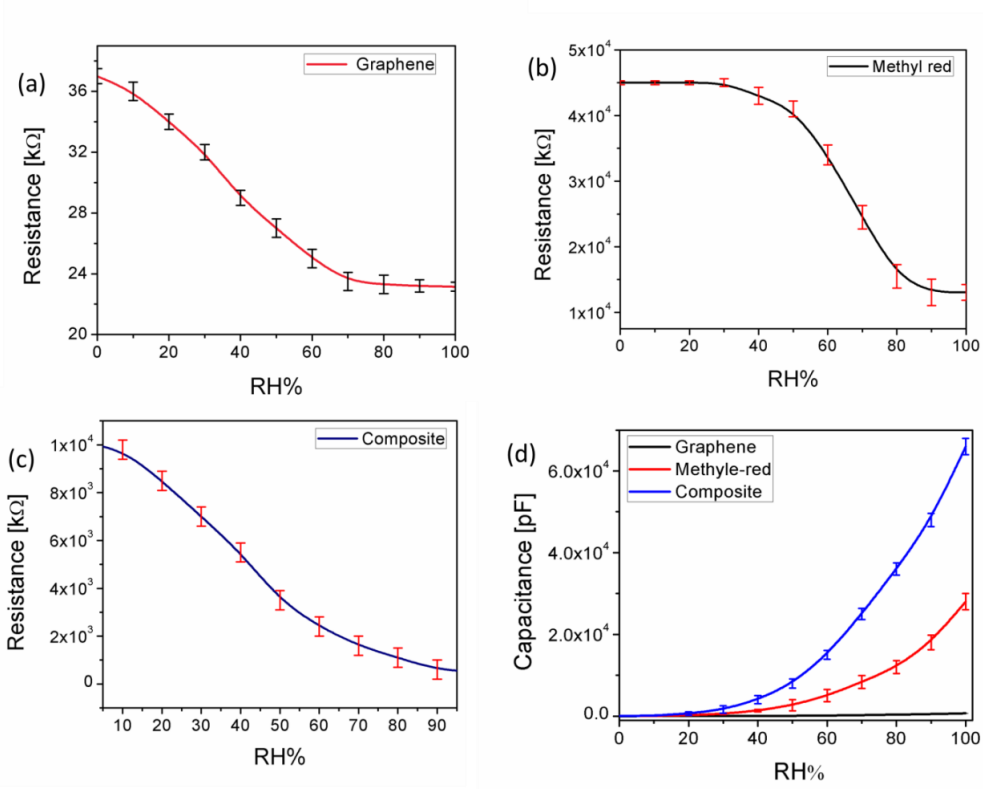

Figure 7.14. (a) Resistance versus relative humidity (% RH) in the graphene film. (b) Resistance versus relative humidity (% RH) in the methyle-red film. (c) Composite graphene/methyl-red based humidity sensor. (d) Capcitance versus relative humidity (% RH) characteristics curves of the graphene/methyl-red composite, methyle-red only, and graphene only based humidity sensors measured in the humidity chamber at 1kHz frequency.

Sensor 3 was placed inside the chamber and N2 was applied. Firstly, the electrical resistance of the sensor significantly changed from 6.5 MΩ to 11 MΩ since the concentration of N2 increased inside the chamber and nitrogen gas flowed across the surface of the sensor. Then by increasing the humidity from 0% to 100% inside the chamber, the sensor showed resistance variation from 11 MΩ down to 0.4 MΩ against relative humidity 5% to 95% as shown in **Figure 7.14**c. This change in

resistance occurred due to the reduction of concentration of water vapors over the surface of graphene/methyl-red thin film. The cross sensitivity against N2 gas was evaluated by injecting a substantial amount of nitrogen gas into chamber to circulate over the surface of the sensor which was already at 0% RH. It was observed that the electrical resistance remained at almost 11 MΩ. It can be seen that the change in resistance at lower than 5% RH and higher than 95% RH is very low. The measured resistance showed a sensitivity of 96.36%. During the experiment, reference humidity meter was used to record the humidity value against the resistance of the DUT. These sensors were characterized for their capacitance change against humidity as shown in **Figure 7.14**d. By utilizing digital L.C.R meter EDC-1631 at room temperature, capacitance measurements were done for the RH range from 0 to 100%. Sensor was placed inside the airtight box and leads of the L.C.R meter were connected with the sensor, where the humidity was controlled through humidifier and N2 gas. Capacitance of the sensor was measured at 1 kHz frequency and %RH was increased from 0% to 100% with increment step of 10%. All sensors showed good detectability against humidity levels almost from 0% to 100% RH for 50 endurance cycles, and the capacitance values against %RH were measured with a small variation for each measuring cycle indicated by the error bars as shown in **Figure 7.14**d. However, the composite sensor showed change in capacitance from 2.3 pF to 66 nF, which is the high change in capacitance and the measured sensitivity of 2869500%. Graphene based sensor showed the least change in capacitance from 0.54 pF to 147 pF, whereas the methyl red based sensor showed capacitance change from 3 pF to 23.7 nF.

7.3.5.3 Open air test

For the direct electrical read out a DAQ circuit was prepared by connecting a fixed resistor (Rfixed) of 1.8 MΩ in series with proposed humidity sensor (RH). DC voltage of 5 V was applied across the series circuit and output was taken across the humidity sensor at Vsens terminal as shown in Figure 7.15a. The resistance of the humidity sensor was changed along the humidity levels, the sensor electrical resistance went up when humidity level increased and resistance went down when humidity level decreased. Therefore, the voltage drop across the RH also varies accordingly. To measure the variation in voltage at the output of the DAQ circuit, an oscilloscope was connected across the RH. The sensor was took out of the chamber and it was exposed to the humidity (relative humidity of approximately 100%) of exhaled human breath, the sensor responded quickly against humidity of human breath as shown in Figure 7.15b.

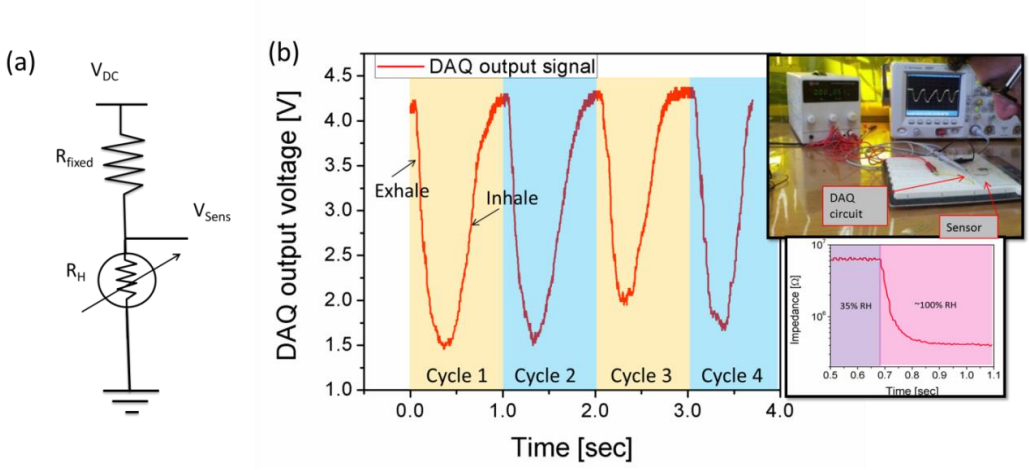

Figure 7.15. (a) Data Aquizition circuit, R_{fixed} is 1.8 MΩ resistor and R_H is the the proposed sensor connected in series for a voltage divider nettwork, where, R_H varies against humidity levels. (b) Output voltage signal of the data acquistion circuit, when the proposed humidity sensor exposed to exhaling and inhaling of human breath. Upper Inset shows the setup and respone against human breath. Lower inset shows the impdeance response of the proposed humidity sensor when suddenly changed the humidity level from 35% RH to 100% RH over the humidity sensor surface.

The experimental setup for the human breath is shown in the upper inset, where sensor is connected to the oscilloscope through the DAQ circuit in open air at ambient condition. In this experiment, the electrical resistance of the sensor decreased while exhaling (with 100% relative humidity) in a close proximity of 10-15 cm to the sensor. While, the device resistance increased during inhaling breath, this process was carried out for several times and the same phenomena happens as shown in the lower inset of **Figure 7.15**b.

7.3.5.4 Sensitivity

The sensitivity of the sensor against humidity levels was recoded as shown in **Figure 7.16**a, which indicates linear change in resistance against humidity. The response time and the recovery time against humidification and dehumidification as shown in **Figure 7.16**b. Here, 6 MΩ (at 35% RH) and 0.4 MΩ (at 100% RH) corresponds to 1 and 0 respectively on the y-axis. On the normalization of y-axis, we calculated the normalized values by using $(R_{sen} - R_{min})/(R_{max} - R_{min})$, where, R_{max} = 6 MΩ at 35% RH, R_{min} = 0.4 MΩ at 100% RH, and R_{sen} is a sensing resistance at a present %RH. The response time and the recovery time were measured to be 0.251s and 0.35s respectively, during human breath test. These results are consistent with our previous results and in line with our expectations from the previous results that we have obtained from humidity chamber.

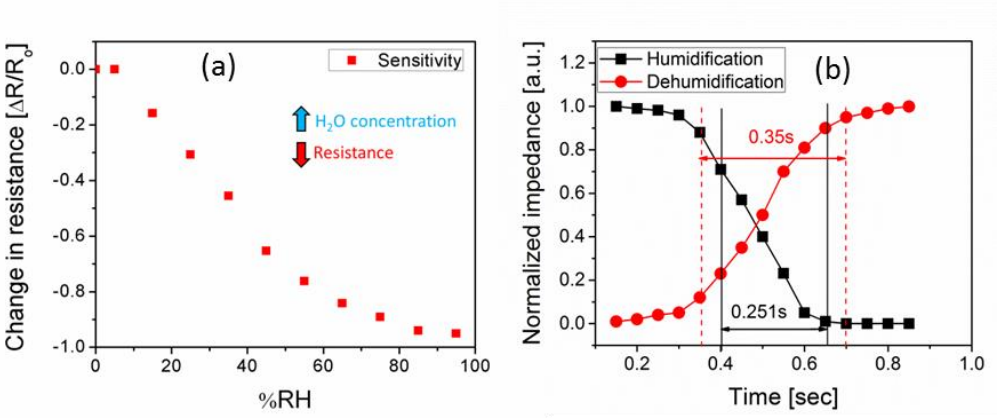

Figure 7.16. (a) Change in resistance versus percent relative humidity level. (b) Response and recovery time curves of humidity sensor for humdification (35% - 100% RH) and dehumidication (100% to 35% RH).

7.3.5.5 Crosscheck and hysteresis characteristics

The proposed humidity sensor was also crosschecked with the commercialized humidity digital sensor HTU21D and response was recorded in the form of resistance variations over the time against humidity levels as shown in **Figure 7.17**a. The electrical resistance of the proposed sensor decreased accordingly to the measured humidity levels. During this experiment, the humidity increment step was kept very low to check the response of the proposed sensor at very low humidity change. It was observed that the proposed sensor showed change in resistance over the variation of humidity at each increment step. The proposed humidity sensor quickly responds to a small change in humidity level due to its high sensitivity as the resistance varies from 11 M Ω to 0.4 MΩ, which makes the sensor more attractive to be utilized in high-resolution humidity measurement applications. The commercialized sensor covers full humidity range while the presented sensor has range of 5 to 95% RH. In order to compare the findings of graphene/methyl-red based humidity sensor with the commercialized and other reported sensors. Humidity sensors carry some memory of conditions experienced in recent past called hysteresis characteristics [[46]]. If sensor is stored at lower humid environment it carry some negative offset while, sensor with high humid history carry some positive offset in terms of its resistance and capacitance values. The proposed sensor was analyzed for the hysteresis characteristics as shown in **Figure 7.17**b. For this characteristic, the sensor was stored at 0% RH, and then the humidity level was increased from 5% to 95%, and back from 95% to 5% RH with 10% step. The resistance of the sensor was recorded against each humidity level during

adsorption and desorption cycles. It was observed that, the resistance values during desorption cycle lower RH (5~20%) and upper (75~95%) values are overlapping which shows no hysteresis, whereas in the middle from 20 to 75% RH the curve follows different resistance path with positive offset showed a small hysteresis effect.

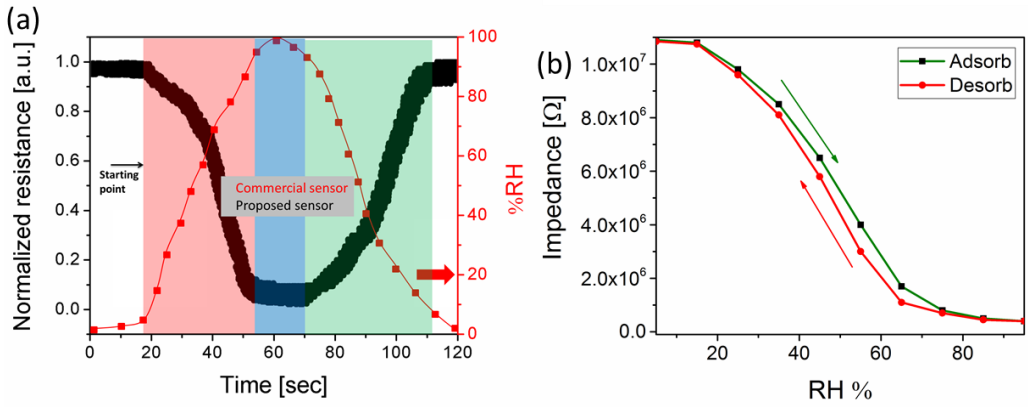

Figure 7.17. (a) Normalized resistance versus time response curves in conjunction with % RH of the proposed and commericial humidity sensor. (b) Hysteresis curve of the proposed sensor, adsorption and desorption cycle for the RH range 5~95%.

7.3.5.6 Comparison

Table 4.2 shows the comparison on the basis different characteristics such as response time, recovery time, range and the sensitivity of the sensors. From the Table I, it can be observed that the response time and recovery time is less than Borini [[23]] as it has 0.03s response and recovery time while our proposed sensor has 0.251s and 0.35s response and recovery time respectively. However, the detectable range of our proposed sensor is high as compared to Borini [[23]] work. The range of our proposed sensor is equal to Buvailo humidity senor [[24]] but the response time, recovery time and sensitivity of our proposed sensor is better. When we compare it with other resistive based humidity sensors, our proposed sensor is better in term of range and sensitivity. While the response and recovery time is better than other reported humidity sensors except Borini's work. From the overall comparison as shown in Table 4.2, our proposed graphene/methyl-red based sensor is better as compared to the reported sensors in term of sensitivity as it has resistive sensitivity of 96.36% and capacitive sensitivity of 2869500%. The sensitivity of the sensor was calculated by using formula for resistance given in equation 1 and for capacitance given in equation 2.

$$S_R = \frac{\Delta R}{R_0} \times 100 \quad (1)$$

$$S_C = \frac{\Delta C}{C} \times 100 \quad (2)$$

Table 4.2. Comparison of different reported humidity sensors with the proposed grahphene/methy-red based humidity sensors

Literature	Sensing Material	Sensing phenomena	Measured %RH Range	Response Time(s)	Recovery Time(s)	Sensitivity (%)
Yao [6]	Graphene Oxide	Piezoelectric	10-98	19	10	79.3 $(\Delta V/\%RH)$
Smith [3]	Graphene	Resistive	1-96	0.6	0.4	0.31$(\Delta R/R\%\Delta RH)$
Bi [7]	Graphene Oxide	Capacitive	15-95	10.5	41	37757.14 $(\Delta C/\%RH)$
Borini [4]	Graphene Oxide	Resistive	30-80	0.03	0.03	-
Hwang [8]	Graphene Oxide/ PVA	Piezoelectric	40-100	-	-	-
Ghosh [9]	Graphene	Resistive	4-84	180	180	65 $(\Delta R/R)$
Chen [10]	Graphene	Resistive	35-98	-	-	18.1 $(\Delta I/I)$
Kuang [2]	SnO_2	Resistive	5-85	120-170	20-60	3200$(\Delta I/I)$
Lin [11]	PANi nanofiber	SAW	20-90	1	2	75 (kHz/%RH)
Buvailo [5]	PVA & PVP	SAW	5-95	1.5	2.5	-
HIH-4000 (commercial)	Polymer	Capacitive	1-100	6	20	-
Presented Work	**Graphene/ methyl-red**	**Resistive**	**5-95**	**0.251**	**0.35**	**96.36**$(\Delta R/R)$
Presented Work	**Graphene/ methyl-red**	**Capacitive**	**5-95**	-	-	**2869500** $(\Delta C/C)$

In equation 1, S_R defines the percent change in the electrical resistance of the graphene/methy-red based sensor with respect to change in relative humidity. Here, ΔR shows change in resistance and R_0 is the resistance at 5% RH. In equation 2, S_C is capacitive sensitivity, ΔC is change in capacitance of the sensor, C is capacitance at 5% HR. From the Table 4.2, it can be observed that the response time and recovery time is high as compared to the work presented by [23] while, the sensitivity and the measurement range is high as compared to all the works presented in literature [21]-[23]. The

graphene-based sensors have resistance variation from few hundred ohms to around 1 KΩ because the graphene layer has less defects in the graphene sheet. While, the graphene oxide (GO) based sensors have high variation from 1 MΩ to 10 MΩ because GO has high degree of bond dangling which contributes to high change in electrical resistance. The graphene and graphene oxide based sensor previously reported are most viable for humidity sensing, here in this work the graphene/methyl-red based resistive sensor has been investigated for humidity, which performed well as compared to other humidity sensors. Other main advantage of the reported sensor over previously reported sensors is fabrication process, which is simple, controlled and all-printed.

7.4 Photo sensors

Among organic electronic devices, many photo sensors [47] are also extensively researched by using different materials carrying photoconductive property [48]. Most of them are active sensors based on phototransistor and photodiode [49] and some are integrated with resonant circuits [50]. Various materials those having photo conductive property has been also reported to fabricate a photo detector [48]. Especially, graphene (a 2D material) is emerging material, which is considered the replacement of silicon in near future [51]. It is extensively researched to improve photo detectors [52]. Photoconductive material Perylene has been widely applied in various optical devices due to excellent photo physical properties of high absorption coefficient and high fluorescence quantum yield, charge transfer properties, as well as outstanding chemical, thermal and photochemical stability [53]. By attaching any other material with it, the property of attaching material can be changed in both cases, optically and electrically [54]. Perylene has been researched in phototransistors [55], solar cells [56], and it is researched for its derivatives to achieve optical and electrical enhancement [57]. Perylene has very high resistivity thus when it is used in passive devices, the resistance is very high which cannot be interface with external electronic circuitry. Perylene have versatile properties which can be achieve by synthesizing it or blending with other material that can enhance its property either optically or electrically [59].

7.4.1 Flexible Photo Sensor

7.4.1.1 Fabrication

Graphene platelets from Cheap Tubes (less than 4 layers and surface area greater than 750m2/g), and dichloromethane solvent and perylene powder assay 99.5% from Sigma Aldrich are used. The graphene platelets are dispersed in dichloromethane solvent by bath sonication 24 h and centrifugation for 4 h. The viscosity of the graphene dispersion is measured to be 15.8 mPa by using magnetically stirred for 24 h. The prepared ink is filtered with 5 µm filter to remove undispersed particles and then bath sonicated for 30 min prior to use.

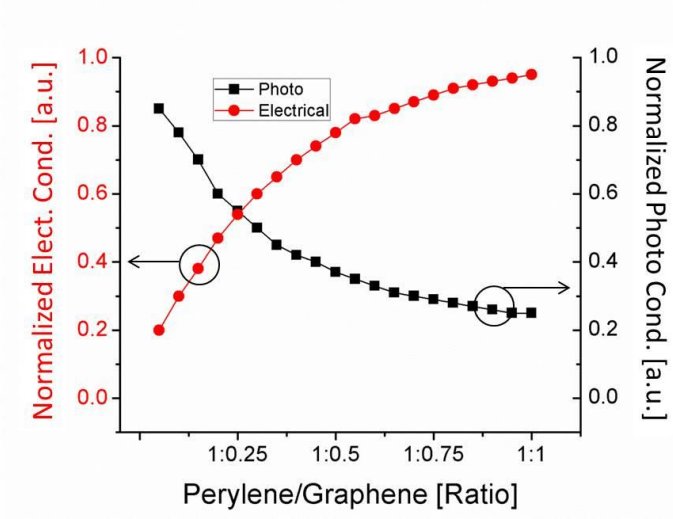

Figure 7.18. Optical and electrical conductivity of the material along Ink mixing ratio.

Viscometer VM-10A system. The surface tension of the dispersion is measured to be 54~57 mN/m. Surface-electro-optics (SEO)'s contact angle analyzer is used for the surface tension measurements. The electrical conductivity of graphene dispersion is 12.2 µS/cm measured by using conductivity meter (Cond6 + meter). Perylene powder of 0.15 g is dispersed in 10 ml dichloromethane and

These two materials were prepared separately and then mixed with various ratios to achieve optimum results experimentally. As a rule of thumb, we found that 1:1/4 is optimal mixing ratio. The electrical conductance increases along the ratio of graphene in the perylene ink but the photo conductance decreases as this relationship is summarized in Figure 7.18. The said mixing ratio of perylene/graphene inks is optimum in term of electrical and photo conductance to achieve light sensing sensitivity and electrical conductance. Ink for silver electrodes is prepared as: Ag nano particle paste sigma Aldrich 50%wt is diluted in 10 ml ethylene glycol solvent and mixed for 1 hour on magnetic stirrer and then 20 min bath sonication. Device was fabricated with EHD system as the

layout diagram is shown in Figure 7.19a. schematic diagram of the device is shown in Figure 7.19b along the terminal resistance, change in resistance between two fingers is indicated by delta R. Fabricated device is shown in Figure 7.19c.

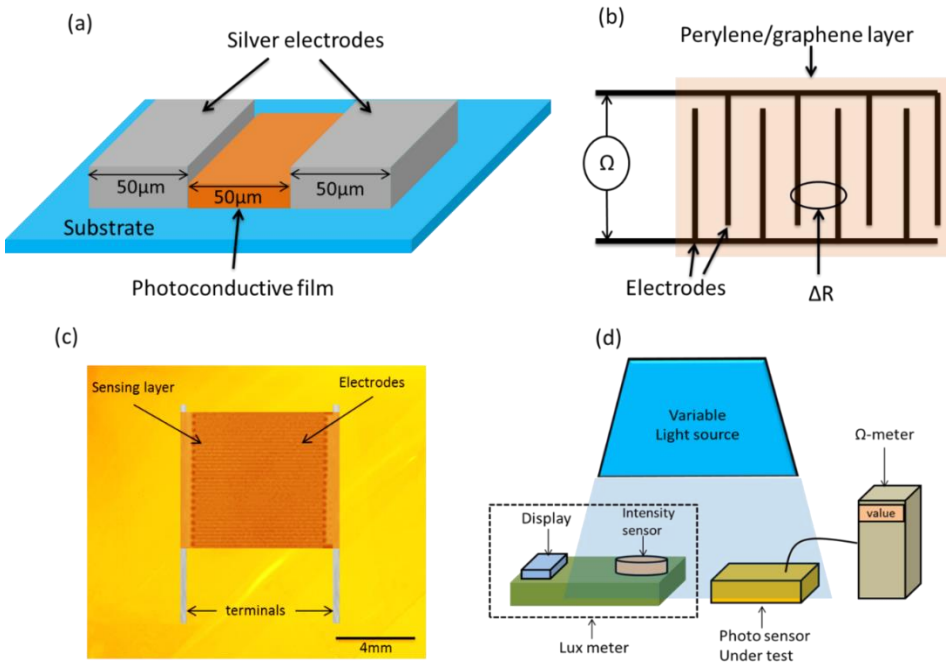

Figure 7.19. (a) Layout diagram of the photo sensor with two electrodes (50µm space) and photoconductive film between them, (b) multiple electrodes diagram to show the cumulative change in resistance at terminals of the sensor, where ΔR is the change in resistance between two electrodes due to the incident light, (c) fabricated photo sensor device on PET substrate, (d) photo detector characterization set up diagram for reading the terminal resistance against varying light intensity.

7.4.1.2 Electrical Characteristics

Perylene/graphene composite based photo sensor is characterized for its current-voltage (I-V) characteristics by using Agilent B1500A Semiconductor Device Analyzer. Photo sensor was placed on substrate holder inside the probes station and probes were connected with its terminal. The sensor's resistance was measured inside a black box, the resistance was recorded about 78 GΩ in dark. After this an LED light source with variable light intensity was used with a lux meter near the photo sensor to detect the light intensity as the diagram shown in Figure 7.19d. The resistance of photo detector was observed from 78 GΩ to 48 GΩ for the light intensity variation from dark to 150 lux as shown in Figure 7.20b. Resistance variation was characterized by measuring the resistance of device along the light intensity with 50 lux increment step. Initially the high resistance

variation was observed from 0 lux to 150 lux and then the resistance variation was observed to be reduced at 300 lux and the resistance of the sensor at 400 lux became constant as shown in Figure 7.20b. This result shows that the sensor can sense light intensity maximum of 400 lux. The proposed device also exhibited its electrical properties while bending it mechanically.

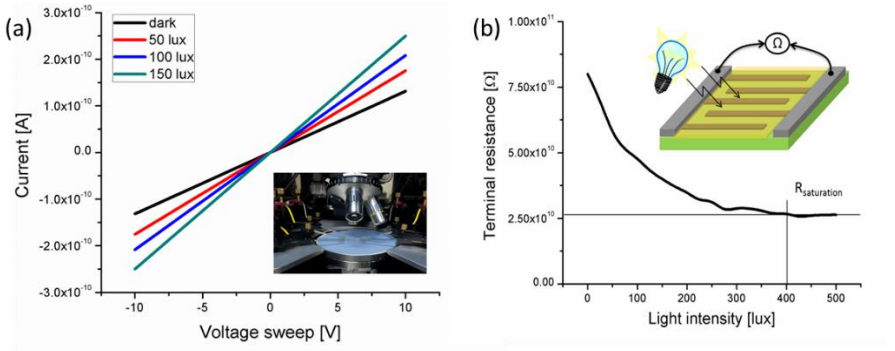

Figure 7.20. Electrical characteristics of the sensor against (a) fixed light intensity, (b) Variable light intensity.

7.4.1.3 Mechanical characteristics

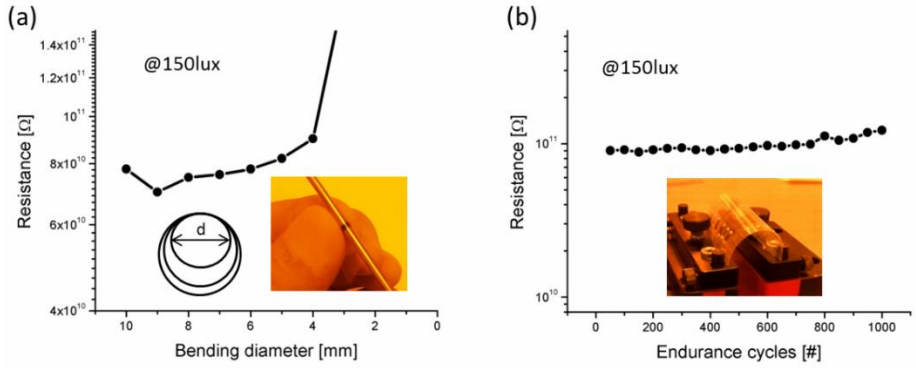

Figure 7.21. (a) Bending analysis of the photo sensor device, (a) bending the device at metallic rod (10~0 mm) diameter, (b) endurance cycle analysis of the fabricated device bending 1000 times at 4mm.

To characterize the device for maximum bendability, it was bent over different rods having diameter from 10mm~2mm as shown in Figure 7.21a. The device showed normal behavior until 4 mm and open circuited behavior at 3mm diameter rod, hence minimum bending diameter is 4 mm for the proposed device. Reliability test of the device was also carried out by bending the device at 4mm diameter rod for 1000 times. The device showed a stable behavior with negligible change in its resistance throughout the test as shown in Figure 7.21b.

7.5 Stretchable Photo Sensor

In this section, a stretchable photo sensor fabricated on a PDMS substrate having uniform micro ridges is presented. The device construction is that, a perylene/graphene composite thin is sandwiched between the ITO bottom and top electrodes through electro-hydrodynamic (EHD) system which is cost effective, environmentally friendly, and non-vacuum e-printing technology . The proposed stretchable photo sensor is profound to blue and ultra violet (UV) light. The resistance of the device is inversely changing with light intensity in the range of 87~108 MΩ. The device showed negligible change in behavior at strain range from 0~25%, and maximum stretchability of 50% with reasonable change in resistance. The device is fully flexible and stretchable tested for 1000 endurance cycles.

7.5.1 Stretchable substrate

Dow Corning's Sylgard 184 elastromer kit, containing the PDMS base and the curing agent are used. A PDMS composite of the base and curing agent at 10:1 by weight and whisked thoroughly for 10 min to make sure that mold is uniformly cross-linked. After proper mixing, the PDMS solution contained air bubbles in it, which has removed by degassing for 30 min through a vacuum pump. The PDMS substrates with uniform ridges were prepared by casting the PDMS solution against ridged plastic homemade die. Die was prepared by producing grooves on plastic substrate though filing. The PDMS castings were annealed inside a furnace at a temperature of 150 °C for 60 min. The PDMS substrates were cut into dimensions of 2.5 cm by 5 mm and an approximate thickness of 1 mm as shown in Figure 7.22.

7.5.2 Device fabrication

Stretchable sensor device was fabricated through EHD system as discussed in chapter 1. During the EHD operation, control parameters of the EHD system for the stable cone jet mode are given in Figure 7.22.The fabrication procedure of the device was completed in three steps. In the 1st step, the bottom electrode of ITO was deposited on the PDMS substrate. In the 2nd step, graphene/perylene active layer was deposited, and in the 3rd step, ITO top electrode was deposited, as the layout diagram is shown in Figure 7.23a.

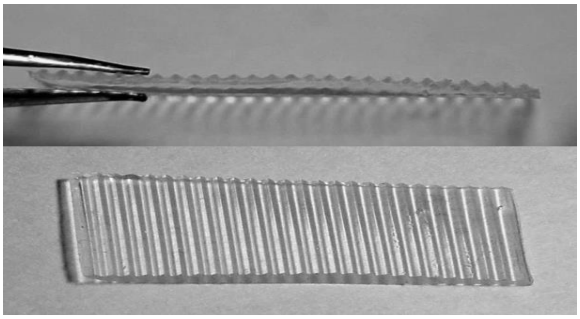

Figure 7.22. Ridged substrate for stretchable photo sensor.

Due to the uniform ridges on the substrate the depositing material got the same shape as of the PDMS substrate.

Table 7.1. EHD parameters for deposition of ITO electrodes and perylene/graphene composite film.

Layers	Spray ITO Bottom electrode	Spray Active layer	Spray ITO top electrode
Ink Flow	40µl/h	60µl/h	40µl/h
Voltage	2 kV	6 kV	2 kV
Nozzle	110 µm	110 µm	110 µm
Stand-of- distance	3 mm	12 mm	3 mm

Each layer (ITO/composite/ITO) is very thin and could not fill the ridges on the substrate, therefore they appeared on the substrate in the form of uniform ridges as shown in Figure 7.23b. Sample was cured at 280 °C for 90 min after the deposition of each layer. After curing the device, silver (Ag) pads were placed at both ends of the sensor to connect the external circuits and electronic instruments; the fabricated device is shown in Figure 7.23b.

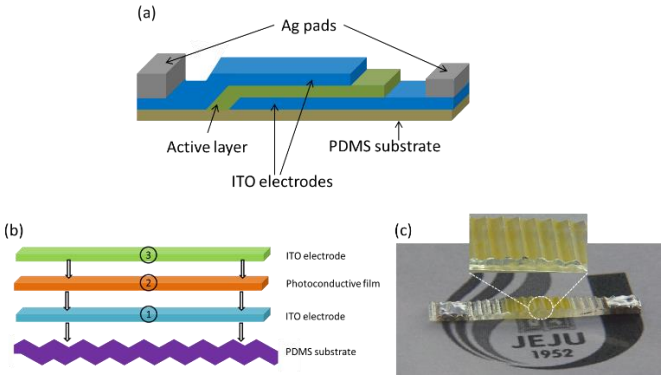

Figure 7.23. (a) Layout diagram of the proposed stretchable photo sensor. (b) Fabrication steps of the device, 1. ITO is deposited on the PDMS substrate to make bottom electrode, 2. Perylene/graphene composite is deposited for active layer, 3. Top electrode of ITO is deposited. (d) Photograph of the fabricated stretchable photo sensor.

7.5.3 Electrical characterization

The fabricated stretchable photo sensor was loaded in a homemade stretching apparatus with a resolution of 10 mm as the schematic diagram is shown in Figure 7.24a. The photo sensor was loaded on the stretching apparatus and placed inside the probe station (Agilent B1500A Semiconductor Analyzer) along a variable light source. Probes were connect at both terminals of the device and resistance was measured against each stretching step while the light source was fixed at 100 lux light intensity. The resistance of the photo sensor at 100 lux was measured by changing the axial strain from 0 to 50% as shown in Figure 7.24b. In the measurement, axial strain percentage (%) is considered as a ratio of a total length of the device, for example, if the length of the device is 2 cm, after stretching the length becomes 3cm which is 50% of the original length.

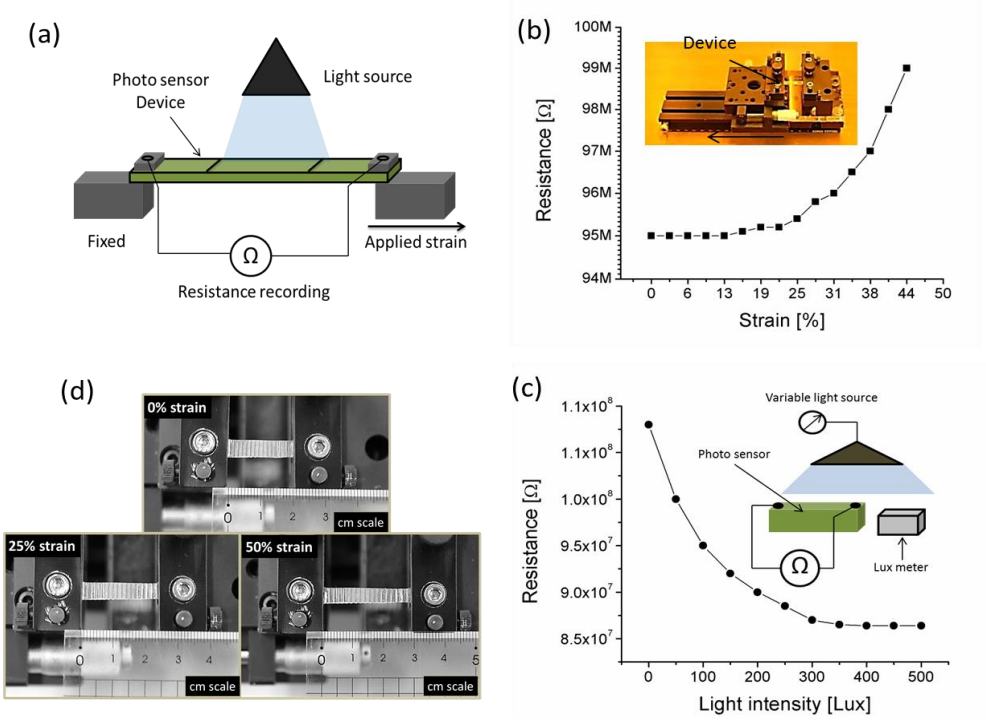

Figure 7.24. (a) Experimental setup to measure stretchability. (b) Variation of resistance by strain percentage. (c) Stretched photo sensors at 0 %, 25 %, and 50 %. (d) Resistance of the photo sensor along light intensity measured as inset experimental setup.

The resistance against stretching until 25% is almost stable and after 25% strain the resistance of the device increased rapidly until 50% strain. The resistance values at 0~25 % strain was 95~95.5 MΩ, whereas at the range of 25~50% strain the resistance value changed from 95.5~99.2 MΩ. This result shows the device has a good performance for stretchability between 0~25% axial strain. The homemade stretching apparatus is shown in the inset of Figure 7.24b. While stretching the device

until 50% axial strain the proposed photo sensor did not show any physical breakdown as the images shown in Figure 7.24c. The length of the device without stretching is 2 cm, the device length became 2.5 cm at 25% axial strain, and length is 3 cm at 50% strain. The stretchable photo sensor has characterized for its electrical properties by using Agilent B1500A Semiconductor Device Analyzer. The device was placed on a sample holder inside the probes station and probes were connected with its terminal. An LED light source with variable light intensity was used with the lux meter near the photo sensor to detect the light intensity as the diagram shown in the inset of Figure 7.24d. The resistance of the photo sensor was observed from 108 MΩ down to 87 MΩ for the light intensity variation from dark to 400 lux as shown in Figure 7.24d. Resistance variation was characterized by measuring the of device along the light intensity of the device became constant. This characterization suggests the device to be used under the 400 lux.

7.5.4 Mechanical characterization

Device was characterized against mechanical stresses by bending it on various diameters from 16 down to 0 mm. The device showed no change toward the bending diameters even completely folded as shown in Figure 7.25a. In the insets, it shows how to take the bendability test of the device manually.

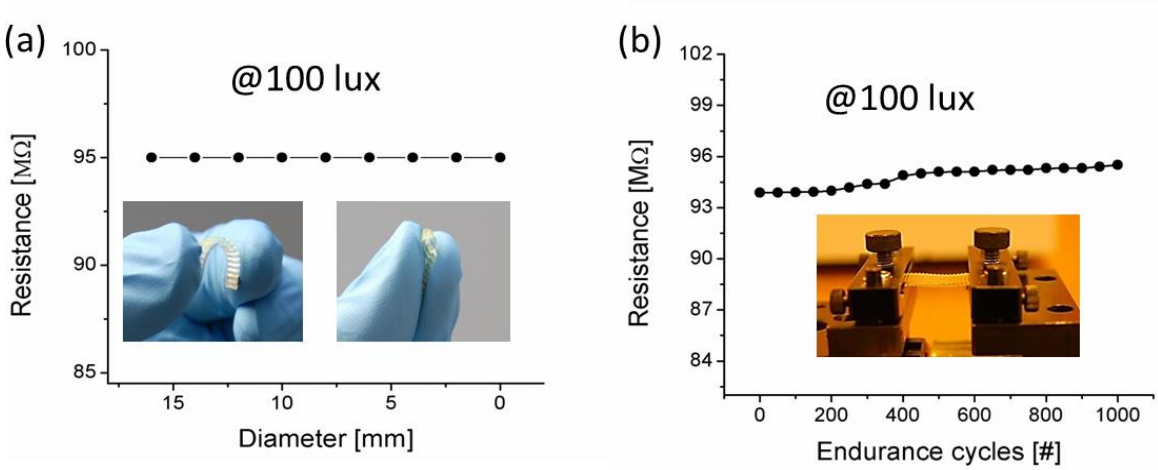

Figure 7.25. (a) Resistance varied by bending diameter. (b) Bending endurance test (resistance vs bending cycles).

To ensure the mechanical reliability of the device it was bended for more than 1000 endurance cycles through an automatic bending machine as shown in the inset of Figure 7.25b. During this test,

the resistance changed from 92 MΩ to 95 MΩ as shown in Figure 7.25b. This result suggests that the device can be utilized in foldable and bendable electronic applications.

Optical characterization was carried out by using UV/Vis Spectroscopy (Shimadzu Corporation - UV-3150). Figure 7.26a show the absorbance spectrum of the PDMS substrate and ITO electrodes, Figure 7.26b shows the absorbance spectrum of the PDMS substrate and ITO electrodes.

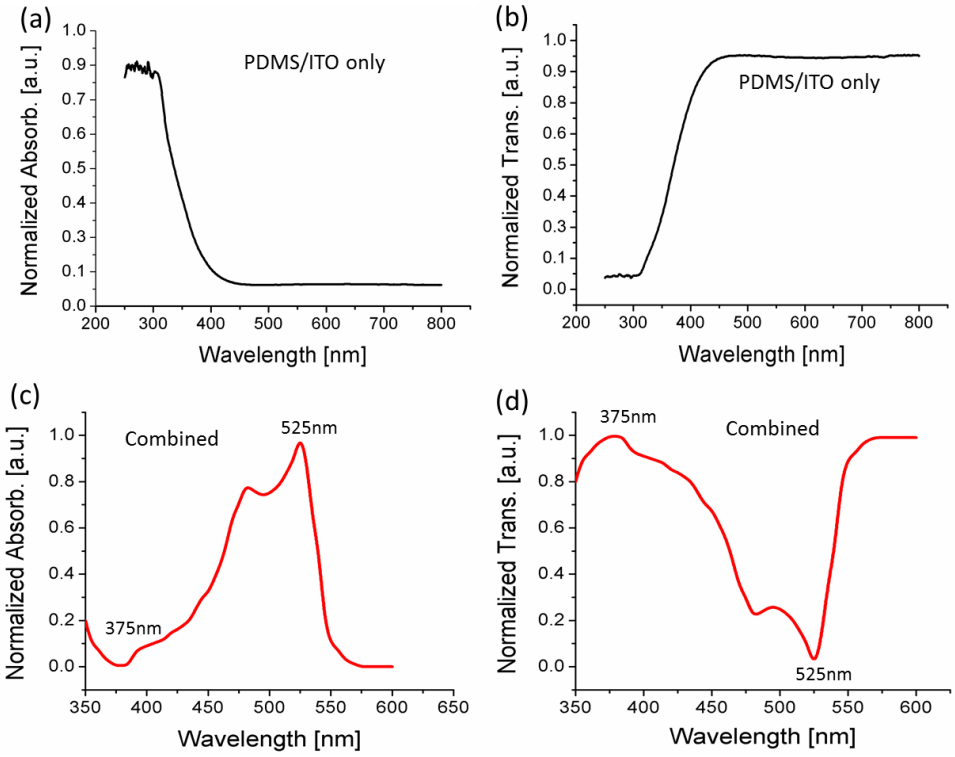

Figure 7.26. Optical property of the active layer (the graphene/perylene film) analyzed through Fourier Transform Infrared Spectroscopy FTIR, (a) absorbance of PDMS and ITO (b) transmittance od PDMS and ITO (c) Absorbance of the device (d) Transmittance of the device.

Figure 7.26c presents the graphene/perylene composite film in visible spectrum range. The absorbance of the thin film is observed to be 50% in the range of 465 nm to 535 nm (blue color) and less than 50% in the range from 350 nm~465 nm (UV and dark blue). The prominent range for the light sensing is from 465 nm to 535 nm as shown in Figure 7.26c. After 535 nm the absorbance goes to zero abruptly, hence the photo sensor cannot detect the light ranging from 550 nm to onward. Figure 7.26d shows the transmittance spectrum of the photo sensor, 1st peak is at 375 nm and 2nd peak at 495 nm where transmittance is high. The minimum transmittance is at 525 nm as the peak shown in Figure 7.26b, after this peak the transmittance increasing, abruptly. The transmittance spectrum shows that the graphene/perylene composite thin film is more suitable for optoelectronic

device applications due to the good transparency. From these results, the proposed sensor can be applied to detect a light intensity in various applications including biomedical and electronic circuits. These characteristics show that the proposed device is promising candidate to be used in stretchable, flexible, transparent, and low cost electronic applications for the sensing of blue and UV light up to 400 lux

7.6 Summary

In first section, a differential temperature sensor is successfully demonstrated, which can measure temperature as well as strain of a flat, flexible and curved surface. Dimatix material inkjet printer DMP-3000 was used to fabricate the silver nanoparticles based back-to-back meander patterns on a PET substrate at ambient conditions. The serially connected back-to-back meander patterns have eliminated the temperature error caused by mechanical deformation of the sensor. The resistance of the DTS sensor varies with temperature regardless of its bending diameter, and the TCR of temperature sensor was observed to be 1.138 x 10-3 °C-1. The sensor showed strain-sensing behavior under bendability from 8 mm down to 2 mm by single meander coil, and the resistivity Changed by 24.94%. The DTS showed reliability for more than 300 endurance cycles at 2 mm and 5 mm diameters. These characterizations can be good basis to develop a novel sensor for the temperature and bending sensing in wearable electronics with good resolution.

In second section, a humidity sensor based on graphene/methyl-red composite thin film is demonstrated for high sensitivity measurement. The sensor is consisted of inter-digital electrodes deposited through inkjet material printer DMP-3000 and sensing thin film (~300 nm) deposited through EHD technique. The senor's resistance inversely varies from 11 MΩ down to 0.4 MΩ against RH from 5 to 95%. In the case of capacitive sensing, the capacitance varies from 2.3 pF to 66 nF against RH from 0 to 100%. The response and recovery time of 0.251s and 0.35s have been recorded against 35 to 100% RH, respectively. The proposed humidity sensor has a high resistive sensitivity of 96.36% and capacitive sensitivity of 2869500%. The high sensitivity of the presented sensor is achieved due to both graphene/methyl red composite thin film and optimum inter-digital electrodes. Moreover, its fabrication process is very simple as it is all-printed over a low cost flexible and transparent PET substrate. The proposed sensor can be easily integrated with the wearable electronic devices. In last section, A flexible/stretchable photo sensor consisted of photoconductive layer of perylene/graphene, interdigital electrodes silver, ITO and substrates PET and PDMS were utilized. The stretchable photo sensor showed stable behavior under 25% axial

strain, whereas it is stretchable up to 50% without electrical and mechanical breakdown. The resistance of the proposed photo detector varied from 108 MΩ to 87 MΩ against light intensity of 0~400 lux, respectively. The maximally detectable light intensity by the photo sensor is 400 lux and its detectable range is from 465 nm to 535 nm in the visible spectrum. The device showed bendability down to 0 mm for more than 1000 endurance cycles. In the result of these characterizations, the proposed photo sensor is good candidate for the stretchable, flexible, and transparent electronic applications.

7.7 References

[1] Y. Yang, et al., Sens. Actuat. A: phys. 143 (2008) 143-153.
[2] H. Leng, et al., Int. J. Smart and Nano Mater. 2 (2011) 78-82.
[3] D.J. Lichtenwalner, et al., Sens. Actuat. A: phys. 135 (2007) 593-597.
[4] C. Lee, et al., Int. J. Hydrogen Energy 37 (2012) 3459-3465.
[5] C. Lee, et al., Sens. Actuat. A: phys. 147 (2008) 173-177.
[6] N. Wilke, et al., Sens. Actuat. A: phys. 123-124 (2005) 319-325.
[7] Y. Moser, et al., J. Microelectromech. Syst. 16 (2007) 1349-1354.
[8] S. Xiao, et al., Microelectron. J. 38 (2007) 360-365.
[9] J. C. Oprea, et al., Sens. Actuat. B: Chem. 140 (2009) 227-233.
[10] S.R. Samarasinghe, et al., Appl. Phys. A 91 (2008) 141-147.
[11] H. Petrova, et al., Physical Chemistry Chem. Phys. 8 (2006) 814-822.
[12] K.H. Choi, et al., J. J. App. Phys. 53 (2014), 05HB02-05HB07.
[13] G. Mattana, et al., IEEE Sensors J. 13(10) (2013) 3901–3909.
[14] F. Molina-Lopez, et al., Microelectron. Reliab. 54 (11) (2014) 2542-2549.
[15] J.A. Rogers, et al., Science 327 (2010) 1603-1607.
[16] S. Ali, et al., Opt. Express 23 (2015) 30583-30591.
[17] D. Soltman, et al., Langmuir 24 (2008) 2224-2232.
[18] M.S. Onses, et al., Nat. Nanotechnol. 8 (2013) 667-676.
[19] J. Martinez-Quijada, et al., Sens. Actuat. A: Phys. 193 (2013) 170-182.
[20] Sun A, et al., Sens. Actuators B: Chem 2009;139:543–547.
[21] Kuang Q, et al., J. Am. Chem. Soc 2007;129,6070–6071
[22] Anderson D. S, et al., Nanoscale 2015;7, 19099-19109.
[23] Borini S, et al., Nano 2013,7(12),11166-11173.
[24] Buvailo A, et al., Sens. Actuators, B 2011;156,444–449.
[25] Lin Q, Li Y, et al., Anal. Chim. Acta 2012;748,73–80.
[26] Li Y, et al., Sens. Actuators B: Chem 2005;107: 252–257
[27] Li Y, et al., Sens. Actuators B: Chem 2007;123, 554–559.

[28] Li Y, et al., J. Mater. Sci 2005; 40,245–247.
[29] Yoo K.P, et al., Sens. Actuators B: Chem 2010;145,120–125.
[30] Power A, et al., Analyst 2010;135,1645–1652.
[31] Sun A, et al., Sens. Actuators B: Chem 2009;142,197–203.
[32] Sappat A, et al., Thailand 2011; 34–37.
[33] Korotcenkov G, Mater. Sci. Eng B 2007; 139,1–23.
[34] Kong, J, et al., Science 2000;287,622-625
[35] Zhou X.T, et al., Chem. Phys. Lett 2003,369,220–224.
[36] Novoselov K.S, et al., Proc. Natl. Acad. Sci 2005;102,10451-10453.
[37] Schedin F, et al., Nat. Mater 2007; 6,652–655.
[38] Bolotin K.I, et al., Solid State Commun 2008;146,351–355.
[39] Wilke N, et al., Sens. Actuat. A:phys 2005;123-124,319-325.
[40] Ali S, et al., Org. Electron. 2015; 17, 121-128.
[41] Ali S, et al., Opt. Express. 2015;23, 30583-30591.
[42] Yang Y, et al., Appl. Phys. Lett 2011;98, 093116.
[43] Freitas R. R. Q, et al., J. Phys. Chem A 2011;115,12348–12356.
[44] Leenaerts O, et al., Phys. Rev. B: Condens. Matter 2009;79,235440.
[45] Wehling T. O, et al., Chem. Phys. Lett 2009;476,125–134.
[46] Wang S, et al., J. Phys. Chem. C 2015;*119*(51),28640-28647.
[47] Hamilton, et al., *IEEE J. of Selected Topics in Quantum Electronics* 10 (2004) 840-848.
[48] G. Pace, A. Grimoldi, et al., Adv. Mater. 26 (2014) 1521-4095.
[49] Kang-Jun Baeg, et al., Adv. Mater. 25 (31) (2013) 4267-4295.
[50] Bruno Romeira, et al., Sensors 13 (2013) 9464-9482.
[51] Kim, et al., Nature 479 (2011) 338-344.
[52] Taehyun Hwang, et al., Sensors and Actuators B: Chemical 187 (2013) 319-322.
[53] L. Schmidt-Mende, et al., Science 293 (2001) 1119-1122.
[54] Nur Pasaogullari, et al., Dyes and Pigments 69 (2006) 118-127.
[55] Linh-Nam Nguyen, et al., Applied Physics Letters 103 (2013)183301-183306.
[56] Erika Kozma, et al., Dyes and Pigments 98 (2013) 160-179.
[57] Sang Hyun Oh, et al., Dyes and Pigments 85 (2010) 37-42.
[58] Erica Torres, et al., Dyes and Pigments 112 (2015) 298-304.
[59] R. Zhongjie, et al., J. Mter. Chem. 22 (2012) 18839-1884

Chapter 8 Printed Rectifiers

Due to versatile properties of the conducting polymers [1], organic based electronics such as organic light-emitting diodes (OLEDs), organic thin film transistors (OTFTs), photovoltaic, radio frequency identification (RFID), and memory devices have been extensively researched because of their flexibility, easy, and low cost fabrication [2]-[6]. In printed electronics, a rectification to convert an alternating current (AC) into a direct current (DC) is an essential process since most of the electronic devices operate on DC power. To realize this function, a printed diode fabricated through low cost fabrication technology is a basic component. Especially, the main constraints of the rectifier diodes are high speed, strong rectification ratio, and high current density. To fulfill these requirements, various rectifier diodes have studied as structures such as metal/organic, inorganic/organic, and p-i-n organic/organic semiconductor heterojunction [7]-[9]. Most of the organic materials are not suitable for rectifying diodes applications because of their low mobility [10]. However, some organic materials provide high mobility for both holes and electrons even in solution processed based devices [10]-[12]. Two organic materials for a higher mobility both fullerene (C_{60}) for electron transportation (n-type semiconductor) and N,N′-Bis(3-methylphenyl)-N,N′-diphenylbenzidine (TPD) for holes transportation (p-type semiconductor) are proposed [13]. These two materials have comparatively good performance for diode applications due to their energy levels and electrons-holes mobility. Fullerene (C_{60}) is an n-type organic semiconductor, and the band gap of the C_{60} is 6.4 eV at HOMO and 4.1 eV at LUMO. TPD is organic semiconductor molecule with 2.3 eV at LUMO and 5.4 eV at HOMO, which is the most commonly material used in organic light emitting diodes (OLEDs) for holes-transportation, in solar cells for photoconduction, and in laser devices [14].

8.1 Printed High Rectification Diode based on C_{60} and TPD

In the section, an all-printed organic diode for high rectification ratio and high current density is presented that can be utilized in printed electronic circuits. The device heterojunction is made of fullerene (C_{60}) for n-type semiconductor and N,N′-Bis(3-methylphenyl)-N,N′-diphenylbenzidine (TPD) for p-type semiconductor. In both side of the heterojunction, an anode is made of thin film of indium tin oxide (ITO) and a cathode is made of thermally evaporated aluminum (Al). The

proposed device is fabricated on a glass substrate through a cost effective and eco-friendly electrohydrodynamic (EHD) technique at ambient conditions and 35% humidity level throughout the experiments. The effective area of the devices is 2×2 mm^2, and the device was encapsulated with PDMS. The current density–voltage (I–V) characteristics of the proposed device were measured using a HP4140B Pico ammeter and Agilent Semiconductor Analyzer B1500A at ambient conditions. From these electrical characteristics, the high rectification ratio (1.2×10^4), the good current density at low voltages (550 mA/cm^2 at 3 V), and the high ratio between reverse bias resistance and forward bias resistance (2.5k) are demonstrated. The proposed device structure is ITO/TPD/C_{60}/Al as shown in **Figure 8.1**a, where, TPD is the p-type semiconductor with hole mobility of 1×10^{-4} cm^2/Vs and C_{60} is the n-type semiconductor with an electron mobility of 1.3 cm^2/Vs [12]. The energy level diagram is show in **Figure 8.1**b, the energy barrier from the HOMO of TPD to the HOMO of C_{60} is 0.9 eV, and it ensuring that holes are very difficult to get over such higher energy barrier. The energy barrier from the LUMO of C_{60} to the LUMO of TPD is 1.8 eV, which makes the electron impossible to be injected from C_{60} layer to TPD layer. Electrons and holes would be accumulated at the TPD/C_{60} interface upon application of external forward bias voltage. That will make electrons and holes move toward the heterojunction for recombination process.

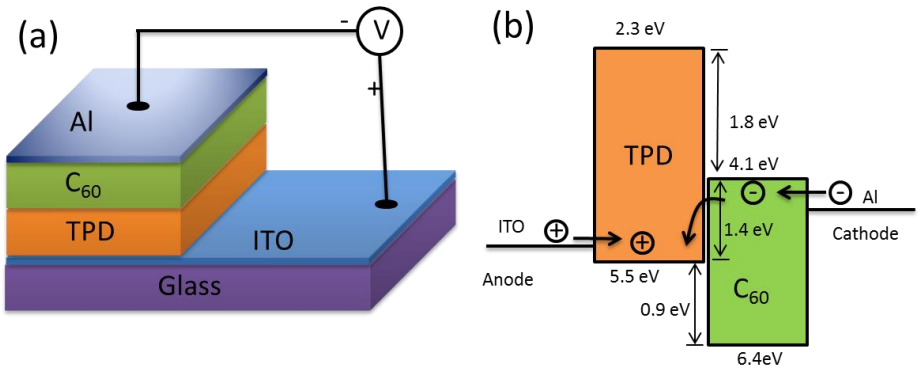

Figure 8.1. (a) Layout and material diagram of the organic diode. (b) Energy diagram of the proposed diode showing energy levels of the proposed TPD/C 60 heterojunction , a 1.4 eV difference is created between HOMO and LUMO of TPD and C_{60} , respectively.

When reversed bias, electrons and holes will move away from the junction and the device will be observed a high resistance. The C_{60} has special spherical π-electron carbon cluster, and it is an organic semiconductor due to the band gap of solid C_{60} is in the range of 1.2 – 2 eV. Melting point for this organic semiconductor material is 280 °C. TPD is the organic semiconductor molecule and a well-known hole-transport material for organic electronics. The LUMO and HOMO for this particular material is 2.3 eV and 5.4 eV, respectively, and the melting point is 170 °C.

8.1.1 Fabrication

Prior to the fabrication of the device, material was synthesized for both P and N type semiconductor and then the device was fabricated through EHD technique. Now the following sections will describe the detailed procedure about material preparation and device printing.

8.1.1.1 Material synthesis

Materials were purchased from sigma Aldrich South Korea, inks of TPD p-type material and C_{60} n-type material were prepared as: dissolving TPD material in solvent (toluene) 10 wt% and dissolving C_{60} in toluene 8 wt%. Both inks were prepared by using magnetic stirrer at 1000 rpm and 40 °C. Both inks were further mixed with N-N Dimethylformalehye (DMF) with ratio 1:2/3 to increase the electrical conductivity of the solvent to enable the electrohydrodynamic (EHD) deposition phenomenon. The final solution was again stirred for 1 hour. During the preparation of materials, humidity level was 35% fixed in the lab.

8.1.1.2 Layer deposition

The control parameters of the EHD system for a stable cone jet were adjusted for TPD and C_{60} materials deposition separately and the optimum values of the EHD control parameters are given in Table 8. 1. The operating voltage and ink flow rate is different for both the materials because of their different ink conductivity and viscosity. Details about the EHD fabrication technique can be found in chapter 1. The layers are deposited on the substrate one by one as shown in Figure 8.2a. After deposition, each layer was cured at 280 °C for 120 min. Top electrode of aluminum (Al) was thermally evaporated to make anode connection. Different devices were fabricated having different thickness of the layers, and the thickness of the layers was controlled during EHD fabrication through number of passes (multiple spray coating). The optimum thickness of the heterojunction materials was observed 35 nm for TPD and 70 nm for C_{60}. Using these fabrication processes, the proposed organic diodes on the single glass substrate are manufactured as shown in the Figure 8.2b. First, TPD layer was deposited on ITO coated PET substrate and cured at 280 °C. Second, C_{60} was deposited with long standoff-distance 15 mm, 170 ul/h ink flow rate, and 6kV operating voltage. These parameters led the deposition of the C_{60} layer without damaging the cured TPD layer due to almost all solvent is evaporated before reaching the substrate.

Table 8. 1. Experimentally observed EHD parameters for TPD and C 60 layers deposition.

Layers	Applied voltage KV	Applied flow Rate µl/h	Stand off Distance (mm)	Substrate Velocity (mm/s)
TDP	4.2	110	11	1
C_{60}	6	20	1.2	3

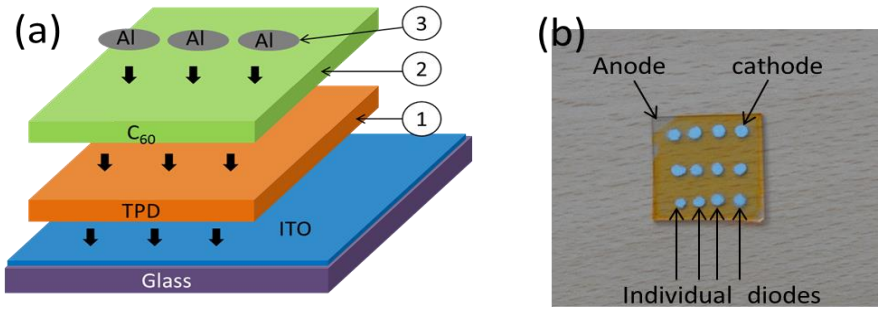

Figure 8.2. (a) Schematic diagram of layer deposition sequence. (b) The digital image of fabricated organic diodes on a glass substrate.

8.1.2 Characterization

8.1.2.1 Surface morphology

The fabricated device was analyzed for its morphological characteristics by taking field emission scanning electron microscopy (FE-SEM) images to verify the proper deposition of the layers. Figure 8.3a shows the cross sectional FE-SEM image of the device and all layers are deposited properly. From this analysis, they have the uniform thickness even though the heterojunction materials are deposited through EHD system that is why having a variation in thickness. Figure 8.3b and c show the FE-SEM images of the TPD and C60 layers. From the analysis, there verify that all the layers are uniformly deposited without cracks on films.

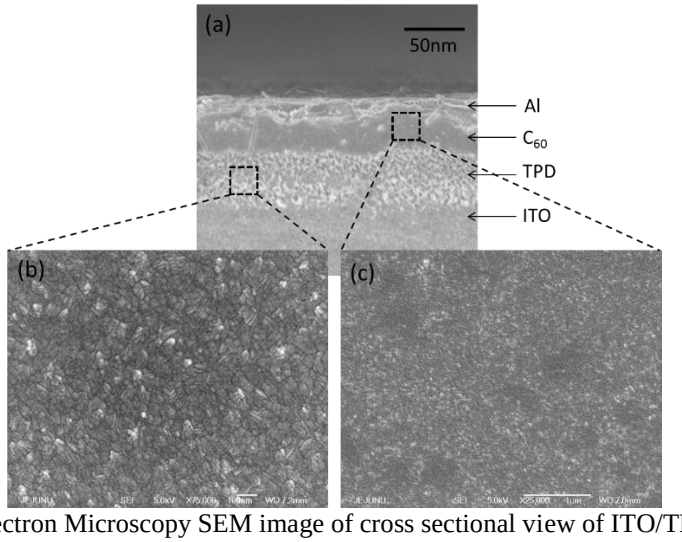

Figure 8.3. (a) Scanning Electron Microscopy SEM image of cross sectional view of ITO/TPD/C 60 /Al diode, (b) TPD layer, and (c) C 60 layer of the diode.

8.1.2.2 Electrical characterization

The current density–voltage (I–V) characteristics were measured using a HP4140B pico-ammeter. Probes were connected to the diode terminals, and a voltage sweep from -8 V to 3 V was applied. Figure **8.4**a shows the I–V characteristics curve of the device, it shows an exact behavior of the diode as the current is flowed in the forward bias and current is not flowed in the reverse bias. The turn on voltage of device was approximately 1.2 V, and current density 100 mA/cm2 at 1.7 V and 550 mA/cm2 at 3.0 V. This I-V behavior shows excellent diode characteristics, whereas the revers bias current is a very low comparing to forward bias current. Especially, the current density of 550 mA/cm2 at 3V shows a strong rectification of the device. To analyze the reverse current it is demonstrated on a log scale with voltage sweep from -8 V to 3 V as shown in the inset of Figure 8.4a. The reverse current density at -3 V is almost 5 µA/cm2 because of the minority carriers in TPD and C60. Under the bias voltage electrons and holes are moving towards the TPD/C60 heterojunction in the result a large energy offsets at LUMOs and HOMOs lead to electrons and holes accumulation at the heterojunction. These accumulated charge carriers at the heterojunction recombine non-radioactively through a charge transfer exciton recombination process leads to high current at low bias voltages. The device was analyzed for the current density at various temperatures starting from 30°C to 120°C. The initial temperature was set to 30 °C and then it was increased to 120 °C with incremental step of 30 °C. It was observed that as the temperature increases the threshold voltage reduces and current density increases as shown in the Figure 8.4b. Current transport across the semiconductor interface is temperature dependent. Thus, the electrons at low temperature would be able to cross only the lower barriers. Therefore, current transport is limited by current passing through the lower energy barrier and produces a large ideality factor. With increasing temperature, the electrons would acquire significant energy to cross higher barrier levels and at low bias voltage high current flow. As this result, the effective barrier height will increase with the temperature and threshold voltage is reduced. As the I-V curve of the device without encapsulation shown in the inset of Figure 8.4b it was observed that the current density of the device without encapsulation is low and current does not increase exponential as compare to encapsulated device.

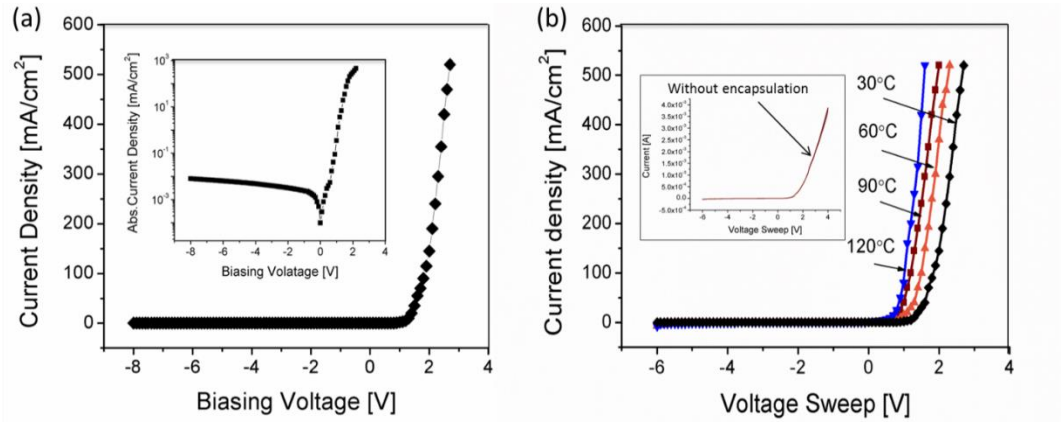

Figure 8.4. (a) Current density-voltage curves of the organic diodes, where, the inset shows absolute I-V curves of the diode. (b) Current density vs voltage at temperature values 30, 60, 90 and 120°C. The inset shows I-V curves of the diode without encapsulation.

Figure 8.5a shows that the device has a strong rectification characteristic. Because of the low mobility of electron in TPD and hole in C_{60} (2.0×10^4 cm^2/Vs) [12], it is not capable of transporting high current at very low electric fields, hence reverse current is very small. The lifetime of a charge carrying exciton recombination at heterojunction can be calculated [15].

$$\tau = \frac{1}{n * R_{ec}} \qquad (1)$$

Where R_{ec} is the recombination coefficient and n is the carrier concentration, which can be calculated the following equation.

$$n = \frac{jd}{\mu qV} \qquad (2)$$

Here, j is current density, "d" is the film thickness, "μ" is the mobility of the organic materials, q is the electron charge, and V is the applied voltage. In the organic devices, the charge transfer exciton recombination rate is reduced by the mobility of holes charge carriers since they are much slower than the electrons. The mobility of charges used to calculate the life time of charge carrying exciton transfer is the hole mobility of TPD (1×10^{-4} cm^2/Vs). The measured current density of the fabricated diode was 550 mA/cm^2 at 3V and it has used to calculate the lifetime of charge transfer exciton of the interface, that is ~149 ps. Junction resistance of the device during forward biased and reverse biased was measured by applying voltage sweep from -4 V to 4 V, and current values were recorded against each point of voltage as shown in Figure 8.5b. It has observed that at higher voltage (3 V) in forward bias the junction resistance approaches to 1kΩ, whereas in reversed bias the resistance

at -3V became 2.5 MΩ. This high ratio (2.5k) between forward and revers bias resistance plays an important role in the rectification of the diode offering high resistance to reverse bias and low resistance to forward bias voltage. The resistances of both sides are an important value due to these values will help in impedance matching when the diode will interfaced with other electronic components in series or parallel. Figure 8.5c. shows the capacitance–voltage (C–V) behavior at 4 kHz for the device ITO/TDP/C60/Al.

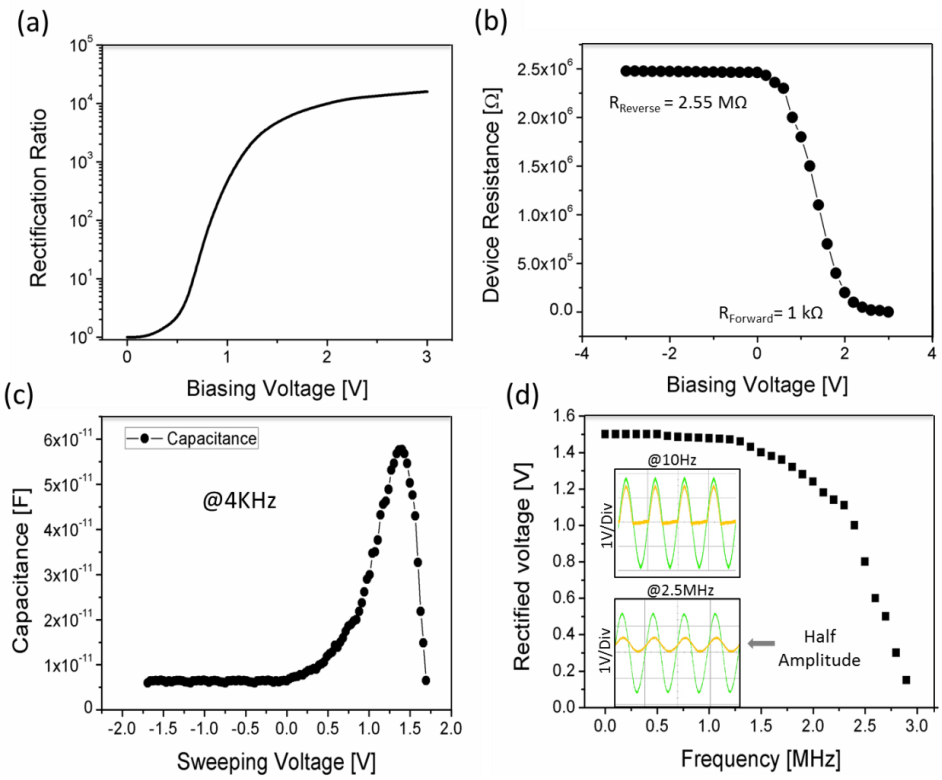

Figure 8.5. (a) Rectification ratio of the ITO/TPD/C 60 /Al diode. (b) Forward and reverse resistance of the proposed diode under biased condition. (c) Capacitance-voltage (C-V) characteristics of the ITO/C 60 /TPD diode. (d) Rectified signal amplitude versus frequency, the inset shows the rectified and input signal at 10 Hz and 2.5 MHz frequency.

During the forward bias voltage from 0 to 1.5 V, capacitance increases with the applied voltage, it is changed due to the decrement in the depletion region. After 1.5V, the capacitance sharply decreases, this is an effect of the free carriers which are stored at the depletion region of the p-n junction at lower voltage than threshold. On the reverse bias, the capacitance decreases as the absolute value of applied voltage increases, and this capacitance is changed due to the increase in the width of the depletion region. The C–V characteristic is typical of a p-n junction diode where the capacitance change due to dual polarity voltage indicates the formation of a depletion region. Figure 8.5d shows the variation in the output voltage of the rectified signal versus frequency analysis from 0 to 3 MHz frequency span. It was observe that the half wave rectified output voltage

amplitude was gradually decayed after 1.5 MHz. At 2.5 MHz, the signal decays to 50% of its 10 Hz frequency amplitude. This rectification behavior shows that the half amplitude cut off frequency of the proposed diode is 2.5 MHz.

8.1.3 Summary

In section 8.2, all-printed organic diode with the higher rectification ration fabricated on the glass substrate through the EHD technique has been presented. The structure of the diode is composed of ITO/TDP/C_{60}/Al. The optimum material combination for heterojunction led the proposed diode to conduct at voltage of 1.2sV with current density of 550 mA/cm^2 maximum at 3 V. The fabricated device using for the n-type material (C_{60}) and the p-type material (TPD) was operated with a strong rectification ratio of ~1.2x10^4 because of the low minority carriers in both materials. Furthermore, morphology analyses of the device were carried out with FE-SEM to verify the successful deposition of all layers through EHD technique. From these characterizations of the proposed organic diode, it can be good role to develop a novel device in all-printed electronic circuits.

8.2 References

[1] J. Heeger, et al., Rev. Mod. Phys. 60, 781 (1988).
[2] T. Sekitani, et al., IEEE Trans. Electron Dev. 56, 1027 (2009).
[3] Forrest, S. R. Nature 428, 911 (2004).
[4] T. Sekitani, et al., Science 326, 1516 (2009).
[5] S. Ali, J. Bae, K. H. Choi, C. H. Lee, Applied Physics A (2015).
[6] E. Cantatore, et al., Solidstate circuits, IEEE J. 42, 84 (2007).
[7] S. Steudel, et al., Nature Mater. 4, 597 (2005).
[8] D. Im, et at., Adv. Mater. 23, 644 (2011).
[9] H. Kleemann, et al., Organic Electronics 13, 1114 (2012).
[10] H. Usta, et al., Accounts of Chemical Research 44, 501 (2011).
[11] J. Smith, et al., Adv. Mater. 24, 2441 (2012).
[12] M. Mustafa, et al., J. Materials Science: Materials in Electronics 24, 4321 (2013).
[13] Z. Nan, et al., Chinese Physics Letters 25, 1091 (2008).
[14] T. Yamada, et al., Organic Electronics 11, 255 (2010).
[15] S.M. Sze, K.K. Ng, Physics of Semiconductor Devices, third ed., John Wiley & Sons Inc, Hoboken, NJ, (2007).

Chapter 9 Conclusions and Future Work

This short chapter presents the overall conclusions of the thesis dissertation and highlights the contribution made in the Printed and Flexible Electronics fields.

9.1 Overview and General Conclusions

Printed electronics is a new technology that enables low cost and large area devices, it is emerging in the present electronics industry to cover the cost and technological gaps associated with conventional electronic processing and application demands. The demands of low-cost, flexibility, and low temperature processing forcing the research and industry to work on this new emerging branch of electronics.

Printed electronics is relatively new field, hence facing problems of fabrication techniques, materials for device as well as for encapsulation of the electronic devices to make them reliable. In past two decades, big efforts have been made in substituting the organic, inorganic semiconductors, silicon dioxide insulator and the metals for organic materials. Apart from the material exploration for the new devices, fabrication techniques are also under investigation to enable them for effective fabrication. Some fabrication techniques are matured and been adopted by the electronic industry such as inkjet, spin coater and EHD, however some techniques are under research yet. In this thesis work EHD, spin coater and Inkjet printer are used for the fabrication of devices. Materials including organic and inorganic are synthesized for the low-cost fabrication techniques and their deposition is confirmed with characterizations. This dissertation contributes to the Research and Development R&D community to address the challenges in the fabrication process of all-printed electronic devices and circuits. Main contributions are listed as below:

1. Printed and flexible organic resistor is presented by utilizing MEH:PPV and PMMA composite fabricated through EHD technique on PET substrate. The resistance value can be predicted by the given expressions and the resistivity is controlled to avoid the size limitation. This device can be used in electronic circuits as a resistor whereas the size of component is independent of resistance value.

2. Memristor based on graphene quantum dots and PVP composite on PET substrate is fabricated through EHD technique. This device provides highly stable resistive switching and can be used in crossbar passive memories (ReRAM). Another memristor based on zinc stannate $ZnSnO_3$ is fabricated on PET substrate with EHD technique. The device exhibits resistive switching with high endurance cycles and can be used in potential applications of ReRAM.
3. Pull-up resistors are introduced in the conventional crossbar array to enable parallel readout and minimize the sneak currents. Pull-up resistors are connected in series with memristors making a voltage divider network. This type of memory read the logic data in the form of voltage instead of current. The memristor utilizes PVP material and resistor is made of MEH:PPV and PMMA composite. The 3 x 3 array is demonstrated on PET substrate through EHD technique.
4. Tristate memory is presented which is composed of two serially connected memristors. These memristors can be switched individually in LRS and HRS states that give three distinct states of the memory cell. This architecture provides very high on/off ratio of ~6000 which improve the detection margin in reading logic data.
5. Asymmetric memristor is introduced that allow current in one direction and blocks the reverse current same as diode. By utilizing this device in crossbar memory array, it significantly minimizes the sneak currents problem. In conventional 3 x 3 crossbar memory array suffers from sneak currents where the read current is erroneous while the presented device can achieve 673 x 673 array with sufficient detection margin.
6. To measure the humidity level, I have presented inkjet printed sensor on PET substrate by utilizing graphene and methyl-red composite ink. This sensor achieves a sensing range of 5-95% RH with sensitivity of 96%. The response time of the sensor is 0.25s and the recovery time is 0.31s.
7. In order to measure the temperature of bendable and flexible surface, a differential temperature sensor (DTS) is proposed which is fabricated through inkjet printer by utilizing AgNPs on PET substrate. The construction of the sensor is two meander patterns are precisely printed back to back on PET substrate and connected serially. In bent position one meander pattern experiences tension while the other compression. In this way, the resistance of one meander pattern increases while the other's decreases. The net resistance remains unchanged only effected by the environmental temperature.

8. Passive filters based on memristors and capacitors are presented in which the cutoff frequency of the filter can be tuned by switching the memristor in LRS or HRS states. The memristor replacing the resistor in conventional RC filter circuit providing two programmable resistive states.
9. In the last section, an organic diode for the rectification purpose is presented that is fabricated on a glass substrate by utilizing TPD and C_{60} materials. The device is fabricated through low cost EHD technique. The device showed high rectification ratio of $1.2x10^4$. This device can be used in printed electronic circuits for the rectification purpose.

9.2 Future Work

At the end of each chapter there is summary of the section where the achieved performance is discussed with their numerical values. Every device, circuit and system has to be improved by mean of fabrication technique, fabrication process or by changing material. In future, these devices special can be investigated for better performance and reliability. Specifically memristors presented in this work on different substrates with different materials can be improved for high retention time, endurance and off/on ratio. Apart from the performance improvement, integration with the exiting CMOS technology is still an issue for real time printed electronics applications. Conventional CMOS technology is based on three-terminal transistor while the resistive switch is two-terminal device that needs different circuit design strategy. SM-OLED device were fabricated and achieved orange light with maximum light intensity of 5lux at 9V. This device can be investigated for multi colours and more light intensity. In the sensors section, humidity sensor can be improved for their response time by adding some new material having hydrophobic nature. Asymmetric memristor can enhance the ReRAM area significantly and the device can be investigated further for the performance and reliability.

Annex-A Journal Papers

1. **Shawkat Ali**, Jinho Bae, Chong Hyun Lee, Kyung Hyun Choi, Yang Hoi Doh: *Flexible and passive photo sensor based on perylene/graphene composite*. Sensors and Actuators B Chemical 12/2015; 220(1):634–640. DOI:10.1016/j.snb.2015.05.128

2. **Shawkat Ali**, Jinho Bae, Chong Hyun Lee: *Organic diode with high rectification ratio made of electrohydrodynamic printed organic layers*. Electronic Materials Letters 11/2015; 14(10).

3. **Shawkat Ali**, Jinho Bae, Chong Hyun Lee: *Stretchable photo sensor using perylene/graphene composite on ridged polydimethylsiloxane substrate*. Optics Express 11/2015; 23(24):30583-30591. DOI:10.1364/OE.23.030583

4. **Shawkat Ali**, Jinho Bae*, Chong Hyun Lee, Kyung Hyun Choi, Yang Hoi Doh: *All-printed and highly stable organic resistive switching device based on graphene quantum dots and polyvinylpyrrolidone composite*. Organic Electronics 10/2015; 25. DOI:10.1016/j.orgel.2015.06.040

5. **Shawkat Ali**, Jinho Bae, Chong Hyun Lee: *Design of versatile printed organic resistor based on resistivity (ρ) control*. Applied Physics A 04/2015; 119:1499–1506. DOI:10.1007/s00339-015-9127-y

6. **Shawkat Ali**, Jinho Bae, Kyung Hyun Choi, Chong Hyun Lee, Yang Hoi Doh, Sangho Shin, Nobuhiko P. Kobayashi: *Organic non-volatile memory cell based on resistive elements through electro-hydrodynamic technique*. Organic Electronics 12/2014; 17. DOI:10.1016/j.orgel.2014.11.028

7. Adnan Ali, Abdelhak Belaidi, **Shawkat Ali**, Mohamed I. Helal, Khaled A. Mahmoud: *Transparent and conductive Ti3C2Tx (MXene) thin film fabrication by electrohydrodynamic atomization technique.* J Mater Sci: Mater Electron. 2016; DOI: 10.1007/s10854-016-4447-z

8. **Shawkat Ali**, Arshad Hassan, Gul Hassan, Jinho Bae, Chong Hyun Lee: *All-Printed humidity sensor based on graphene/methyl-red composite with high Sensitivity.* Carbon, 2016, 105, 23-32.

9. **Shawkat Ali,** Jinho Bae, Chong Hyun Lee: *Printed Non-Volatile Resistive Switches based on Zinc Stannate ($ZnSnO_3$);* Current Applied Physics, 2016; 16 (7) 757–762

10. **Shawkat Ali,** Arshad Hassan, Jinho Bae, Chong Hyun Lee: *Printed differential temperature sensor for the compensation of bending effect;* Sensors and actuators A:Physical, 2016 (in publication process)

11.

Annex-B to be Submitted Papers

1. **Shawkat Ali**, Jinho Bae, Adnan Ali, Chong Hyun Lee, Sangho Shin, Nobuhiko P. Kobayashi: *Ultra-asymmetric memristor for sneak current elimination in passive crossbar arrays;* Nature materials (submitted)

2. **Shawkat Ali**, Arshad Hassan, Gul Hassan, Fasiullah khan, Jinho Bae and Chong Hyun Lee, Chang-Ho Eun: *Rapid Detection and Classification of Foodborne Pathogens using a Disposable All-printed electronic biosensor;* Scientific reports (Submitted)

3. **Shawkat Ali**, Jinho Bae, Chong Hyun Lee: *AND resistive switches for passive crossbar arrays*, Nature materials (In preparation)

4. **Shawkat Ali**, Arshad Hassan, Jinho Bae and Chong Hyun Lee: Memristor-Capacitor Frequency Selective passive Filters, IEEE Electron Transaction (In Preparation)

5. **Shawkat Ali**, Jinho Bae, Chong Hyun Lee, Sangho Shin, Nobuhiko P. Kobayashi: State Memorable Light Emitting Device, Nano Letters, (to be submitted)

6. **Shawkat Ali**, Jinho Bae, Chong Hyun Lee, Sangho Shin, Nobuhiko P. Kobayashi: serial and parallel control of OLED, Nano Letters, (to be submitted)

7. **Shawkat Ali**, Jinho Bae, Chong Hyun Lee, Sangho Shin, Nobuhiko P. Kobayashi:Ultra-low power non-volatile resistive crossbar memory based on pull up resistors, Organic Electronic (Submitted)

8. **Shawkat Ali**, Jinho Bae, Adnan Ali, Chong Hyun Lee, Sangho Shin, Nobuhiko P. Kobayashi: *Stacking ultra-asymmetric memristor for high density passive crossbar arrays;* Nano Letters (In preparation)

Annex-C Conference Papers

1. **Shawkat Ali**, Jinho Bae, Chong Hyun Lee: *Flexible and stackable non-volatile resistive memory for high integration*. Proc. SPIE 9553, Low-Dimensional Materials and Devices,, San Diego, California, United States; 08/2015

2. **Shawkat Ali,** Jinho Bae, Chong Hyun Lee: *Stretchable photo sensor based on graphene/perylene composite utilizing electrohydrodynamic fabrication technique*. Proc. SPIE. 9655, Fifth Asia-Pacific Optical Sensors Conference, 96550F. (July 01, 2015), jeju, South Korea; 07/2015

3. **Shawkat Ali,** Jinho Bae, Chong Hyun Lee: *Single layered flexible photo-detector based on perylene/graphene composite through printed technology*. Proc. SPIE 9655, Fifth Asia-Pacific Optical Sensors Conference, 96550E (July 1, 2015), JEJU; 05/2015

4. **Shawkat Ali**, Jinho Bae, Kyung Hyun Choi, Chong Hyun Lee: *Organic memory cell based on a memristor*. Invitation workshop on memristor, 2014 JEJU National University. Republic of Korea

5. Arshad Hassan, **Shawkat Ali**, Jinho Bae, Chong Hyun Lee: Flexible dual-band antenna for communication and radar applications. 2016 IEEE Radar conference, USA

Annex-D Patents

1. ELEMENT BASED MEMRESITOR (멤리스터 기반), Registration No. : 1015576210000
2. MEMORY CELL USING MEMRESISTOR (멤리스터를 이용한 메모리), Registration No. : 1015775320000
3. APPARATUS FOR DRIVING MEMRESISTOR (멤리스터 구동 장치), Registration No. 1015969360000
4. Asymmetric memristor for sneak current reduction (under process)
5. State memorable LED (under process)
6. Sneak current elimination by two memristor in passive crossbar arrays (under process)
7. Disposable electronic biosensor for food born pathogen (under process)